UNIVERSITY OF OKLAHOMA

GRADUATE COLLEGE

REDOX INTERFACES IN THE PROXIMAL PERMIAN CUTLER FORMATION, MESA COUNTY, WESTERN COLORADO

A THESIS

SUBMITTED TO THE GRADUATE FACULTY

in partial fulfillment of the requirements for the

Degree of

MASTER OF SCIENCE

By

DESIREE PAIGE HULLASTER
Norman, Oklahoma 2019

REDOX INTERFACES IN THE PROXIMAL PERMIAN CUTLER FORMATION, MESA COUNTY, WESTERN COLORADO

A THESIS APPROVED FOR THE
CONOCOPHILLIPS SCHOOL OF GEOLOGY AND GEOPHYSICS

BY

Dr. Andrew S. Elwood Madden, Chair

Dr. Gerilyn S. Soreghan

Dr. Kato T. Dee

Dedications

For my daughter, Madelynn Rose, and my best friend Alicia Norman.

Maddie you give my life purpose. You helped me persevere thought out this process and I could not have accomplished this goal without you, I love you with all my heart. This is for you.

Alicia, though you are no longer with us, I keep your memory with me in everything I do. You were the most supportive, loving, hilarious best friend anyone could ask for and you believed in me when no one else did. You always said I would do great things which has always driven me forward when times get tough. I'm forever grateful for your extraordinarily positive influence on my life.

ACKNOWLEDGEMENTS

D.P.H. was supported by NSF EPSCoR RII Track-2 award #1736255. We thank Dr. Lindsey Hunt for help with the electron microprobe; Matt Hamilton for his assistance with SEM; Dr. Mehrdad Sardar Abadi for his help with LPSA; Dr. Claire Curry for her help with ArcGIS; Gary Davison, Charles Duval, and Cansu Demirel for their assistance with XRD; Lily Pfeifer-Johnson and Michael Miller for field support; and Emma Bachman for analyzing samples on the Raman.

Table of Contents

Abstract

Diagenetic and hydrothermal fluid alteration of ancient sedimentary rocks create visible ferrous (green)/ferric (red) redox interfaces attributable to changes in iron oxide and phyllosilicate mineralogy. Redox interfaces control aqueous/ solid phase partitioning of metals such as uranium. However, the long-term implications of ancient redox interfaces for the immobilization of metals in reduced, green siliciclastic rocks interfingered and layered between Permian red beds remains uncertain. We investigated redox interfaces of early Permian sediments in contact with Precambrian basement rock to understand how red bed mineralogy impacts metal reactivity during hydrothermal events. The proximal Cutler Formation onlaps Precambrian crystalline basement at the mouth of Unaweep Canyon in western Colorado and hosts dark green coarse-grained Cutler rocks in direct contact with basement rock and mint green, reduced, primarily coarse-grained intervals within red bed siliciclastic strata above the basement contact. The more western portion of the proximal Cutler additionally hosts bleached-mint green layers within red beds. We hypothesized that color variations resulted from grain-size variations that regulated flow of reducing fluids during the Tertiary hydrothermal event in the nearby La Sal mountains. Powder x-ray diffraction (XRD), scanning electron microscopy (SEM), and energy-dispersive x-ray spectroscopy (EDS) revealed the presence of hematite and chlorite in both red and green sediments, but no iron oxide occurs in the bleached sediments. Pervasive hematite in both red and green layers suggests that sediments were hematite-rich before hydrothermal alteration. Abundant mixed layer and swelling clays such as smectite, illite-smectite, and chlorite-smectite (or corrensite) dominate the mineralogy of the clay fraction. Previous studies indicated the presence of kaolinite; however, it is absent in our samples. Optical microscopy and electron microbeam analyses were performed to identify biotite-fluid reactivity,

especially in association with chloritization, but also with authigenic mineral formations in association with hydrothermal fluid alteration. Furthermore, quantitative comparison of grain sizes in red, green, and bleached (RGB) intervals were performed via laser particle size analysis (LPSA) and demonstrates that the red intervals are finer grained than the green and bleached intervals. Ultimately, understanding the reactivity of redox interfaces in ancient sedimentary rocks will help predict the behavior of redox-active metals such as U(VI) and the long-term persistence of sedimentary rock reducing capacity for metal immobilization.

1. INTRODUCTION

Red beds are associated with oxidizing conditions, as their color reflects the pervasive presence of the ferric oxide hematite (Bankole et al., 2016). Red bed genesis has been a hot topic of debate for years (Van Houten, 1973; Walker, 1974). Some suggested that continental red beds may form during chemical weathering (e.g., Van Houten, 1973; Dubiel and Smoot, 1994), although with uncertain paleoclimatic significance (e.g., Sheldon, 2005). However, two hypotheses are generally favored: 1) alteration of Fe-bearing silicate grains during diagenesis, and 2) recrystallization of poorly crystalline or low-temperature forms of ferric oxides such as goethite into hematite during burial diagenesis (Turner, 1977; Hubert and Reed, 1978; Elmore and Van der Voo, 1982).

Red beds are commonly altered to host green-bleached and green to red intercalations reflecting post-depositional hydrothermal alteration (Bankole et al., 2016). The origin of different sediment/ rock colors typically reflects mineralogy but more specifically, the valence state of iron within the minerals (Keller, 1953; Van Houten, 1973; McBride, 1974). Iron (II) or, ferrous iron, contributes to green or grey hues whereas iron (III), ferric iron, contributes to red, brown, and yellow colors in the form of ferric oxides (Keller, 1953; McBride 1974). Examples of minerals that can appear green as a result of reduced iron include chlorite, glauconite, smectite (montmorillonite), illite, epidote, hematite, and biotite (Keller, 1953). Ferric iron often accompanies ferrous iron in green silicate minerals thus the ratios of iron valence (as FeO/Fe_2O_3) can be useful for predicting color (MacCarthy, 1926; Keller, 1953). Ferric iron-bearing minerals include the iron-oxides such as hematite, goethite, lepidocrocite, and maghemite (Keller, 1953). Additionally, the ferro-ferric iron-oxide magnetite, Fe_3O_4, exhibits grey and black colors, and iron-sulfides (i.e. pyrite) exhibit black to dark green hues (Keller, 1953). The colors of these

minerals and their respective iron valence states thus record redox conditions in altered red beds. Titanium could also play a role in mint green rock color within these altered Permian red beds (Morad and Aldahan, 1986). Ti-oxides (i.e. rutile) can be associated with green sediments because they form authigenically via the dissolution of detrital ilmenite which liberates the necessary titanium ions required to form authigenic Ti-oxides in reducing environments (Morad and Aldahan, 1986).

Visible redox conditions are interpreted as an effect of grain-size differences wherein coarse-grained layers served as preferential fluid pathways between finer grained clay-rich layers. The fine-grained layers retard fluid flow and maintain the reducing conditions that lead to iron reduction, Fe (II), and pyrite (Steiner and Lucas, 2000). Important components of the fluid chemistry are pH, composition and temperature, in addition to the fluid-rock ratio (Meunier, 2005). Multiple episodes of oxidizing and reducing fluid alteration may overprint depositional signals; thus, discrimination of fluid compositions based on their mineralogical effects in the fluid-rock system provides opportunities to interpret deep time signatures of local and regional geosphere-hydrosphere dynamics.

Redox interfaces in clastic sedimentary units are also of interest because reducing conditions sequester metals such as uranium. Redox interfaces in sandstones host ~25% of the world's uranium resources (Kyser, 2014), as uranium is generally soluble in oxidizing conditions and insoluble in reducing conditions. Oxidizing fluids leach U(VI) from detrital U-bearing minerals, where it may be immobilized in contact with reduced sediments or fluids containing reductants such as organic matter, hydrocarbons, sulfide or sulfate minerals, or Fe(II)-bearing minerals (Kyser, 2014). Oxidizing fluids sequester uranium with two simultaneous or successive processes: adsorption and direct precipitation of uranyl phosphate/vanadate minerals from over-

saturated solutions (Langmuir, 1978). However, reducing fluids primarily sequester uranium by precipitation of U(IV)- oxide, uraninite or U(VI)- silicate, coffinite (Finch and Murakami, 1999). Therefore, it is important to understand hydrothermal, diagenetic, and mineralogic alterations of sediments associated with metal removal from the system. Understanding processes that lead to uranium deposition is additionally critical for both mineral resource assessment and environmental risk. Generating redox interfaces in uranium-contaminated groundwater continues to receive considerable attention as a strategy for remediation (Bargar et al., 2013; Nöel et al., 2017).

1.1 Redox interfaces in the Permian Cutler Formation

This study was motivated by field observations of the proximal, lower Permian Cutler Formation, which hosts redox interfaces in the form of bleached to green interfingering in red beds as well as dark green layers in contact with or stratigraphically above crystalline basement rock (Fig. 1). Previous work has focused on characterizing the mineralogy of the Cutler Formation for paleoclimate studies and provenance but disregard the meaning and implications of visible redox interfaces within the Permian red beds (Fig. 2) (Werner, 1974; Suttner and Dutta, 1986). Paleomagnetic data suggest that redox conditions within the distal (>10 km away from source) Cutler Formation reflect hydrothermal alteration along faults in the Lisbon Valley during the late Cretaceous to early Tertiary (Reynolds et al., 1985); however, redox interfaces in the proximal Cutler Formation (within ~10 km of the source) were not similarly investigated. Furthermore, the depositional history of the proximal formation is heavily debated to be either a non-glacially related fluvial system or a proglacial fluvial system (e.g., Campbell, 1981; Soreghan et al., 2009). The depositional environment plays a critical role in creating the

necessary permeable and impermeable layers for reducing fluid pathways that result in the reduced green-bleached sediment within the formation.

A firm understanding of the development of redox interfaces and their impact on potential uranium immobilization in the Cutler Formation demands a complete grasp of the composition and depositional history of the system (Bankole et al., 2016). We hypothesize that if (1) the green rocks contain reduced iron, Fe (II), then there is potential for the reduction of metals such as U, and the proximal Cutler might then host paleovalley-type uranium accumulations (e.g., Hou et al., 2017), (2) the green-bleached rocks host preferential fluid pathways during a hydrothermal event that dissolved iron or reduced Fe(III) to Fe(II), then the red-green-bleached (RGB) colorations will have unique grain-size differences, (3) the green-bleached coloration is from post-depositional reducing hydrothermal fluid alteration then secondary mineral intergrowths and authigenic mineral/clay formations should be present within the rocks, (4) the mineralogical and geochemical changes in the redox interfaces can be quantified via SEM and XRD, then the geologic history of fluid-rock interactions can be unraveled and the maximum fluid and diagenetic temperatures can be constrained, (5) Unaweep Canyon has been over-deepened by paleoglacial carving, the proximal Cutler may contain mineralogical or geochemical signatures of proglacial weathering and subsequent groundwater flow influenced by this paleogeomorphic feature. This study particularly addresses key knowledge gaps in understanding the mineralogical, geochemical, and textural differences between RGB layers within the proximal Cutler Formation, with the goal of constraining the sequence of processes and events leading to redox interface development and informing future studies that will further explore implications for uranium accumulation.

2. GEOLOGIC SETTING AND FIELD SAMPLING

The lower Permian Cutler Formation onlaps Precambrian basement at the mouth of Unaweep Canyon, located southwest of Grand Junction in Mesa County, Colorado (Fig. 3). The canyon bisects the Uncompahgre Plateau, a late Cenozoic uplift that was also previously uplifted during the Pennsylvanian (as the Uncompahgre uplift) as a result of orogenic activity that built the Ancestral Rocky Mountains (Baars and Stevenson, 1981; Kluth and Coney, 1981; Soreghan et al., 2007; Soreghan et al., 2009). During the Pennsylvanian, the Uncompahgre uplift was eroded to the crystalline Precambrian basement, comprising gneiss, granite, and varied metamorphic rocks that represent multiple magmatic episodes, dated as 1.4 - 1.6 Ga (Hedge et al., 1968; Mose and Bickford, 1969; Case, 1991). Tectonic activity resumed during the Laramide orogeny ~80-40 Ma and subsequently, the epeirogenic uplift associated with the incision of the Colorado Plateau ~5-6 Ma (Dorsey and Lazear, 2013). The canyon was then thought to have been fluvially exhumed and abandoned between 1.4-0.8 Ma (Balco et al., 2013; Aslan et al., 2014; Soreghan et al., 2015). The formation of Unaweep Canyon has been the subject of much debate upon which there are three prevailing hypotheses: 1) Fluvial incision during the late Cenozoic (Miocene-recent); 2) Glacial incision during the late Cenozoic (Quaternary); or 3) Glacial incision in the late Carboniferous- Early Permian (Late Paleozoic) followed by Permian-Mesozoic sedimentation, then partial fluvial exhumation of the buried paleovalley from 6 to 1.5 Ma by the ancestral Gunnison River, subsequent partial filling by Pleistocene sediment after abandonment by the ancestral Gunnison River, and finally, gradual headward erosion by East and West Creeks to form the current configuration of a canyon with two mouths (Marra, 2008; Soreghan et al., 2009; Aslan et al., 2014; Soreghan et al., 2015).

Unaweep Canyon hosts two underfit drainages (East and West Creek) that drain in opposite directions emanating from Unaweep Divide at an elevation of 7047 ft (2148 m), making Unaweep Canyon the only canyon in the world that has two mouths (Aslan et al., 2014; Soreghan et al., 2015). The initiation of two opposite-flowing drainage systems is inferred to have begun with damming via mass wasting of the ancestral Gunnison river 1.41 ± 0.19 Ma, blocking flow to the west mouth of the canyon (Balco et al., 2013; Aslan et al., 2014). In turn, a lake formed which is supported by the Massey #1 and #2 cores (Soreghan et al., 2007; Marra, 2008; Balco et al., 2013; Soreghan et al., 2015). By 1.34 ± 0.13 Ma, the lake filled via sedimentation and the river escaped eastward towards Grand Junction (Soreghan et al., 2007; Balco et al., 2013; Aslan et al., 2014).

2.1 The Proximal Lower Permian Cutler Formation

The Cutler Formation is a generally maroon to red, arkosic siliciclastic unit (siltstone, sandstone, and conglomerate). Strata exposed near Gateway, Colorado, at the mouth of Unaweep Canyon, are referred to as the proximal Cutler (Fig. 3) (Cater and Craig, 1970; Soreghan et al., 2009). Suttner and Dutta (1986) after Cater (1955) suggested the maximum burial of the Cutler Formation is ~2400 m, implying burial temperatures of ~100-200º C, generally less than expected depths and temperatures of the complete smectite-to-illite transition (Cater, 1955; Suttner and Dutta, 1986; Worden and Burley, 2003; Meunier, 2005). With distance from the onlap contact, grain sizes of the Cutler Formation decrease from boulder-cobble-pebble-gravel conglomerate and diamictite to fine-grained sand/siltstone (Campbell, 1981).

In many places along strike, the lower Cutler Formation depositionally onlaps Precambrian igneous and metamorphic rocks (basement rocks); however, in other areas such as the Paradox Basin the lower contact is with the subjacent Pennsylvanian Hermosa Formation

(Fig. 4) (Cater and Craig, 1970). The Cutler Group lies unconformably below the Triassic-Jurassic Moenkopi Formation (Fig. 4) (Cater and Craig, 1970). Depositional interpretations for the proximal Cutler Formation converge on fluvial-alluvial, but range among hot-humid, hot-arid, or – more recently—cold-humid (proglacial) systems sourced from erosion of the Uncompahgre uplift that resulted from the Ancestral Rocky Mountains orogeny (Mack, 1977; Campbell, 1981; Kluth and Coney, 1981; Suttner and Dutta, 1986; Soreghan et al., 2007; Soreghan et al., 2009; Soreghan et al., 2015).

The color of the formation varies substantially, with mint green and bleached coarse-grained strata intercalated with the proximal red beds but distally predominated by uniformly colored red beds (Fig. 2) (Soreghan et al., 2007; Soreghan et al., 2009). Such variegated coloration is typically attributed to the presence of hematite/iron-oxide (red), chlorite (green), epidote (green), and stripping of these minerals (bleached) (Meunier, 2005). Also, in the proximal Cutler are dark green conglomeratic intervals in contact with underlying basement rocks.

Regional fault systems and basement-sediment contacts potentially served as a hydrothermal fluid conduit from the Tertiary La Sal laccolith (Shawe, 2011). Understanding these hydrothermal fluid impacts is critical for linking the mineralogy of Permian red beds to redox interfaces and their effect on metal reduction/ partitioning. Cutler Formation samples were collected from outcrops in proximal to “distal”- proximal and labelled respectively as sections III-XII, as designated in Soreghan et al. (2009) (Fig. 3 and 5). Samples were also collected north-westward along the basement contact for an inclusive interpretation of the RGB redox interfaces (Fig. 3).

2.2 Mineralogy and Petrology of the Cutler Formation

Although a few studies investigated the mineralogy of the Cutler Formation, there is no previous work to date on mineralogical changes associated with the prolific color variations throughout the proximal area. There are notable mineralogic changes that occur from the proximal Cutler to the distal as the sediment travels further from its 1.48 Ga vernal-mesa quartz monzonite source rock and becomes intercalated with eolian sourced Appalachian Mountain strata in the salt wash Paradox Basin (Hedge et al., 1968; Werner, 1974). Previous thin-section and outcrop analysis by Campbell (1981) shows quartz and calcite cement increases distally while igneous and metamorphic rock fragments decrease. Petrographic work by Werner (1974) reports the presence of, "…quartz, rock fragments, potassium and plagioclase feldspar, biotite, iron-stained clay-rich matrix, and authigenic calcite… (as well as) common heavy-minerals of apatite, chlorite, epidote, garnet, muscovite, opaques, sphene, tourmaline, and zircon" in the proximal Cutler near Gateway, Colorado, all of which are evident in our samples (Werner, 1974). Suttner and Dutta (1986) characterized the proximal Cutler Formation as a chemically immature, silica-depleted, arkosic sandstone based on its framework mineralogy that yields a QFR value of 49:44:7 (Suttner and Dutta, 1986). Additional work performed on the clay mineralogy of the Cutler Formation via XRD and SEM by Dutta and Suttner (1986) reports sandstone clay compositions of, "…kaolinite, chlorite, smectite, illite, quartz, various carbonate minerals, and iron oxide" without any further mention of qualitative or quantitative analyses on the mixed-layer clays (Dutta and Suttner, 1986). Pervasive chlorite and smectite-rich cements were noted throughout the formation (Dutta and Suttner, 1986). However, Suttner and Dutta (1986) failed to compare the visible color variations trending from proximal to distal along the Cutler outcrops. The green/drab colors suggest the potential for uranium immobilization by reaction with Fe (II)-bearing minerals (for example, chlorite (Brookshaw et al., 2015) or smectite

(Qafoku et al., 2017)) and furthers the need to explore these variations. The overarching hypothesis by Suttner and Dutta (1986) is the chlorite is of authigenic origin based on crystalline habit; however, the work presented here attempts to readdress the origin of the clays (e.g. authigenic or detrital) related to color variations in the proximal Cutler Formation.

2.3 Relation of regional uranium mineral deposit occurrences to fluid flow events

The Unaweep Canyon area has produced significant uranium deposits primarily identified in Mesozoic formations. Multiple uranium deposit sites, including Gateway, form the Uravan district (Bankey, 2003). The uranium and vanadium production from 1947 to 1982 was upwards of 85 million lbs (39 million kg) and 427 million lbs (194 million kg), respectively (Chenoweth, 1996; Bankey, 2003). The Mesozoic uranium deposits in this area occur in lithologically controlled bodies within sandstone layers bounded above and below by mudstone, particularly associated with permeable channel sands containing organic-rich materials or redox interfaces associated with sandstone/mudstone contacts. Higher ore grades occur closer to redox interfaces between oxidized (red bed), reduced, and bleached/carbonaceous facies (Shawe, 1976).

Discriminating the timing and extent of regional fluid alteration events remain an active area of research, with historical ideas summarized by Dahlkamp (2010) and Shawe (2011). The source(s) of uranium, mineralizing fluids, and post-mineralization fluid alteration history vary by location within the Colorado Plateau. Potential sources of fluid alteration that might have influenced the proximal Cutler Formation include meteoric syn-depositional and diagenetic groundwaters, Paradox basin fluids expelled during Permo-Triassic salt tectonic valley collapse (Thompson et al., 2018), large-scale regional groundwater flow (Sanford, 1982 and subsequent contributions), hydrocarbon evolution, mudstone dewatering in overlying Mesozoic mudstone

during burial and compaction, fluids mobilized during the Laramide orogeny, fluids associated with multiple regional Tertiary volcanic episodes to the east, southeast, south, and southwest, and meteoric groundwater.

In particular, the La Sal Mountain laccolith, located in Utah 30-40 km from the proximal Cutler Formation, is the most likely source of produced fluids that hydrothermally altered the Paradox Formation during the early Tertiary (Shawe, 2011; Thomson et al., 2015). Thompson et al. (2015) further constrained this fluid event to the Oligocene, from 33-23 Ma, and Chan, Parry, and Bowman (2000) determined the La Sal mountain activity to have occurred from 28-25 Ma, thus over a span of 4 Ma. These fluids heated formation waters in the Paradox Basin that subsequently followed permeable flow paths along fault zones which carried them from Utah into the western Colorado area and within the Uravan mineral belt (Shawe, 2011). The reduced fluids, in tandem with the water expelled from magmas, are what triggered the leaching of certain elements from in-situ sedimentary rocks and subsequent deposition upon mixing with other more oxidizing fluids at the chemical/redox interfaces (Shawe, 2011). Reducing hydrothermal fluids originating from the Tertiary La Sal mountains followed fault zones and the more permeable Cutler Formation strata creating the visible redox interfaces still present in the formation today, also influencing redox interfaces in the overlying uranium-bearing Mesozoic sandstones (Shawe, 2011).

2.3.1 The Permian Cutler Formation – a possible uranium paleovalley deposit host?

Uranium deposits are only found in the distal Cutler strata (>10 km W-SW from Unaweep Canyon). However, some of the necessary characteristics to form uranium paleovalley deposits as described by Hou et al. (2017) are satisfied by proximal Cutler strata as follows: (1) fluvial depositional environments, (2) coarse-grained green-bleached relatively unconsolidated,

reducing strata confined by fine-grained red rocks, and (3) the presence of paleovalley-incised Precambrian igneous and metamorphic bedrock. In this study, the redox interfaces of the proximal Cutler Formation were studied at length partly to determine the suitability of the proximal Cutler Formation to host a uranium paleovalley deposit.

3. MATERIALS AND METHODS

Samples analyzed in this study were acquired from outcrops located in the vicinity of Gateway, far western Colorado, southwest of Grand Junction or from the Massey-1 core drilled in Unaweep Canyon as described in Marra (2008). Cutler Formation rock samples were collected from sections III to XII as described in Soreghan et al (2009), targeting the red-green-bleached interfaces and the relatively unaltered Cutler red beds (Fig. 3). Samples were also collected westward of section XII for lateral representation of the redox interfaces.

3.1 X-Ray Diffraction

A total of 45 RGB samples were analyzed for their bulk mineralogy. Of those samples, 39 were additionally analyzed for clay mineralogy.

3.1.1 Random Bulk Mount Preparation

Bulk random mounts to quantify whole-rock mineralogy were prepared generally following Eberl (2003). Sample preparation was started by crushing/grinding the desired sample with a hammer or percussion mortar until 1-2 g pass through a 0.4 mm sieve. The sample was then transferred to a micronizing tube, pre-loaded with grinding elements (Y-Zr-oxide) and 5-7 mL of methanol were added. The sample was micronized for 5 minutes and the resultant liquid poured into a weigh boat and dried in a drying oven. Once dry, the sample was stirred with a stir-rod to prevent preferred orientation due to gravimetric settling and filtered through the

micronizing sieve once more. Finally, the sample was poured into a glass cavity mount flush with the rim while avoiding compaction into the cavity to minimize preferred orientation. The sample was then analyzed as described in section 3.1.5.

3.1.2 Separation of clay fraction from bulk samples

For most rocks and sediments, whole-rock bulk mineralogy by powder XRD provides relatively little insight into the mineralogy of the clay size fraction. The procedure to separate the clay size fraction follows the methods of Moore and Reynolds (1997). Rock samples were crushed, and 1-2 g were filtered through a 0.4 mm sieve (Eberl, 2003). The material was then transferred to a glass beaker, and 150 mL distilled water and a "pinch" of sodium (hexa)metaphosphate were added. The solution was placed in the sonic dismembrator for 5 minutes to disaggregate the rock fragments, and then centrifuged at 800 rpm for 3.5 minutes. The liquid was decanted after centrifuging, avoiding the pelleted material at the bottom. This liquid contained the clay-sized (2 μm) fraction used to make the oriented mount.

3.1.3 Random Clay Mount Preparation

Random clay mounts are used primarily to elucidate the di- vs. tri-octahedral character of phyllosilicate minerals using (hk0) reflections that indicate *b*-axis dimensions or discriminate between polymorphs; neither of which can be determined in an oriented clay mount. In this case, the liquid containing the 2 μm fraction is dried in the drying oven, stirred to a powder and mounted into a bulk random mount glass holder as described in section 3.1.1. For more detail, see Moore and Reynolds (1997).

3.1.4 Oriented Clay Mount Preparation

Oriented mounts use the natural preferred orientation of phyllosilicate minerals and are used to interpret the otherwise largely unknown clay fraction mineralogy of each sample. Oriented clay films were prepared on fused silica slides according to the filter peel method of Drever (1973) as described in Moore and Reynolds (1997). The clay solution created in section 3.1.2 was vacuum filtered onto 0.2 µm filter and calcium-saturated with 1M $CaCl_2$. The top of the filter paper that stuck to the slide was gently rolled to remove any potential air bubbles and then placed in a drying oven at ~50°C. The filter paper was peeled off and the remaining oriented clay on the glass slide was the AD (air-dried) specimen used for analysis.

3.1.5 Powder-XRD Data Collection and Interpretation

All random and oriented mounts were analyzed using a Rigaku Ultima IV powder X-ray diffractometer using Cu-Kα radiation with a voltage of 40 kV, current of 44 mA, Bragg-Brentano optical configuration, and curved-graphite diffracted-beam monochromator. Data were analyzed using Jade 2010 with the ICDD-PDF4+ database. Whole-pattern Rietveld fitting was used for quantitative weight percent determinations. Oriented clay mounts were scanned with a 2Θ range from 2-32 for a count time of 2s and a step size of 0.02. Interpretation of oriented clay mount data requires a minimum of three separate scans. The first run following mount preparation is known as the air-dried (AD) sample. The sample was then 'glycolated' via exposure to ethylene glycol (EG) vapor in a desiccator overnight (~24 hours, but no longer than 72 hours due to the possibility of total dissociation of swelling clays if present) and analyzed on the XRD immediately upon removal from the desiccator. Then, the specimen was heat-treated at 550°C (HT550) for one hour in the drying oven and scanned one last time on the XRD. Once all the data were collected, the three patterns were superimposed in Jade 2010 (Materials Data, Inc.).

The peak position values and relative shifting, swelling, transformation, etc. of the three different patterns aid in identification of the clays.

3.2 Petrography

Petrography is used primarily to understand mineral associations and alteration in the Cutler Formation. Splits of the same Cutler rock samples used for XRD were sent to either the University of Iowa or Wagner Petrographic for preparation of standard microprobe-polished thin sections. Thin section samples were specifically selected to capture the red/green and red/bleached redox interfaces. A ZEISS Axio Imager.Z1 stereo microscope was used to analyze all twenty-two thin sections via plane polarized light and cross-polarized light to determine grain-size variations, sorting, roundness, overall mineralogy, and mineral associations.

The thin sections were carbon-coated and examined via scanning electron microscopy (SEM) to identify minerals and understand mineral textures, associations, and morphology. SEM was performed on a FEI Quanta 250 with a Bruker energy-dispersive spectrometer (EDS) at the University of Oklahoma. Imaging was performed in backscatter mode for all samples.

Select carbon-coated thin sections were subsequently analyzed on the electron microprobe for a qualitative interpretation of iron-oxides, micas, and chlorites. Energy-dispersive X-ray analysis (EDS) elemental mapping was performed at the University of Oklahoma on a CAMECA SX100 electron probe micro-analyzer. Analysis and mapping employed a 15 kV accelerating voltage and a 20 nA beam current (measured at the Faraday cup). Elemental mapping conditions were set to 100 frames at 200 seconds per frame, for a total acquisition time of 20,000 seconds.

3.3 Laser Particle Size Analysis (LPSA)

LPSA was performed to determine the grain-size distributions between the RGB rocks for understanding preferential hydrothermal fluid pathways. Five rock samples containing both red/green or red/bleached were carefully selected from proximal to distal Cutler to represent grain-size distributions. Rock samples were disaggregated using finger pressure, then dry sieved through a 2 mm mesh before transfer to 50 mL Falcon tubes. Removing grains >2 mm facilitates LPSA analyses; however, material retained on the sieve was not quantified. Iron-oxide cement was removed via one round of the standard CBD treatment method. Three drops of 1M sodium (hexa)metaphosphate were added to each sample to prevent clumping. The uncemented samples were sonicated for 5 minutes each before analysis on a Mastersizer 3000 Hydro EV.

3.4 Whole-rock Geochemistry

Detailed whole-rock geochemistry was performed on eleven representative rock samples by ALS Mineralogy in Reno, Nevada for major, trace, and rare earth elements (REEs). Methods include fused bead, acid digestion, and ICP-MS. In addition, ferrous iron was measured via titration.

4. RESULTS

4.1 Powder- XRD Mineralogy

The Cutler Formation samples are labeled according to Soreghan et al. (2009) from proximal to distal as sections III – XII, see Fig. 3. The bulk and clay mineralogy of RGB rock samples were analyzed to discriminate mineralogical variations that contribute to color changes resulting from redox conditions. Rock colors are described according to the Munsell color chart

(Table 1). Whenever possible, subsamples of intercalated red and green or red and bleached were collected from the same sample.

4.1.1 Bulk Mineralogy

The overall bulk mineralogy of 45 RGB rocks collected from the Cutler Formation around Gateway, Colorado are quite similar. The red, green, and bleached rocks contain varying amounts of chlorite, smectite, illite/mica, plagioclase, potassium feldspar, calcite, and quartz plus minor gypsum and epidote (Table 2). The proximal Cutler Formation has abundant mica which, as referred to in this paper, is biotite. Identification of the heavy minerals is primarily from thin-section analysis due to their relatively low abundance (<1%) in most samples and therefore inability to be represented in XRD. Epidote is the most abundant heavy-mineral, detected via XRD in two igneous rocks, one red rock, and three green at 0.3-7.6 wt.% (Table 2). The two igneous rocks with detectable epidote (1218-26D and 1218-28VMQM) have lower modeled epidote percentages, 1.3% and 0.3% respectively, than the epidote-bearing red and green Cutler samples.

Counterintuitively, the red and green rocks both host ferric iron oxide (hematite) that was verified using Raman spectroscopy (Fig. 6). This alludes to the rock coloration being dependent on specific valence states as opposed to the overall mineralogy or elemental chemistry; specifically, ferric iron, Fe(III), attributed to the red coloration and ferrous iron, Fe(II), likely attributed to the green coloration (Cornell and Schwertmann, 2003). X-ray diffraction subtraction patterns of associated red-green and red-bleached samples revealed high similarities in the red vs green and red vs bleached rocks with similarity percentages ranging from 81-97.1% (Fig. 7-8). XRD pattern overlays provide visual evidence of higher iron-oxide as hematite, in decreasing

abundance, as red > green >> bleached. Also, chlorite which is typically green and commonly associated with Fe(II) is present in both red and green layers.

Two Precambrian igneous rocks were collected in the area around the proximal Cutler Formation and their XRD derived mineralogy was plotted on a Streckeisen QAP diagram to classify each rock (Streckeisen, 1974). The QAP of samples 1218-26D and 1218-28VMQM are 37:60:3 and 34:34:32, respectively. Sample 1218-26D is identified as an alkali-feldspar granite and is one of the siliciclastic Cutler source rocks in the study area as determined by the mineralogy and direct contact of this basement rock with the Cutler Formation. The bulk mineralogy of this sample contains 4.6% chlorite, 10.2% illite/mica, 1.3% hematite, and 1.3% epidote. Sample 1218-28VMQM is a potential source rock identified as a monzo-granite that does not host chlorite or hematite but contains 5.9% illite/mica and 0.3% epidote. Full wt.% values are reported in Table 2.

4.1.2 RGB k-means cluster analysis

Interpretations were enhanced using k-means cluster analysis with 10 groups showing spatial relationships (Fig. 9 and 10). Trace minerals were removed from the sample sets and the samples were normalized to 100%. Fe-oxide, interpreted to be hematite, is present in all but 6 green/bleached samples from 0.1 to 7.7%. The highest values of hematite, up to 7.7%, are in the red rocks and the dark green rocks, sections V – VIII, in contact with/or a short distance above basement. Chlorite is most abundant in cluster group 10, >20% in each sample, with a relative decrease in illite/mica. All samples in cluster group 10 are in sections V-VII, have coarse grain-sizes, and are described as some variation of green. The lack of illite/mica in tandem with increased chlorite could indicate that illite/mica was weathered or altered to chlorite (Meunier, 2005). Calcite is present from 0 – 10% throughout the samples and only exceeds 20% in 5

samples, cluster group 1, which are primarily distal red samples. A general trend of high illite/mica: chlorite ratios occurs in cluster groups 2, 8, and 9, with no general spatial commonalities between the three clusters. Group 2 represents distal red bed samples from section XII; groups 8 and 9 are proximal samples that trend east to west from the mouth of Unaweep Canyon to the Colorado-Utah boarder. The opposite trend occurs in group 10, an all green cluster, which is high in chlorite and low in illite/mica. Another unique trend in group 3 shows high smectite: illite/mica ratios. Detrital epidote is present in small but detectable amounts throughout the samples; its distribution is described further in section 4.2.

4.1.3 Statistical comparison of RGB bulk mineralogy

Box plots were made to see general trends in individual minerals between the red, green, bleached, and basement rocks (Fig. 11). Hematite exhibits an average of 3.5% in the red rocks, 2.0% in the green rocks, and 0.6% in the basement rock with zero in the bleached. There is more illite/mica on average in the red rocks (30.2%) than in the green (21.7%), bleached (27.9%), or basement- which contains the lowest average at 8.0%. Calcite again is most prevalent in the distal red rocks but remains minor throughout the formation. The plagioclase content is similar among all rock colors and averages 16.5, 14.7, and 12.0 % in the bleached, green, and red layers, respectively. Potassium feldspar is also similar across all rock colors. The quartz content averages lowest in the green rocks and highest in the red rocks. Epidote primarily occurs in the green strata and basement rocks. Smectite is a clay mineral and thus is commonly undetected by bulk XRD analyses; however, a sufficiently high abundance occurred in some samples which showed up in the bulk mineralogy. In those samples, smectite exhibits the highest abundance in the green rocks with 7.5% followed by 3% in the bleached and 2% in the red, with none in the basement rocks.

4.1.4 Clay Mineralogy

The clay mineralogy of the Cutler Formation consists of abundant mixed-layer illite-smectite, illite, smectite, corrensite (ordered chlorite-smectite), and chlorite plus chlorite-smectite in one sample (53S V-1 Green) without any evidence of kaolinite (Table 3). Previous studies of the proximal Cutler also found abundant chlorite, smectite, and illite, but have suggested the presence of small contributions of kaolinite throughout the formation and lacked discussion on mixed-layer clays (Werner, 1974; Dutta and Suttner, 1986). Biscaye factors were applied to all spectra of clay fraction, oriented mounts to convert peak areas to semiquantitative estimates of weight percent (Biscaye, 1965).

Corrensite, an ordered mixed-layer chlorite-smectite, is present in samples 53 III-14C green, 53 IV-244.5 red, 1218-15 red, 1218-10 red and bleach, 63 XII-16.5 red, and 63 XII-37.5 red with no corrensite in the basement contact samples from section VI – VIII (Table 3). A green clay sample, MC-01-1078, collected from a fracture at 1078 ft in the gneissic Massey Core #1 is pure corrensite (Fig. 12 and 13). All samples in sections VII – X plus the western proximal samples contain some amount of smectite. The distal-most section XII samples instead host corrensite and mixed-layer illite-smectite. Smectite distribution in the proximal-most samples at the mouth of Unaweep Canyon is not consistent throughout the samples. Smectite in the air-dried Cutler samples is primarily present in a minimally-hydrated state giving AD peaks around 12.5Å that swell to 16.9Å upon exposure to ethylene glycol. The clay fraction of green and red sections VI – X all have chlorite, smectite, and illite with no mixed-layer clays. Illite-smectite mixed layers are only in proximal sections III and IV, and in the distal most section XII but non-unique to the red or the green rocks. No bleached layers have illite-smectite, but all have abundant smectite.

Random clay fraction mounts were used to discriminate di-octahedral versus tri-octahedral sheets based on the (060) d-spacings in the EG clay spectra. Sample 63S VI-27 Green has three peaks in the d(060) region; a tri-octahedral chlorite peak at 1.55 Å, a peak at 1.51 Å that may indicate a tri-di- mixed-layer biotite-smectite that is being skewed slightly by a 1.47 Å peak, and a 1.54 Å quartz peak identified based on a subsequent 1.82 Å peak also associated with quartz (Fig. 14) (Brindley and Brown, 1980). Sample 53 IV-244.5 Red also contains the quartz peaks in the (060) region at 1.82 Å and 1.54 Å plus an iron-rich, tri-octahedral chlorite peak at 1.56 Å, an iron-rich illite peak at 1.51 Å, and a di-octahedral smectite peak at 1.49 Å (Brindley and Brown, 1980). The green clay basement sample, MC-01-1078, is pure corrensite and contains two peaks in the d(060) region; one at 1.538Å which indicates a tri-octahedral clay and one at 1.507Å which indicates a di-octahedral clay thus the corrensite is interpreted to be tri-di-octahedral corrensite.

4.2 Petrography of Mineral Alteration

4.2.1 Optical Microscopy

Thin-sections were made from the same rocks used for XRD and cut to represent both the red and the green in each rock sample for a better understanding of the redox interfaces and evident comparison of the color changes. Petrography via optical microscopy, SEM, and EDS revealed weathered and altered minerals within the Cutler rocks. Minerals observed in the Cutler rocks are consistent with Werner (1974) and includes quartz, micas, rock fragments, feldspars (Na and K), sparse laumontite, iron-oxide grains, various clays, gypsum and authigenic calcite as well as heavy-minerals: epidote (var. allanite in some samples), chlorite, tourmaline, rutile, titanite (sphene), ilmenite, zircon, magnetite, manganese oxide and maybe garnet (Werner, 1974). Micas were primarily determined to be biotite or a biotite alteration to clay; however,

minor muscovite is present in some samples. Fe-oxide grains are pervasive throughout all samples, including hematite ranging up to 500 μm (Fig. 6). Gypsum cement is present in one sample, 1218-03 Green (Fig. 16).

The red bed mineralogy appears finer grained and more compacted than that of the green strata; however, all grains are texturally immature and very angular to sub-angular (Fig. 15). Evidence for compaction is abundant, especially with the parallelization of biotites throughout the samples that appears to result from more than just their preferred orientation obtained through deposition (Fig. 15). Biotite was determined via the typical green-brown pleochroism in ppl and birds-eye extinction in xpl on an optical microscope, followed by SEM and EDS. Pleochroic intensity, strong brown- green colors in plane light, can indicate higher iron content in biotite (Fig. 17).

4.2.2 Biotite alteration

Biotite alteration is prevalent throughout the Cutler Formation as secondary mineral intergrowths and the formation of clay minerals. The primary mineral alteration comprises varying degrees of iron-oxide replacing biotite, or “dusting”, where the iron-oxide replacement ranges from micron size growths in the interlayers to complete biotite replacement by iron-oxide (Fig. 18). Other secondary biotite mineral intergrowths include quartz, apatite, titanite, rutile, fluorite, fluorapatite, and calcite (Fig. 19). The iron-oxide, titanite, apatite, and quartz replacements occur in the red, green, and bleached colorations. Secondary calcite intergrowths occur between biotite interlayers in proximal sample 53 III-14A in both the red and green with and without iron-oxide replacement. Rutile, barite, fluorite, and fluorapatite intergrowths occur only in green/bleached samples. 53S V-1 Green and 63S IV-27 Green host evidence of biotite chloritization (Fig. 19, A).

4.2.3 Authigenic mineral formation

Epidote

Authigenic epidote formation is evinced via SEM in sample 1218-03 green (Fig. 20). The epidote hosts no signs of weathering and is forming within the clay matrix of the sample. Epidote is surrounded by a Na-Mg rich clay and is growing in tandem with a biotite alteration to clay. Epidote formation from biotite alteration requires the addition of calcium, perhaps supplied by feldspar dissolution, and hydrothermal fluids >220ºC (Tomasson and Kristmannsdottir, 1972; Parneix et al., 1985). All detrital epidote occurrences in multiple Cutler Formation samples exhibit signs of mechanical weathering (i.e. fractures).

Chlorite

Chlorite is found as both primary detrital grains and a result of in-situ biotite chloritization and chemical alteration. Samples in contact with/ or near the basement at the mouth of Unaweep Canyon have the highest chlorite content based on XRD results. These samples also host the evidence of biotite chloritization, but other samples noted to contain chlorite via XRD simply host spherulitic chlorite throughout the sample, typically in association with biotite (Fig. 21). This does not discount detrital chlorite since chlorite is also found in the potential source rock, 1218-26D.

Ti-bearing minerals

Titanium is pervasive in different forms throughout the samples but more specifically is its unique associations in the green/bleached samples such as Ti-bearing clays and biotites. In addition, rutile (TiO_2) is only found as biotite intergrowths in green and bleached samples which alludes to a reducing fluid event in the rock history due to the removal of Fe but persistence of Ti

during the proposed mobilization from biotite to rutile (Fig. 19). Sample 1218-15 Bleach hosts Fe-Ti-oxide rims around quartz and biotite in the presence of Fe-rich clay that follows an apparent preferential flow pathway for alteration fluids (Fig. 22).

Gypsum and Barite

Some samples in the formation exhibit signs/ evidence of a past oxidizing sulfate-bearing fluid system. Sulfur-rich sample 1218-03 Green contains gypsum cement, sulfur-bearing clays, and thenardite, an anhydrous sodium sulfate (Fig. 23). Sample 53S V-1 has barite crystals plus barite intergrowths in biotite (Fig. 24).

4.3 Grain-size

The grain-size variations between the RGB sediments were tested on 10 representative samples using LPSA and supplemented with EDS mapping and petrography (Fig. 25). LPSA results are displayed as volume and number of particles (<2 mm) in Table 4. Mode is the grain size that occurs most frequently and Dx (90) is the largest grain size accounting for 90% of the total respective volume or particle number. Volume % and number % are used together for analysis because large grains can skew the volume density. This is evidenced by sample 1218-09 where the grain-size volume of the green rock appears to host smaller grains relative to the red counterpart. However, the number of coarser particles is larger in the green part of this sample, supporting the interpretation that the green rock is coarser than the red rock. All the other samples tested have a higher volume and number of larger size classes in green and bleached layers than red layers. Additionally, coarse sand-gravel grains, >2mm, are present within the green and bleached rocks that are not present within the red rocks. However, the coarser, greater than 2mm grains, had to be separated off for LPSA analysis and thus are not represented within

this data set. Based on volume and number of particles, the grain-size results show the green and bleached sediments are coarser grained than the red sediments. EDS mapping was performed on representative sample 53 III-14A to illustrate these grain-size variations across the red/green interface (Fig. 26). There are similar volume percentages of biotite as determined via XRD; however, the biotite grains are roughly 1000 μm in the green and 100 – 200 μm in the red. Additionally, optical petrography of sample 1218-15RB provides another example of the larger, coarser grained green versus finer grained red rock across the redox interface (Fig. 27).

4.4 Comparison of typical RGB sample mineralogy with whole-rock geochemistry

In addition to bulk mineralogy via XRD, three key proximal samples (1218-03 Green, 1218-15 Bleach, and 1218-15 Red) were further chosen for whole-rock geochemistry because their color and associations with each other generally represent the rest of the sample set. According to XRD bulk mineralogy, sample 1218-03 green contains almost 10x more smectite but less illite/mica than the bleached and red samples (Fig. 28). Sample 1218-15 red and bleached contain comparable mineral abundances relative to each other however the red sample overall has more illite/mica and hematite than the other two samples. The smectite: illite/mica ratios are worth noting because illite/mica can transform/alter to smectite and chlorite.

Whole-rock geochemical analyses of splits from the same three RGB samples (performed by ALS Mineralogy) demonstrate most major and trace elements are present with similar concentrations (Table 5). However, notable differences include: (1) the green and bleached rocks have approximately half as much total iron as the red, 2.98 wt.%, 3.19 wt.%, and 6.49 wt.% respectively, (2) the green sample has much higher Fe(II)/Fe(III) (green 51.8% > bleached 36.3% > red 29.5%), and (3) the green sample has considerably higher uranium (green 14.35 > red 2.26 > bleached 1.82 ppm U).

5. DISCUSSION

Proximal green and bleached strata result from several geologic features that likely impacted their origin and evolution: (1) the southwestern mouth of (modern) Unaweep Canyon, (2) the contact with underlying Precambrian bedrock, (3) regional buried and surficial fault systems that define the edge of the Uncompahgre Plateau, and (4) fluvial-alluvial depositional environment. Paragenetic evaluation unravels the potential effect(s) of these features in relation to hydrothermal fluid conduits, diagenesis, deposition, and stratigraphic location (Fig. 29). Upon understanding of mineral transformations from various alteration mechanisms or depositional systems, we can draw implications for uranium immobilization throughout the proximal Permian Cutler Formation.

5.1 Authigenic mineral formation mechanisms

Authigenic minerals in the red Cutler strata include hematite and calcite plus quartz, hematite, calcite, apatite, and titanite as secondary biotite intergrowths. The authigenic minerals in the green Cutler rocks are epidote, calcite, hematite, gypsum, barite, thenardite (Na-sulfate), and a host of secondary biotite mineral intergrowths including those in the red layers plus rutile, fluorite, fluorapatite, titanite, and barite. Bleached samples only host secondary biotite intergrowths and calcite (detected so far). Authigenesis of hematite, gypsum, barite, and thenardite requires oxidizing conditions.

5.1.1 Biotite – Corrensite –Chlorite + Epidote

The proximal Cutler Formation hosts abundant biotite in all three RGB colors. Biotite (trioctahedral mica) is more easily destroyed than muscovite (dioctahedral mica) via the loss/replacement of K^+ ions (Meunier, 2005). This process enables the transformation of biotite

to clay minerals, specifically biotite → chlorite (biotite chloritization) and biotite → vermiculite → smectite (Meunier, 2005). If percolating fluids are charged with Ca^{2+} and Mg^{2+}, the generalized transformation is as follows (Meunier, 2005):

(1) Biotite → vermiculite → smectite → randomly ordered ML clays → regularly ordered ML clays (corrensite) → illite → chlorite + epidote → epidote + actinolite

Note that not all transformations need to occur in a step-wise process to form certain clays (i.e. biotite to chlorite can be a direct transformation). Vermiculite and actinolite are not present in the Cutler samples. Biotite transformations are interpreted to have provided some of the cations necessary for authigenic mineral growths.

Biotite is less abundant in the green rocks which could reflect either: (1) less initial biotite in the coarser grained layers during deposition or (2) biotite alteration to other minerals such as mixed-layer clays, chlorite (biotite chloritization), and epidote. Biotite is altered in most samples which include secondary mineral intergrowths and clay genesis + epidote. The amount of epidote in the Cutler samples is higher in the green (1.6-7.6%) and red (2.5%) rocks than in the basement rocks (0.3-1.3%) from which they were derived, suggesting authigenic epidote formation + detrital epidote. SEM images provide evidence of authigenic epidote formation in association with intermediate biotite alteration and Na-Mg-bearing clay (Fig. 20). The authigenic epidote is 20 μm and grew within the clay layers. Detrital epidote is also visible via SEM with grain sizes up to ~400 μm and small fractures from slight mechanical weathering (Fig. 19). Epidote is only present in one red sample, 1218-24, from XRD results and is inferred as detrital.

Epidote, $Ca_2(Al, Fe)_3Si_3O_{12}(OH)$, contains ferric iron ($Fe^{3+}$) as an aluminum substitution (Myer, 1965). Ferric iron typically contributes to red coloration (i.e. hematite) because of its face-sharing octahedra that adsorb slower wavelengths of light (red). Epidote, however becomes green- dark green when the amount of Fe^{3+} substitution increases because it increases the unit cell edge volume (Myer, 1965). Edge sharing, as opposed to face sharing, contributes to yellow-green-brown colors from different wavelength adsorptions as in the case of epidote. Epidote could therefore partly contribute to green coloration under oxidizing conditions. The general chemical composition of epidote in the Cutler samples is: $Ca_{2.12}(Al_{1.73},Fe_{1.35})Si_{3.13}O_{12}(OH)$. The formation of Fe-rich epidote requires temperatures of at least 220ºC, consistent with hydrothermal fluids as the cause for authigenic epidote to form in the presence of biotite dissolution (Tomasson and Kristmannsdottir, 1972; Parneix et al., 1985).

Corrensite formation begins ~100ºC and loses its stability above 280ºC; however, lack of corrensite does not necessarily indicate temperatures outside this range (Velde, 1977; Parneix et al., 1985; Morrison and Parry, 1986). Typically, chlorite-smectite mixed layers indicate neutral to alkaline hydrothermal fluid conditions (Velde, 1995). Some of the Cutler samples have transformed from biotite to corrensite whereas other samples have transformed completely to chlorite. Corrensite may only be present in certain samples because of an abundance of available cations that fit into octahedral coordination (Al, Fe(II), Fe(III), and Mg) in those areas of the rock acting as “microsystems” since the rocks are not homogeneous (Meunier, 2005).

The chemistry of the octahedral sheet in the smectite and three different octahedral sheets in corrensite may provide clues to its origin and/or the nature of alteration fluids. Dutta and Suttner (1986) noted abundant smectite in the Cutler Formation and assumed it must be Mg-smectite. They interpreted red-bed associated chlorite as forming early after burial, making Mg-

rich solutions likely. However, it does not appear they investigated the chemistry of the chlorites or smectites, nor do they present XRD (060)-region data. On the other hand, Morrison and Perry (1986) investigated clay minerals in the Cutler Formation from bleached zones along the Lisbon fault (across the Paradox Basin from Unaweep ~80 km away; similar to the study area of Reynolds et al., (1985)). They found authigenic Al-rich smectite and corrensite (di/di octahedral, or 'tosudite') that they associated with acidic hydrothermal fluids traveling upwards along the fault and reacting with aluminous phases such as kaolinite or K-feldspar.

In the proximal Cutler samples investigated in this study, isolated 'pure' phases of smectite or corrensite were difficult to locate in thin sections. Smectites identified by EDS analysis are Al-rich (Al >> Mg > Fe) and dioctahedral, matching the (060) spacings observed in XRD spectra from random mounts of the clay fraction. Pure corrensite from the basement fracture-fill is tri-di-octahedral based on the (060) d-spacings, 1.538 Å and 1.507 Å respectively. Subsequent of corrensite is the formation of chlorite and epidote, see epidote equation above (Meunier, 2005). EDS spectra suggest the mixture of high Al, Mg, and Fe, suggesting a tri/di composition. If the clays formed in the sequence smectite → corrensite → chlorite, then the Al-rich dioctahedral layer might be inherited from the smectite, with the addition of Mg and Fe leading to the formation of tri/di corrensite, or sudoite. Eberl (1978) found mixed layer tri/di corrensites can form directly via hydrothermal alteration of dioctahedral smectites without intermediate randomly-interstratified clays. On the other hand, Jiang and Peacor (1994) demonstrated the alteration of biotite to corrensite and chlorite by the interstratification of dioctahedral clays in low-grade metamorphism of pelites, suggesting this is a possible mechanism of corrensite and chlorite formation from hydrothermal fluid in the Cutler Formation.

Diagenetic corrensite is uncommon because it requires unique conditions (i.e. neutral to alkaline pH and excess dissolved octahedral cations) therefore the corrensite in our system is interpreted to result from hydrothermal fluid. Pure corrensite found within fracture filling clay in a basement rock core, sample MC-01-1078, further supports hydrothermal fluid pathways along faults and fractures which served as conduits into the Cutler Formation. Furthermore, tri/di corrensite (sudoite) is typically associated with hydrothermal alteration along faults and contacts with bedrock and has been identified with unconformity-type uranium deposits (Percival et al., 1993; Kotzer and Kyser, 1995; Cloutier et al., 2010; Riegler et al., 2014). Further investigation of clay octahedral sheet chemistry in further studies of the proximal to distal (presumably unaltered) Cutler Formation would help to clarify the nature and significance of the smectite, corrensite, and chlorite chemistries.

Chlorite is found throughout the samples and in the basement rock, therefore some of the chlorite is interpreted as detrital (Fig. 11). Evidence of biotite chloritization in the green rocks close to or in contact with the basement rock is hypothesized to be an authigenic process from hydrothermal fluids percolating along this contact. Thus, the Cutler rocks contain authigenic and detrital chlorite. Additionally, biotite chloritization occurs between 220 – 280 ºC therefore fluid temperatures must have been between 220 – 280 ºC based on biotite chloritization and authigenic epidote formation during hydrothermal alteration, regardless of corrensite (Parneix et al., 1985; Velde, 1995).

5.1.2 Transformation of inherited biotite in response to fluid alteration

The biotite ranges in chemical and textural alteration from relatively unaltered to completely replaced forms that are altering to clays as a result of hydrothermal fluid alterations. The chemical alteration is primarily evident via iron and magnesium content plus the loss of K^+

ions and addition of Al into the octahedral sheet as in sample 53-14C Green: $K_{0.8}(Mg_{1.2}, Fe_{1.2}, Al_{0.6})(Si_{3.2}, Al_{0.8})O_{10}(OH)_2$. Aluminum incorporation could also indicate Al-smectite layers within the biotite. The textural alteration appears as a range of clean to frayed/ "exploded" biotites. Secondary mineral intergrowths are present as rutile, quartz, titanite, calcite, hematite, barite, apatite, and fluorapatite. Barite intergrowths occur near gypsum and thenardite, plus S-bearing clay mineralization in green-bleached samples near the Colorado-Utah boarder. Sulfate abundance is from recent oxidative weathering after erosion and re-exposure of the Cutler Formation, a post hydrothermal fluid alteration event (Shawe, 2011). Quartz, apatite, hematite, calcite, and titanite intergrowths occur in both the red and green rocks therefore they must have formed before reduction, from oxidizing fluids during diagenesis. Ixer, Turner, and Waugh (1979) proposed that hematite and rutile (+titanite) are formed as intergrowths from intrastratal dissolution of Fe and detrital Ti-oxide grains, respectively. Titanite and calcite further imply calcic fluids to accommodate their formation.

5.1.3 Hematite- an indicator for rock color development

Our research suggests the Cutler Formation was not deposited red but instead was deposited without any distinct coloration. However, fine particle hematite formation during oxidation at the time of deposition can't be discounted based on this study alone. Hematite exists in the form of individual coarse grains (authigenic or potentially pyrite pseudomorphs), grain-coatings, and various stages of secondary biotite intergrowths (Fig. 18). The bleached samples are void of Fe-oxide, which is suggested to have been stripped from the red beds by hydrothermal fluids during the Tertiary La Sal magmatic event (Lipman et al., 1976; Shawe, 2011). Iron stripping would have occurred via reduction of insoluble Fe(III) to soluble Fe(II)(aq). The solubilized Fe(II) then transported some distance or deposited in the adjacent red layers.

During the magmatic event, magmatic fluids mixed and heated formation fluids in the Paradox Basin and thus drove them up along faults and fractures, into the proximal Cutler Formation (Shawe, 2011).

The parent rocks do not host the large (up to 500 μm) hematite grains that are pervasive throughout the RGB (bleached determined via SEM) rocks but they do contain secondary hematite intergrowths within biotite. These intergrowths within basement rock biotite must emanate from the same fluid influx seen in the red beds after diagenesis. The formation is hypothesized to have been oxidized (red) post-deposition during diagenesis based on hematite rimmed quartz grains and coarse-grained authigenic hematites that are potentially pyrite pseudomorphs or martite. The red beds in their final transformation host green-bleached interfingering from reducing, intermediate hydrothermal fluids. This poses a generalized model that Cutler sediments were: (1) deposited without unique coloration, (2) diagenetically altered and oxidized red, and then (3) reduced by hydrothermal fluids (Fig. 30). An alternate model for reddening of Cutler sediments that can't be discounted is: (1) pigmentary hematite formed during syn-depositional weathering, (2) further hematization occurred during diagenesis, followed by (3) reduction via hydrothermal fluids to form green and bleached layers.

5.2 Diagenetic Influences

Understanding diagenetic impacts on the Cutler Formation is important for discrimination of hydrothermal fluid alteration. Dutta and Suttner (1986) indicated that burial did not exceed the depths required for late-stage diagenetic mineral destruction (i.e. burial did not exceed 2400 m). The RGB rocks host similar mineralogies but more specifically, the red and green rocks contain Fe-oxide (hematite) whereas the bleached and basement rocks are void (<1%) of it in XRD. Fe-oxide coated grains occur in the green samples via SEM (Fig. 11 and 18) which suggests the

rocks were red (oxidized) before they were later reduced. The Cutler Formation red beds are hypothesized to have formed their hematite pigment from diagenetic alteration of iron-oxide silicate grains (Elmore and Van der Voo, 1982). This implies that the red beds were not red when they were deposited (Ixer, Turner, and Waugh, 1979).

Dutta and Suttner (1986) assumed that early diagenetic pore fluid was Mg- and Si- rich, which caused the formation of authigenic Mg-rich smectite from reaction with concentrated pore waters in an arid climate. Although their study confirms the similar presence of pervasive smectite in the <2 μm clay fraction throughout most of the proximal Cutler samples, two key differences provide insights to the diagenetic versus hydrothermal alteration history: (1) smectite composition and (2) mutually-exclusive presence of smectite and mixed-layer illite-smectite.

SEM-EDS measurement of smectite in the proximal Cutler Formation indicates (dioctahedral) Al-rich smectite, rather than the Mg-smectite (presumably trioctahedral based on their formation mechanism, evaporative concentration in alkaline porewaters, (e.g., Deocampo et al., 2004)) proposed by Dutta and Suttner (1986). Importantly, Al-rich smectite forms via low-temperature (e.g., Zhu et al., 2006) or hydrothermal (Inoue, 1995) alteration of siliciclastic systems under neutral to mildly alkaline conditions. This leads to testable hypotheses regarding the octahedral sheet chemistry of proximal to distal smectites and their relationship to climate and fluid alteration.

Typically, as burial increases and temperatures exceed 100ºC, smectite loses its stability and transforms to illite. However, the transformation sequence includes intermediate phases of randomly ordered and regularly ordered mixed-layer illite-smectite (I/S), respectively (Meunier, 2005). Mixed-layer clays occur sporadically throughout the formation; notably, illite/smectite mixed layer clays were detected in 8 out of 39 samples. Discrete smectite was present in only 2

of the 8 I/S-bearing samples but in 29/39 oriented mounts investigated in this study, suggesting an inverse relationship between the presence of smectite and mixed-layer I/S. Three potential explanations for this relationship are (1) hydrothermal alteration partially illitized smectite, (2) the "illite/smectite" is actually mixed-layer biotite/smectite as an intermediate stage in formation of corrensite/ sudoite, or (3) diagenetic compaction created microsystems, separating parts of the formation from other areas that better preserved these mixed layer clays. Furthermore, smectite content drastically decreases over geologic time such that formation ages of Eocene- present yield 40-60% smectite but ages in the Paleozoic (i.e. Permian) do not exceed 10% (Thompson and Hower, 1975; Meunier, 2005).

When comparing the clay mineralogy of the green-bleached rocks to their red counterparts, the green-bleached samples consistently host more smectite than the red samples. This suggests that the abundant pure smectite in our system is younger than Eocene and likely a result of hydrothermal fluid alteration, whereas the mixed-layered smectites are remnant from diagenetic pore fluids (Dutta and Suttner, 1986). Hydrothermal smectite forms from intermediate fluids with a pH >7 while at pH <7, kaolinite forms (Jacobs and Kerr, 1965; Chamley, 1989; Meunier, 2005). In regard to pH, intermediary fluid mineral zones with (1) K cations and (2) Ca +Mg cations are as follows, with respect to increasing temperature (Meunier, 2005 after Utada, 1980):

(1) Smectite → I/S mixed layers → Illite → K-spar

(2) Smectite → I/S and C/S mixed layers → Chlorite + Epidote → Epidote + Actinolite

Strictly acidic and alkaline fluids produce clay minerals that are not present in our samples; the lack of kaolinite in our system refutes the possibility of acidic fluids. Since smectite transforms

at elevated temperatures over time, the illite-smectite mixed layers in our system are a result of diagenesis. Chlorite-smectite mixed layers are diagnostic of neutral to alkaline hydrothermal fluid conditions (Velde, 1995).

The Cutler Formation also exhibits evidence of mechanical compaction, primarily with parallel biotite grains throughout the formation from diagenetic alteration. Burial compaction records exposure to higher temperature because as pressure increases with depth, so does temperature (Velde, 1995; Meunier, 2005). The geothermal gradient of the continental crust is ~30ºC/km (Velde, 1995; Meunier, 2005). In addition, compaction creates a closed system wherein fluid composition becomes controlled by equilibrium with the surrounding minerals (Meunier, 2005).

5.3 Depositional Impacts

A proglacial depositional environment could have influenced the contribution of chlorite to the Cutler Formation that was mechanically weathered from the underlying parent rock during glacial carving. An over-deepened, paleovalley, hypothesized by Soreghan et al (2015) to be the result of glacial carving lies a few kilometers from the proximal Cutler Formation, buried in the subsurface of modern Unaweep Canyon. Discrimination of nonglacial fluvial and proglacial fluvial deposits is difficult because they have similar indicators. Either of these depositional environments may have caused grain-size variations, leading to coarse-grained green-bleached rocks with fine-grained red rocks. This allowed hydrothermal fluids from local faults and fractures to take a preferential flow path through the more permeable green-bleached sediments and stripped them of some of their hematite/ Fe (III) oxides (Fig. 3). The Cutler Formation is also in contact with basement rock therefore fluids could have percolated along the basement contact and created the dark green, coarse-grained rocks. These rocks are also high in chlorite

therefore suggesting hydrothermal fluids traveling along this contact influenced authigenic chlorite, evidenced as biotite chloritization. The bleached sediments were almost completely stripped by the fluids, but the reduced green zones were only partially affected, leaving residual hematite as separate crystallites and intergrowths in oxidized micas. The contrast between the green and bleached is inferred to reflect higher permeability and larger grain-sizes in the bleached layers than in the green layers; however the residual Fe-oxide in the green layers could also result from higher initial Fe-oxide content. The green-bleached rocks were also influenced by oxidative weathering when the formation was re-exposed, which changed the mineralogy and caused sulfate formation.

The hypothesized paleovalley in association with Unaweep Canyon is thought to be overdeepened in the subsurface, and thus a reflection of glacial activity in the deep-time (presumably late Paleozoic) past. Studies of weathering associated with modern valley glaciation suggests the unique signatures of proglacial valley groundwaters are oxidative solutions with elevated sulfate and Ca (Salerno et al., 2016; Torres et al., 2017). Generally, proglacial groundwaters contain dissolved oxygen, but are often somewhat undersaturated with respect to atmospheric O_2 (Brown et al., 1994; Tranter and Wadhawan, 2014). In contrast, weathering under larger ice sheets tends to be associated with the development of anoxia and reducing groundwaters (Wadham et al., 2010; Graly et al., 2014; Andrews and Jacobson, 2018). If the greening and bleaching in the proximal Cutler Formation were associated with anoxic proglacial groundwaters, then the development of RGB features in the Cutler Formation should be syn-depositional, rather than post-burial diagenesis. Although biotite alteration was observed to be significant both in this study and at the foreland of a retreating glacier (Anderson et al., 2000), the observed authigenic mineralogical signatures in the proximal Cutler Formation are not

consistent with reduction in low-temperature meteoric solutions, and no conclusion can be drawn on the climate at the time of deposition of the proximal Cutler Formation.

5.4 Grain-size effects on permeability: Implications for hydrothermal fluid pathways

If the green rocks contain a greater proportion of Fe(II), reduced iron, then it could signify the potential for the occurrence of reduced metals such as U(IV). The grain-size variations within the Cutler Formation from coarse- to fine grained are: bleached > green>> red. The grain-size variations resulted from a fluvial-alluvial depositional environment in the early Permian (~290 Ma). The red beds primarily host angular-subangular silt-mudstone grains and the green-bleached sediments host coarse-grained siliciclastics. Based on the authigenic mineral alterations revealed by SEM, EDS, and XRD, the bleached and green layers are more permeable than the red layers and therefore served as preferential fluid pathways. The bleached and mint green coloration is from high-temperature hydrothermal fluids, groundwater, or a mix of both that flowed through the relatively coarser-grained, more-permeable layers (Morrison and Parry, 1986).

5.5 Implications for uranium immobilization

Uranium accumulated in overlying Mesozoic units (i.e. the upper Moenkopi, Chinle, and Morrison formations) implying potential for uranium deposition in the underlying Cutler Formation (Finch, 1963; Campbell, 1981). Indeed, uranium occurrences are noted in the distal red beds of the Cutler Formation, away from the sediment source proximal to Unaweep Canyon (Campbell, 1981). The proximal Cutler facies are more indicative of paleovalley-type deposits in that they have been previously characterized as a braided fluvial system burying crystalline basement rock (Campbell, 1981; Hou et al., 2017). Uranium leaching from basement rock that is

in contact with percolating fluids was potentially expelled along fault zones into the nearby proximal Cutler Formation. Hou et al. (2017) noted that ideal characteristics of siliciclastic uranium deposits are fine to coarse-grained sands derived from fluvial-alluvial deposition. Unexplored before this is the additional factor of oxidized/reduced fluid influx through the proximal Cutler strata and the resulting RGB redox interfaces that support the potential formation of a uranium paleovalley deposit in the Cutler Formation (Hou et al., 2017).

5.5.1 Uranium paleovalley formation mechanisms

Sandstones require their own unique set of specific parameters to trap uranium which are: 1) A protective barrier to oxidation, 2) A primary uranium source, and 3) a reductant (Hou et al., 2017). The proximal Cutler Formation is therefore idealized here as a potential siliciclastic, uranium-hosted paleovalley deposit. General elements of such a deposit include: "sediment and uranium sources, geologic setting, depositional environment, age, and relative timing of mineralization, aquifer characteristics, availability and distribution of reductants, and preservation potential of the uranium mineral system" (Hou et al., 2017). An unexplored critical component to our system is the reduction of oxidized uranium-bearing fluids, perhaps via Fe(II) release from reaction with ferromagnesian minerals (i.e. chlorite and biotite) (Hou et al., 2017). Previous studies have indicated abundant authigenic chlorite within the Cutler rocks that could be derived from hydrothermal fluid activity (Suttner and Dutta, 1986; Shawe, 2011). Our results indeed indicate (1) Fe(II)/Fe(III) ratios likely increase in green layers as expected with the color difference; however, local conditions associated with outcrop and microsystem-scale features can change results of fluid alteration; (2) the green layers likely do scavenge U from groundwaters as revealed by the whole-rock geochemistry; and (3) authigenic smectites are Al-rich, but authigenic corrensite and chlorite likely include Fe(II)-Mg. If the proximal Cutler

Formation satisfies the necessary conditions for geochemical sequestration of uranium, then we will have provided a new model for uranium sequestration not previously identified in the region.

6. CONCLUSION

The proximal Permian Cutler Formation has undergone a complex depositional history. The formation accumulated in a fluvial-alluvial-dominated environment which remains a hot topic of debate today (e.g., Soreghan et al., 2009). Regardless of the exact environmental interpretation, deposition resulted in significant grain-size variations in the strata. The formation was then subjected to burial diagenesis at depths of up to 2400 m, leading to slight compaction throughout the formation. Oxidative diagenesis created iron-oxide (hematite) rimmed grains that likely turned the formation red after deposition throughout the formation. The grain-size variations then enabled post-depositional preferential fluid flow through the coarser-grained, more permeable layers that resulted in color variations of red, green, and bleached. Magmatic fluids were released during the Tertiary from the La Sal laccolith that subsequently mixed and heated formation fluids in the Paradox Basin. These reduced fluids then emanated up from the Paradox Basin along faults, fracture zones, and the basement rock contact, into the Cutler Formation. Perhaps these fluids mixed with lower-temperature groundwaters flowing out from Unaweep canyon and/or the overlying Mesozoic formations. The result of these fluid pathways was the RGB redox interfaces. Authigenic minerals that formed from the fluids are epidote, corrensite, chlorite, calcite, illite, and secondary mineral intergrowths. The formation was then eroded and exposed to weathering which triggered sulfate formation.

Evaluation of the RGB redox interfaces and their paragenesis within these Permian red beds have not been previously studied. Study of the detailed mineralogy of the rocks enabled

unravelling of the sequence of events and identification of general fluid composition(s), temperature(s), and metal immobilization capacity in the reduced strata. The fluid composition creating green and bleached layers must have been reducing and intermediate (pH 6-8), with temperatures of 220-280ºC. Intermediate hydrothermal fluid during the Tertiary magmatic event flowed along faults and fractures, especially into sediment/rocks in contact with basement rock which acted as a fluid conduit (Meunier, 2005). Grain-size variations confirmed the green-bleached colors resulted from fluid alteration that reduced Fe(III) to Fe(II). The reductive capacity to reduce iron suggests metals (i.e. U) can be immobilized within the green, reduced layers.

REFERENCES

Anderson, S., Drever, J., Frost, C., and Holden, P. (2000). Chemical weathering in the foreland of a retreating glacier. *Geochimica et Cosmochimica Acta, 64(7)* 1173–1189.

Andrews, M., and Jacobson, A. (2018). Controls on the solute geochemistry of subglacial discharge from the Russell Glacier, Greenland Ice Sheet determined by radiogenic and stable Sr isotope ratios. *Geochimica et Cosmochimica Acta 329,* 312-329.

Aslan, A., Hood, W. C., Karlstrom, K. E., Kirby, E., Granger, D. E., Kelley, S., & Asmerom, Y. (2014). Abandonment of Unaweep Canyon (1.4–0.8 Ma), western Colorado: Effects of stream capture and anomalously rapid Pleistocene river incision. *Geosphere*, *10*(3), 428-446.

Baars, D. L., and Stevenson, G. M., (1981). Tectonic evolution of the Paradox Basin, Utah and Colorado, in Wiegand, D.L., ed., *Geology of the Paradox Basin, Rocky Mountain Association of Geologists, Field Conference*, p. 23–31.

Balco, G., Soreghan, G. S., Sweet, D. E., Marra, K. R., … & Bierman, P. R. (2013). Cosmogenic-nuclide burial ages for Pleistocene sedimentary fill in Unaweep Canyon, Colorado, USA. *Quaternary Geochronology*, *18*, 149-157.

Bankey, V. (2003). *Resource potential and geology of the Grand Mesa, Uncompahgre, and Gunnison (GMUG) National Forests and vicinity, Colorado* (No. 2213).

Bankole, O. M., El Albani, A., Meunier, A., Rouxel, O. J., Gauthier-Lafaye, F., & Bekker, A. (2016). Origin of red beds in the Paleoproterozoic Franceville Basin, Gabon, and

implications for sandstone-hosted uranium mineralization. *American journal of science*, *316*(9), 839-872.

Bargar, J. R., Williams, K. H., Campbell, K. M., Long, P. E., Stubbs, J. E., Suvorova, E. I., ... & Davis, J. A. (2013). Uranium redox transition pathways in acetate-amended sediments. *Proceedings of the National Academy of Sciences*, *110*(12), 4506-4511.

Biscaye, P. E. (1965). Mineralogy and sedimentation of recent deep-sea clay in the Atlantic Ocean and adjacent seas and oceans. *Geological Society of America Bulletin*, *76*, 803-832.

Brindley, G. W., & Brown, G. (1980). Quantitative X-ray mineral analysis of clays. *Crystal structures of clay minerals and their X-ray identification*, *5*, 411-438.

Brookshaw, D. R., Pattrick, R. A., Bots, P., Law, G. T., Lloyd, J. R., Mosselmans, J. F. W., ... & Morris, K. (2015). Redox interactions of Tc (VII), U (VI), and Np (V) with microbially reduced biotite and chlorite. *Environmental science & technology*, *49(22)*, 13139-13148.

Brown, G. H., Tranter, M., Sharp, M. J., Davies, T. D., and Tsiouris, S. (1994). Dissolved oxygen variations in alpine glacial meltwaters. *Earth Surface Processes and Landforms*, *19*, 247–253.

Campbell, J. A. (1981). Uranium mineralization and depositional facies in the Permian rocks of the northern Paradox Basin, Utah and Colorado, *in* Weigand, D. L., ed., Geology of the Paradox Basin: Rocky Mountain Association of Geologists, p. 187-194.

.

Case, J. E. (1991). Geologic Map of the Northwestern Part of the Uncompahgre Uplift, Grand County, Utah, and Mesa County, Colorado, with Emphasis on Proterozoic rocks. U.S. Geological Survey, Miscellaneous Investigations, Series I-2088, 16 p.

Cater Jr., F. W. (1955). Geology of the Gateway quadrangle, Colorado: US Geol. *Survey Geol. Quad. Map GQ-55*.

Cater, F. W., & Craig, L. C. (1970). Geology of the salt anticline region in southwestern Colorado. *U.S. Geological Survey Professional Paper*, 637.

Chamley, H. (1989). *Clay sedimentology / Hervé Chamley.* Berlin; New York: Springer-Verlag.

Chan, M. A., Parry, W. T., & Bowman, J. R. (2000). Diagenetic hematite and manganese oxides and fault-related fluid flow in Jurassic sandstones, southeastern Utah. *AAPG bulletin*, *84*(9), 1281-1310.

Chenoweth, W. L. (1996). The uranium industry in the Paradox basin, *in* Huffman, A. C., Jr., Lund, W. R., and Godwin, L. H., editors, Geology and resources of the Paradox basin: Utah Geological Association Publication, 25, p. 95-108.

Cloutier J., Kyser K., Olivo G., and Alexandre P. (2010). Contrasting Patterns of Alteration at the Wheeler River Area, Athabasca Basin, Saskatchewan, Canada: Insights into the Apparently Uranium-Barren Zone K Alteration System. *Economic Geology*, 303–324.

Cornell, R. M., & Schwertmann, U. (2003). *The iron oxides: structure, properties, reactions, occurrences and uses*. John Wiley & Sons.

Dahlkamp, F. J. (2010). *Uranium deposits of the world: USA and Latin America*. Springer Science & Business Media.

Deocampo, D. M. (2004). Authigenic clays in East Africa: regional trends and paleolimnology at the Plio–Pleistocene boundary, Olduvai Gorge, Tanzania. *Journal of Paleolimnology, 31*, 1–9.

Dorsey, R. J., & Lazear, G. (2013). A post–6 Ma sediment budget for the Colorado River. *Geosphere*, *9*(4), 781-791.

Drever, J. I. (1973). Preparation of oriented clay mineral specimens for x-ray-diffraction analysis by a filter-membrane peel technique. *American Mineralogist, 58,* 553–554.

Dubiel, R. F., and Smoot, J. P. (1995). Criteria for interpreting paleoclimate from red beds—a tool for Pangean reconstructions. In: Embry AF, Beauchamp B, Glass DJ (eds) Pangea: global environments and resources. *Can Soc Pet Geol Mem* 17:295–310

Dutta, P. K., & Suttner, L. J. (1986). Alluvial sandstone composition and paleoclimate; II, Authigenic mineralogy. *Journal of Sedimentary Research*, *56*(3), 346-358.

Eberl, D. (1978). Reaction Series for Dioctahedral Smectites. *Clay Clay Miner 26,* 327–340.

Eberl, D. D. (2003). *User guide to RockJock-A program for determining quantitative mineralogy from X-ray diffraction data* (No. 2003-78). US Geological Survey.

Elmore, R. D., & Van der Voo, R. (1982). Origin of hematite and its associated remanence in the Copper Harbor Conglomerate (Keweenawan), Upper Michigan. *Journal of Geophysical Research: Solid Earth*, *87*(B13), 10918-10928.

Finch, W. I. (1963). Geology of uranium deposits in Triassic rocks of the Colorado Plateau region. *Geological Survey Bulletin*, (1074), 125.

Finch, R., & Murakami, T. (1999). Systematics and paragenesis of uranium minerals. *Reviews in Mineralogy, 38,* 91-180.

Graly, J. A., Humphrey, N. F., Landowski, C. M., and Harper, J. T. (2014). Chemical weathering under the Greenland Ice Sheet. *Geology, 42,* 551–554.

Hedge, C. E., Peterman, Z. E., Case, J. E., & Obradovich, J. D. (1968). Precambrian geochronology of the northwestern Uncompahgre Plateau, Utah and Colorado. *US Geological Survey Professional Paper, 600,* C91-96.

Hou, B., Keeling, J., & Li, Z. (2017). Paleovalley-related uranium deposits in Australia and China: a review of geological and exploration models and methods. *Ore Geology Reviews, 88,* 201-234.

Houston, W., Wray, L., & Moreland, P. (2009). The Paradox Basin Revisited: New Developments in Petroleum Systems and Basin Analysis. Rocky Mountain Association of Geologists, 1–825.

Hubert, J. F., & Reed, A. A. (1978). Red-bed diagenesis in the east Berlin Formation, Newark group, Connecticut Valley. *Journal of Sedimentary Research, 48*(1), 175-184.

Inoue, A. (1995). Formation of Clay Minerals in Hydrothermal Environments. In: Velde B. (eds) Origin and Mineralogy of Clays. Springer, Berlin, Heidelberg.

Ixer, R. A., Turner, P., & Waugh, B. (1979). Authigenic iron and titanium oxides in Triassic red beds: (St. Bees Sandstone), Cumbria, northern England. *Geological Journal, 14*(2), 179-192.

Jacobs, M., and Kerr, P. (1965). Hydrothermal Alteration Along the Lisbon Valley Fault Zone, San Juan County, Utah. *GSA Bulletin, 76,* 423–440.

Jiang, W., and Peacor, D. (1994). Formation of corrensite, chlorite and chlorite-mica stacks by replacement of detrital biotite in low-grade pelitic rocks. *J Metamorph Geol, 12,* 867–884.

Keiser, L. J., Soreghan, G. S., & Kowalewski, M. (2015). Use of Quartz Microtextural Analysis to Assess Possible Proglacial Deposition for the Pennsylvanian–Permian Cutler Formation (Colorado, USA). *Journal of Sedimentary Research*, *85*(11), 1310-1322.

Keller, W. (1953). Illite and montmorillonite in green sedimentary rocks. *J Sediment Res, 23,* 3–9.

Kluth, C. F., & Coney, P. J. (1981). Plate tectonics of the ancestral Rocky Mountains. *Geology*, *9*(1), 10-15.

Kotzer, T. G., and Kyser, T. K. (1995). Petrogenesis of the Proterozoic Athabasca Basin, northern Saskatchewan, Canada, and its relation to diagenesis, hydrothermal uranium mineralization and paleohydrogeology. *Chemical Geology*, 45–89.

Kyser, K. (2014). Uranium ore deposits. *Treatise on Geochemistry (2nd ed.), 13,* 489-513.

Langmuir, D. (1978). Uranium solution-mineral equilibria at low temperatures with applications to sedimentary ore deposits. *Geochimica et Cosmochimica Acta*, *42*(6), 547-569.

Lipman, P. W., Fisher, F. S., Mehnert, H. H., Naeser, C. W., Luedke, R. G., & Steven, T. A. (1976). Multiple ages of mid-Tertiary mineralization and alteration in the western San Juan Mountains, Colorado. *Economic Geology, 71*(3), 571-588.

Lorens, R. B. (1981). Sr, Cd, Mn and Co distribution coefficients in calcite as a function of calcite precipitation rate. *Geochimica et Cosmochimica Acta*, *45*(4), 553-561.

MacCarthy, G. R. (1926). Colors produced by iron in minerals and the sediments. *American Journal of Science, 67,* 17-36.

Mack, G. H. (1977). Depositional environments of the Cutler-Cedar Mesa facies transition (Permian) near Moab, Utah. *The Mountain Geologist, 14,* 53-68.

Marra, K. (2008). Late Cenozoic geomorphic and climatic evolution of the northeastern Colorado Plateau as recorded by Plio-Pleistocene sediment fill in Unaweep Canyon, Colorado (M.S. thesis, University of Oklahoma).

Matheny, J. P., & Longman, M. W. (1996). Lower Desert Creek Reservoirs in the Paradox Basin: examples of phylloid algae filling depositional lows related to salt dissolution. N.W. Longman, M.D. Sonnenfeld (Eds.), *Paleozoic systems of the Rocky Mountain Region*, Rocky Mountain Section, SEPM, 267-282.

McBride, E. (1974). Significance of color in red, green, purple, olive, brown, and gray beds of Difunta Group, northeastern Mexico. *J Sediment Res, 44,* 760–773.

Meunier, A. (2005). *Clays*. Springer Science & Business Media.

Moore, D. M., & Reynolds, R. C. (1997). X-Ray Diffraction and the Identification and Analysis of Clay Minerals. *Oxford University Press*.

Morad, S., & Adin Aldahan, A. L. A. (1986). Alteration of detrital Fe-Ti oxides in sedimentary rocks. *Geological Society of America Bulletin*, *97*(5), 567-578.

Morrison, S. J., and Parry, W. T. (1986). Dioctahedral Corrensite from Permian Red Beds, Lisbon Valley, Utah. *Clays Clay Min 34*, 613–624.

Mose, D. G., & Bickford, M. E. (1969). Precambrian geochronology in the Unaweep Canyon, west-central Colorado. *Journal of Geophysical Research*, *74*(6), 1677-1687.

Myer, G. H. (1965). X-ray determinative curve for epidote. *American Journal of Science*, *263*(1), 78-86.

Noël, V., Boye, K., Kukkadapu, R., Bone, S., Pacheco, J., Cardarelli, E., Janot, N., Fendorf, S., Williams, K., and Bargar, J. (2017). Understanding controls on redox processes in floodplain sediments of the Upper Colorado River Basin. *Sci Total Environ*, *603*, 663–675.

Nuccio, V. F., & Condon, S. M. (1996). Burial and thermal history of the Paradox Basin, Utah and Colorado, and petroleum potential of the middle Pennsylvanian Paradox Formation.

Parneix, J. C., Beaufort, D., Dudoignon, P., and Meunier, A. (1985). Biotite chloritization process in hydrothermally altered granites. *Chem Geol*, *51*, 89–101.

Percival, J. B., Bell, K., and Torrance, J. K. (1993). Clay mineralogy and isotope geochemistry of the alteration halo at the Cigar Lake uranium deposit. *Canadian Journal of Earth Sciences*, 689–704.

Qafoku, O., Pearce, C. I., Neumann, A., Kovarik, L., Zhu, M., Ilton, E. S., ... & Felmy, A. R. (2017). Tc (VII) and Cr (VI) interaction with naturally reduced ferruginous smectite from a redox transition zone. *Environmental science & technology*, *51*(16), 9042-9052.

Reynolds, R. L., Hudson, M. R., Fishman, N. S., & Campbell, J. A. (1985). Paleomagnetic and petrologic evidence bearing on the age and origin of uranium deposits in the Permian Cutler Formation, Lisbon Valley, Utah. *Geological Society of America Bulletin*, *96*(6), 719-730.

Riegler, T., Lescuyer, J. L., Wollenberg, P., Quirt, D., and Beaufort, D. (2014). Alteration related to uranium deposits in the Kiggavik–Andrew lake structural trend, Nunavut, Canada: new insights from petrography and clay mineralogy. *Canadian Mineralogist, 52,* 27–45.

Salerno, F., Rogora, M., Balestrini, R., Lami, A., Tartari, G. A., Thakuri, S., Godone, D., Freppaz, M., and Tartari, G. (2016). Glacier Melting Increases the Solute Concentrations of Himalayan Glacial Lakes. *Environmental Science & Technol*ogy, *50*, 9150-9160.

Sanford, R. F. (1982). Preliminary model of regional Mesozoic groundwater flow and uranium deposition in the Colorado Plateau. *Geology, 10,* 348–352.

Shawe, D. R. (1976a). Sedimentary rock alteration in the Slick Rock district, San Miguel and Dolores Counties, Colorado. US Geol Surv Prof Paper 576-D, pp D1-D5.1.

Shawe, D. R. (2011). Uranium-vanadium deposits of the Slick Rock district, Colorado. *United States Geological Survey, Professional Paper, 576*, 80.

Sheldon, N. D. (2005). Do red beds indicate paleoclimatic conditions?: a Permian case study. *Palaeogeography, Palaeoclimatology, Palaeoecology*, *228*(3-4), 305-319.

Soreghan, G. S., Sweet, D. E., Marra, K. R., Eble, C. F., Soreghan, M. J., Elmore, R. D., ... & Blum, M. D. (2007). An exhumed late Paleozoic canyon in the Rocky Mountains. *The Journal of Geology*, *115*(4), 473-481.

Soreghan, G. S., Soreghan, M. J., Sweet, D. E., & Moore, K. D. (2009). Hot fan or cold outwash? Hypothesized proglacial deposition in the upper Paleozoic Cutler Formation, western tropical Pangea. *Journal of Sedimentary Research*, *79*(7), 495-522.

Soreghan, G. S., Sweet, D. E., Thomson, S. N., Kaplan, S. A., Marra, K. R., Balco, G., & Eccles, T. M. (2015). Geology of Unaweep Canyon and its role in the drainage evolution of the northern Colorado Plateau. *Geosphere*, *11*(2), 320-341.

Steiner, M. B., & Lucas, S. G. (2000). Paleomagnetism of the Late Triassic Petrified Forest Formation, Chinle Group, western United States: further evidence of "large" rotation of the Colorado Plateau. *Journal of Geophysical Research: Solid Earth*, *105*(B11), 25791-25808.

Streckeisen, A. (1974). "Classification and nomenclature of plutonic rocks recommendations of the IUGS subcommission on the systematics of Igneous Rocks". *Geologische Rundschau*. *63*(2): 773–786.

Suttner, L. J., & Dutta, P. K. (1986). Alluvial sandstone composition and paleoclimate; I, Framework mineralogy. *Journal of Sedimentary Research*, *56*(3), 329-345.

Thompson, J. A., Giles, K., Hearon, T. E., Trudgill, B., Rowan, M. G., and Langford, R. P. (2018). Halokinetic Features in the Paradox Basin, Utah and Colorado. In AAPG ACE 2018.

Thompson, G. R., & Hower, J. (1975). The mineralogy of glauconite. *Clays and Clay Minerals*, *23*(4), 289-300.

Thomson, S. N., Soreghan, G. S., Reiners, P. W., Peyton, S. L., & Murray, K. E. (2015). A Precise 6 Ma Start Date for Fluvial Incision of the Northeastern Colorado Plateau Canyonlands. In *AGU Fall Meeting Abstracts*.

Tómasson, J., & Kristmannsdóttir, H. (1972). High temperature alteration minerals and thermal brines, Reykjanes, Iceland. *Contributions to Mineralogy and Petrology*, *36*(2), 123-134.

Torres, M., Moosdorf, N., Hartmann, J., Adkins, J., and West, J. (2017). Glacial weathering, sulfide oxidation, and global carbon cycle feedbacks. *Proceedings of the National Academy of Sciences, 114,* 8716–8721.

Tranter, M., and Wadham, J. (2014). Geochemical Weathering in Glacial and Proglacial Environments. *Treatise on Geochemistry*, Elsevier. *7*, 157–173.

Turner, P., & Archer, R. (1977). The role of biotite in the diagenesis of red beds from the Devonian of northern Scotland. *Sedimentary Geology*, *19*, 241-251.

Utada, M. (1980). Hydrothermal alterations related to igneous activity in Cretaceous and Neogene formations in Japan. *Mining Geol., Spec. Issue*, *8*, 67-83.

Van Houten, F. B. (1973). Origin of Red Beds - Review, 1961-1972. *Annual Review of Earth and Planetary Sciences, 1,* 39–61.

Velde, B. (1977). *Clays and clay minerals in natural and synthetic systems* (Vol. 21). Elsevier.

Velde, B. (Ed.). (1995). *Origin and mineralogy of clays: clays and the environment*. Springer Science & Business Media.

Wadham, J. L., Tranter, M, Skidmore, M., Hodson, A. J., Priscu, J., Lyons, W. B., Sharp, M., Wynn, P., and Jackson, M. (2010). Biogeochemical weathering under ice: Size matters. *Global Biogeochem Cy*, *24*, GB3025.

Walker, T. (1974). Formation of Red Beds in Moist Tropical Climates - Hypothesis. *GSA Bulletin*, *85*, 633–638.

Werner, W. G. (1974). Petrology of the Cutler Formation (Pennsylvanian-Permian) near Gateway, Colorado, and Fisher Towers, Utah. *Journal of Sedimentary Research*, *44*(2), 292-298.

Worden, R. H., & Burley, S. D. (2003). Sandstone diagenesis: the evolution of sand to stone. *Sandstone Diagenesis: Recent and Ancient*, *4*, 3-44.

Zhu, C., Veblen, D., Blum, A., and Chipera, S. (2006). Naturally weathered feldspar surfaces in the Navajo Sandstone aquifer, Black Mesa, Arizona: Electron microscopic characterization. *Geochimica et Cosmochimica Acta, 70*, 4600–4616.

FIGURES

Fig. 1: Cutler Formation field photos of outcrops representing RGB interlayers and layering.

Top: Red/bleached interlayering. Bottom: Green and red/green interlayers.


Proximal
Dark Green
Proximal
Red/Green
Red/Bleached
Distal Red

Fig. 2: Representation of the RGB redox interfaces within the proximal Cutler Fm. The dark green rocks occur in contact with or near contact with igneous basement rock at the mouth of Unaweep Canyon. The proximal red-green also occur near basement rock however their occurrence spans laterally from the mouth of Unaweep Canyon to the Colorado-Utah boarder. The red/bleached do not occur within 1 km of the canyon mouth but do occur westward and the distal red which are void of green-bleached alterations span from 2 miles SW of the canyon to the west side of the Dolores river.

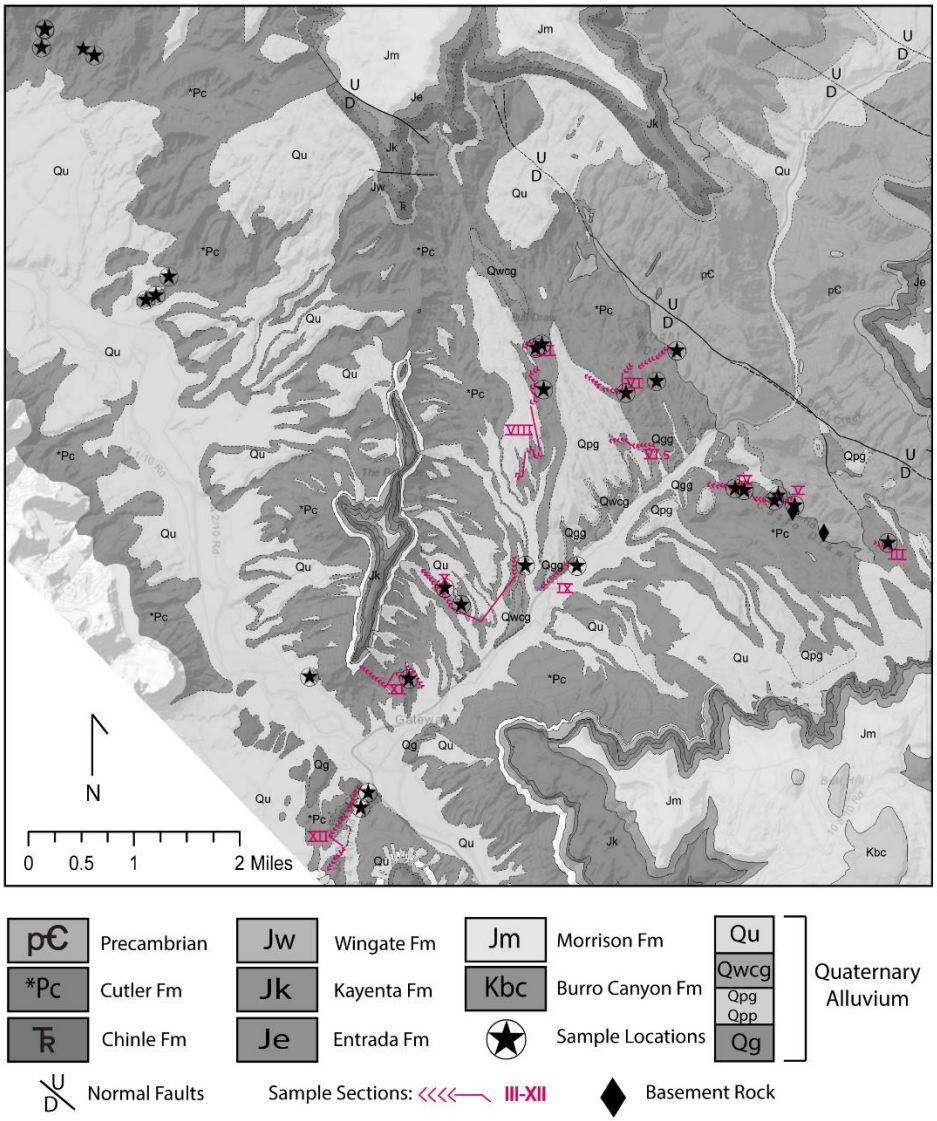

Fig. 3 (modified from Soreghan et al., 2009): Proximal Cutler sample location map in western Colorado, from the mouth of Unaweep Canyon to the Colorado-Utah boarder. RBG samples were collected from sections numbered as III (proximal) to XII ("distal" relative to the area, for easier reference).

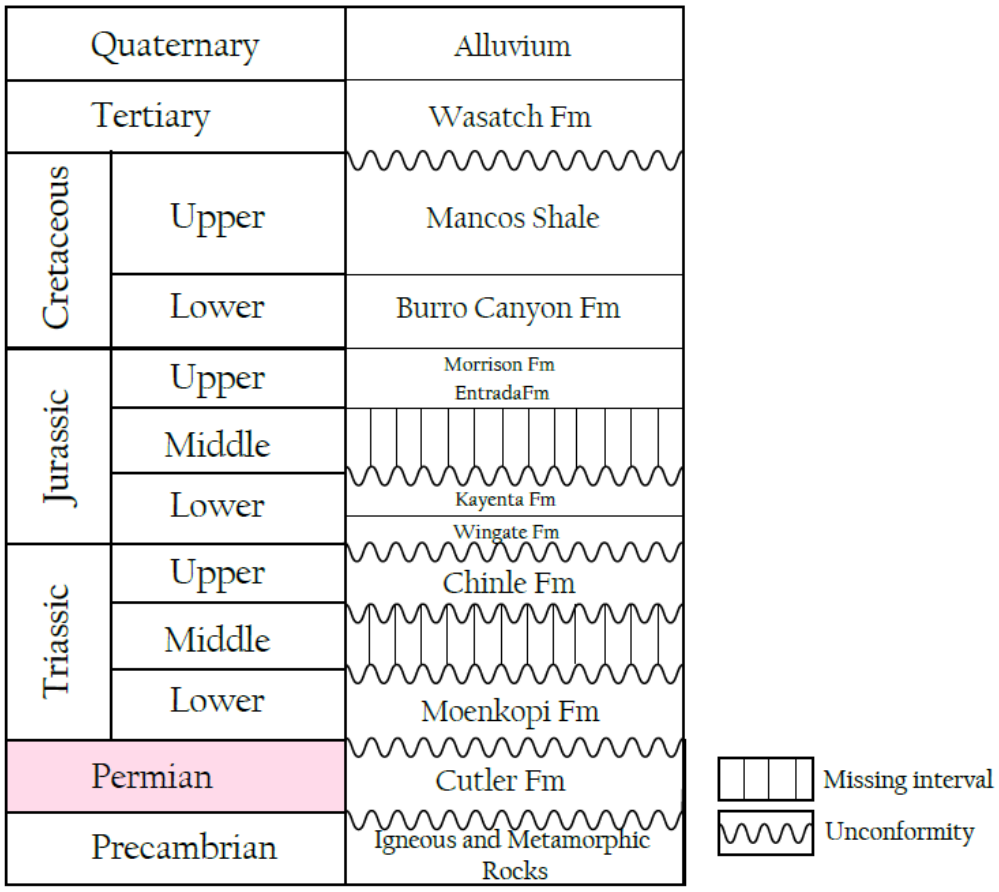

Fig. 4 (modified from Houston, Moreland, and Wray, 2009; Matheny and Longman, 1996; Nuccio and Condon, 1996): Generalized stratigraphic column of the Paradox Basin, including the Permian Cutler Formation highlighted in red.

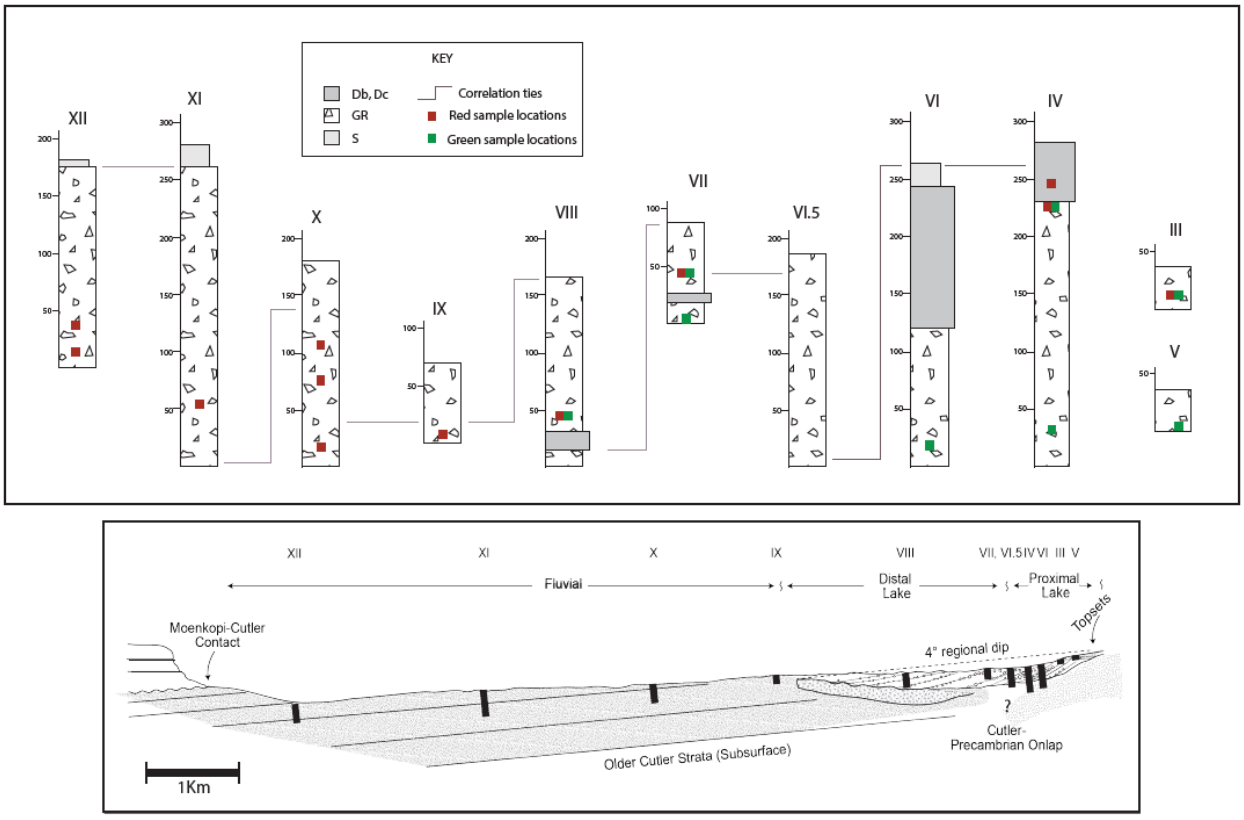

Fig. 5 (modified after Keiser et al., 2015): Vertical cross-section from proximal to distal Cutler where proximal starts at the mouth of Unaweep Canyon and distal is section XII, across from the Dolores River. Sample locations are denoted by their color as red or green. Bleached samples do not occur along these previously measured sections but were sampled from locations farther to the northwest closer to the Utah border.

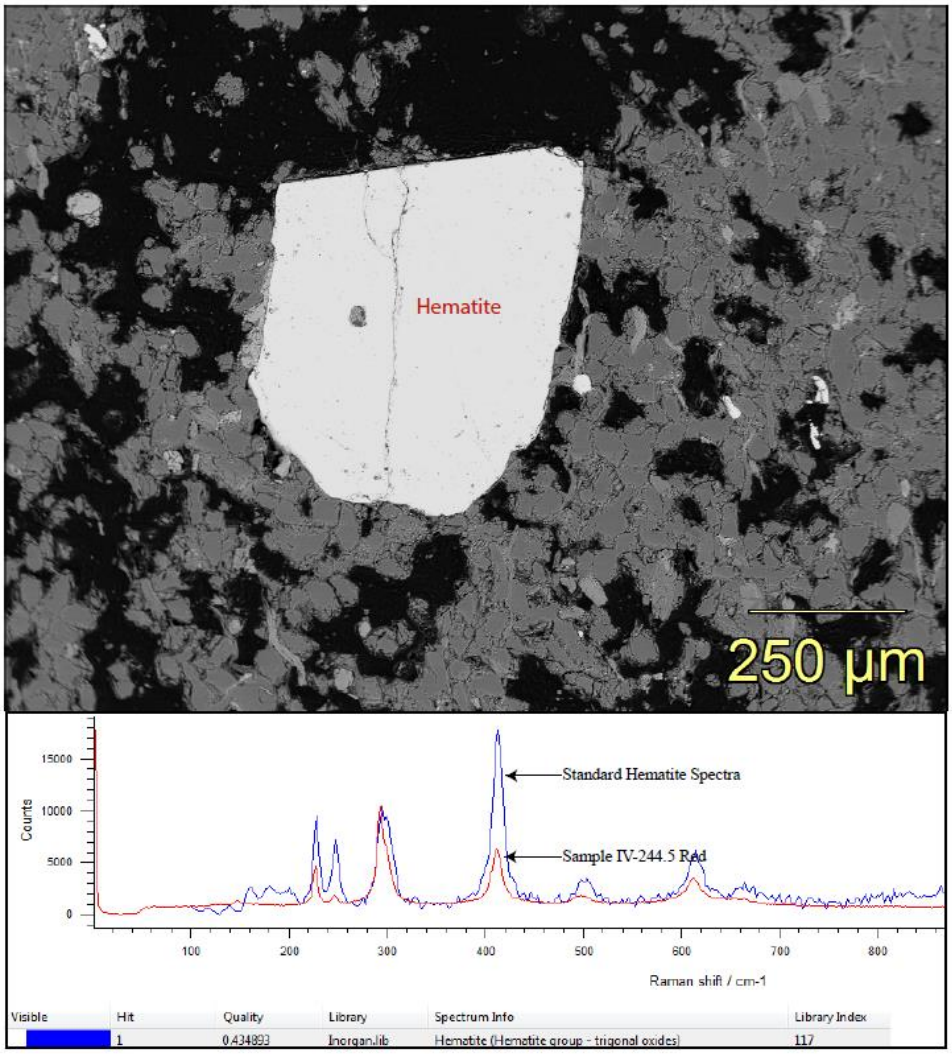

Fig. 6: EDS image of 500µm hematite grain (top) and Raman spectroscopy verifying Fe-oxide is hematite (bottom) from sample IV-244.5 Red.

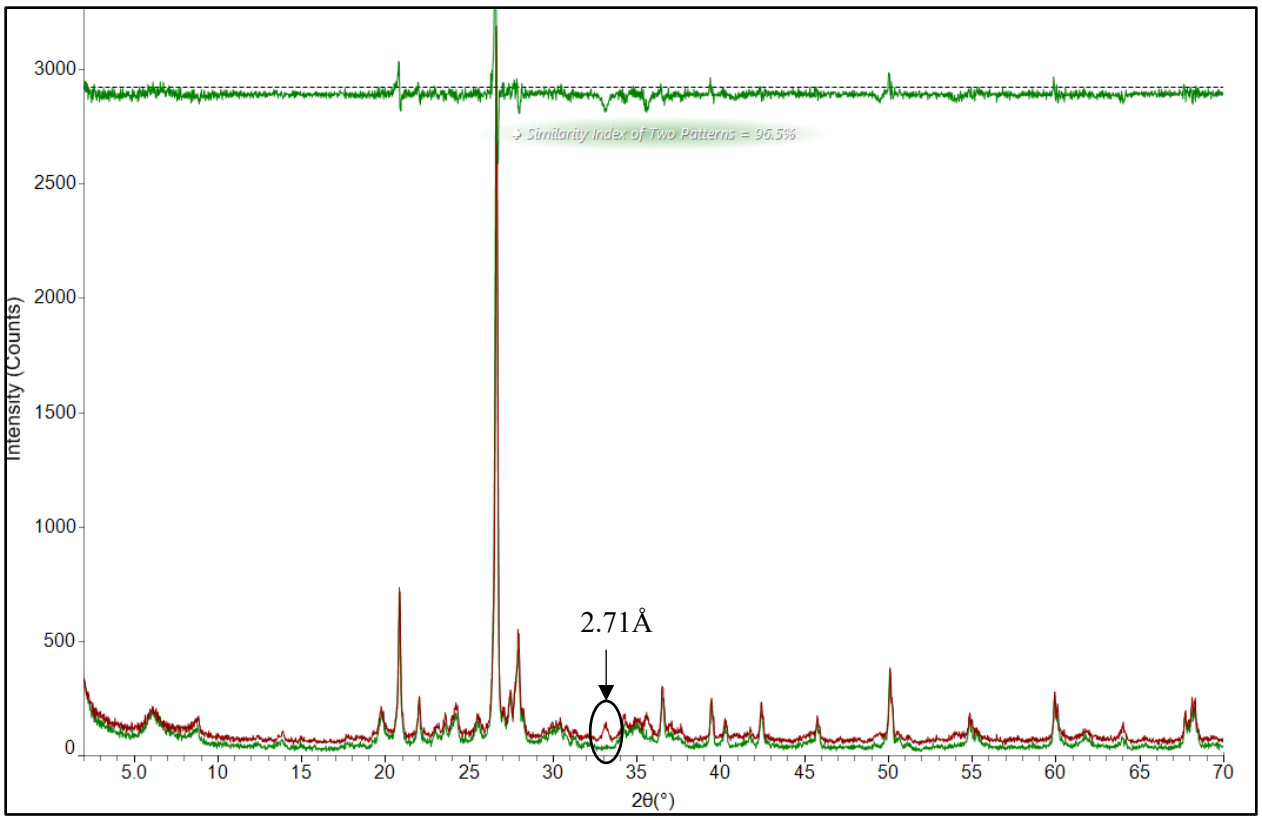

Fig. 7: Representative XRD subtraction pattern of sample 1218-15 RB with a calculated similarity between the red and bleached spectra of 96.5%. The main hematite peak at 2.71Å is visible in the red sample and circled in black.

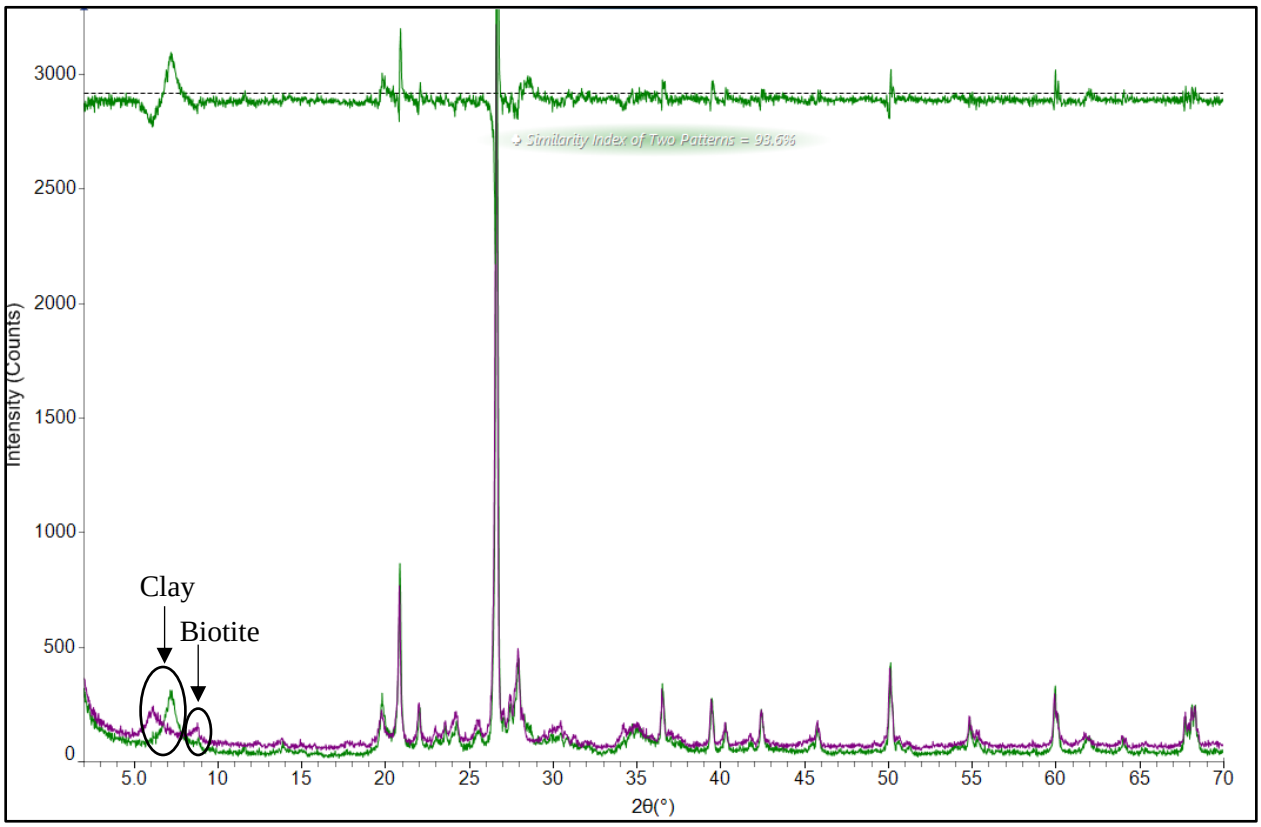

Fig. 8: Representative XRD subtraction pattern of sample 1218-15 Bleached (purple) and 1218-03 Green (green) displaying bulk mineralogical similarities of 93.6%. The main mineralogical differences are within the clay and biotite.

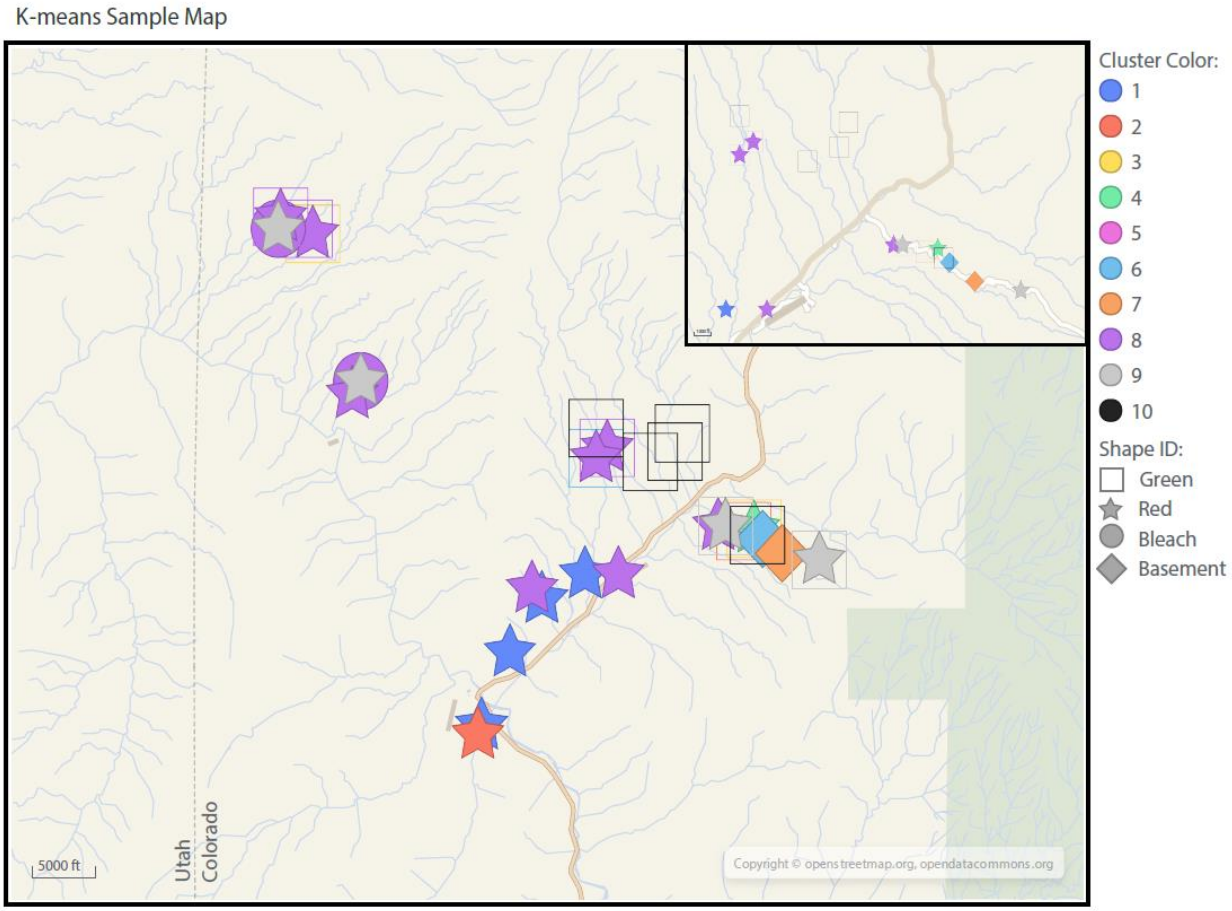

Fig. 9: K-means cluster analysis sample location map showing how sample colors (denoted by symbol) fall into ten different cluster groups and their spatial relationship.

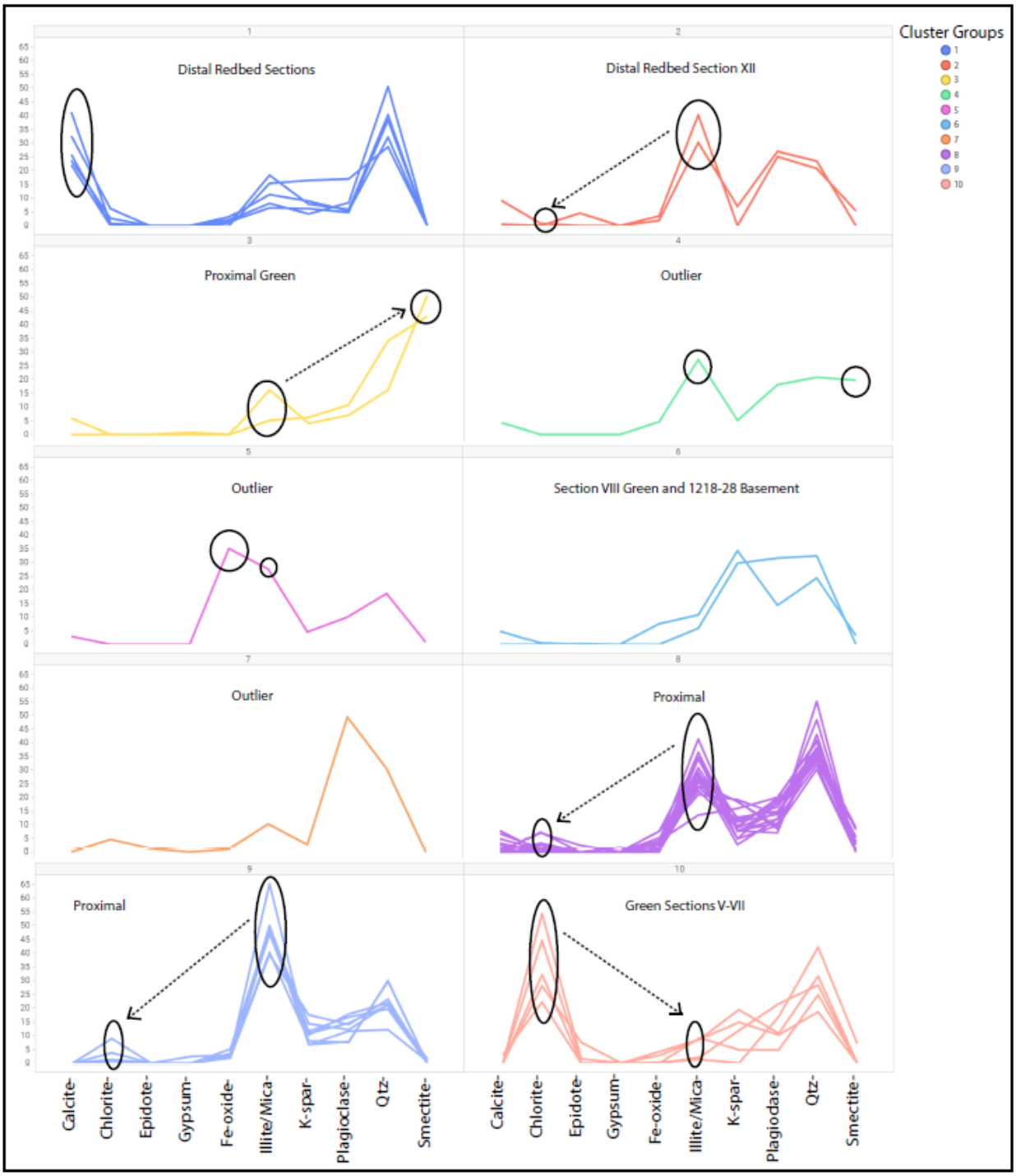

Fig. 10: XRD K-means clustering using 10 groups and 10 minerals to cluster 45 RGB bulk mineralogy samples. Key mineralogical differences are across samples are circled. Arrows represent mineral increase or decrease of circled minerals relative to each other.

Fig. 11: Box plots comparing the mineralogical abundance of five key minerals in the RGB + basement samples.

Fig. 12: Images of Massey core #1 sample MC-01-1078, containing green clay hosted within a gneissic basement rock fracture.

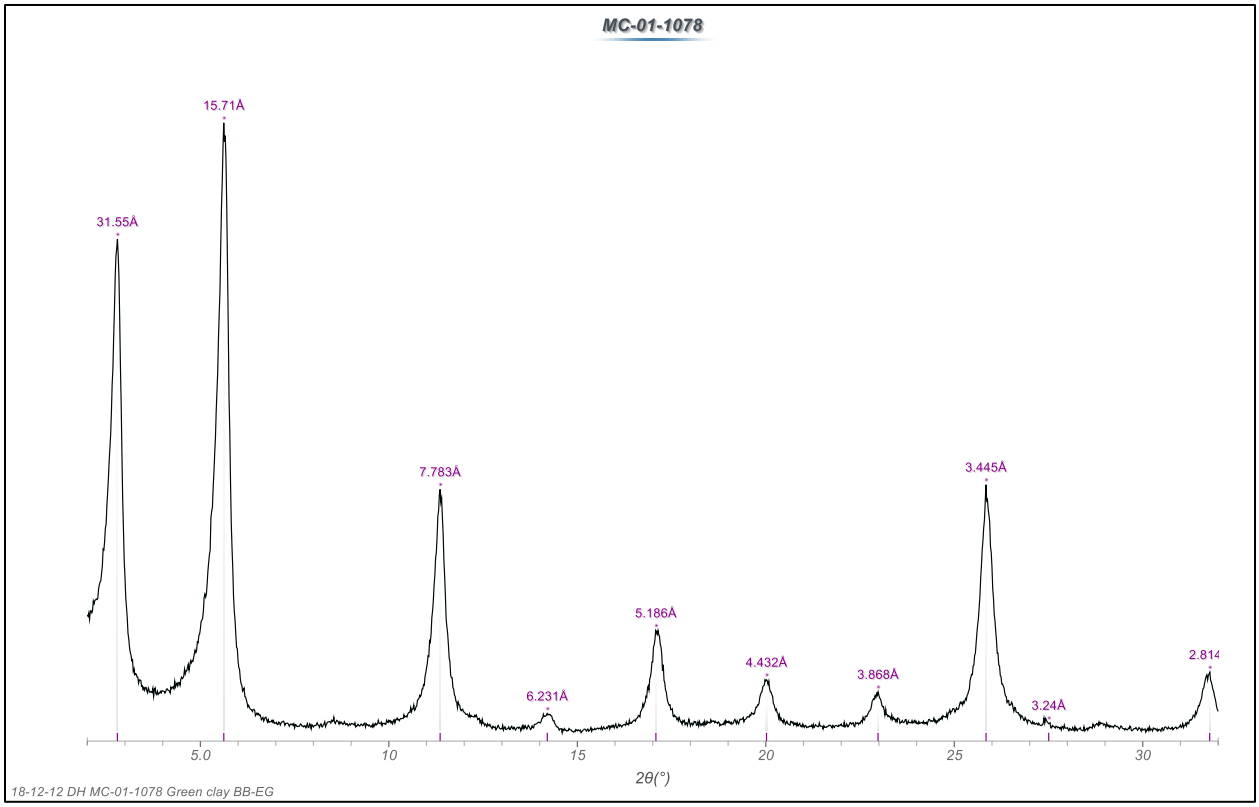

Fig. 13: XRD pattern of sample MC-01-1078 from Massey core #1 drilled in Unaweep Canyon showing pure corrensite. Oriented clay fraction extract after treatment with ethylene glycol vapor.

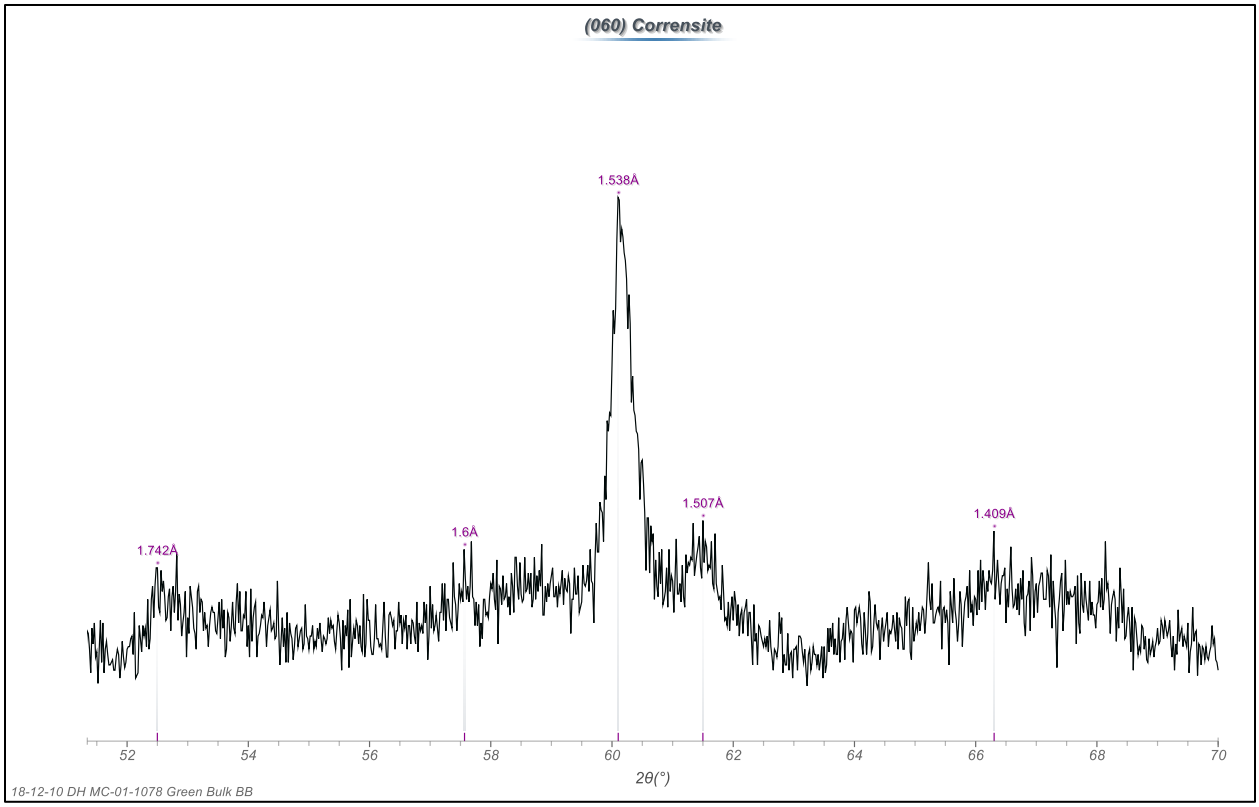

Fig. 14: XRD spectra of (060) corrensite peaks in the random mount clay fraction of sample MC-01-1078. The 1.538Å peak represents a tri-octahedral layer and the 1.507Å peak represents a di-octahedral layer suggesting a tri-di corrensite.

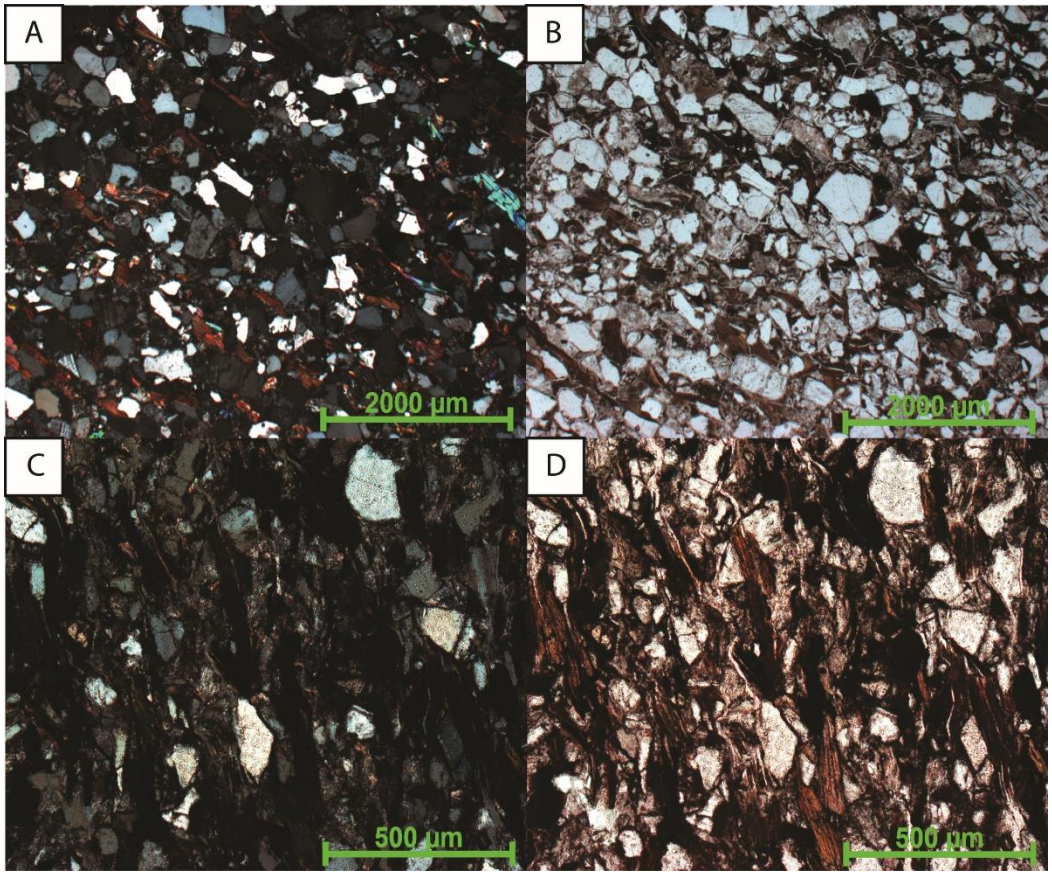

Fig. 15: Optical petrography showing compaction via parallel biotite grains in red-bleached and red-green samples 1218-15 RB (top) and 53 III-14A (bottom).

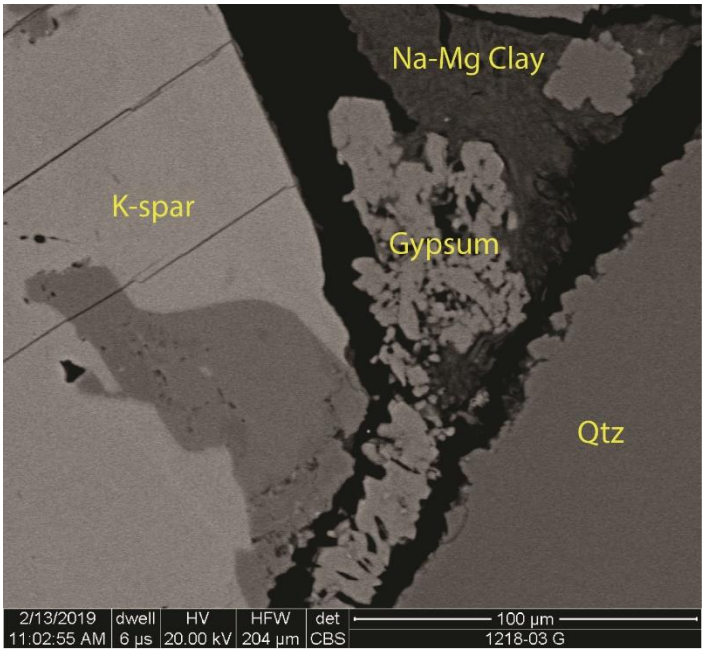

Fig. 16: SEM image of gypsum cement in sample 1218-03 green related to recent oxidative groundwater exposure after the Cutler Formation was eroded and uplifted.

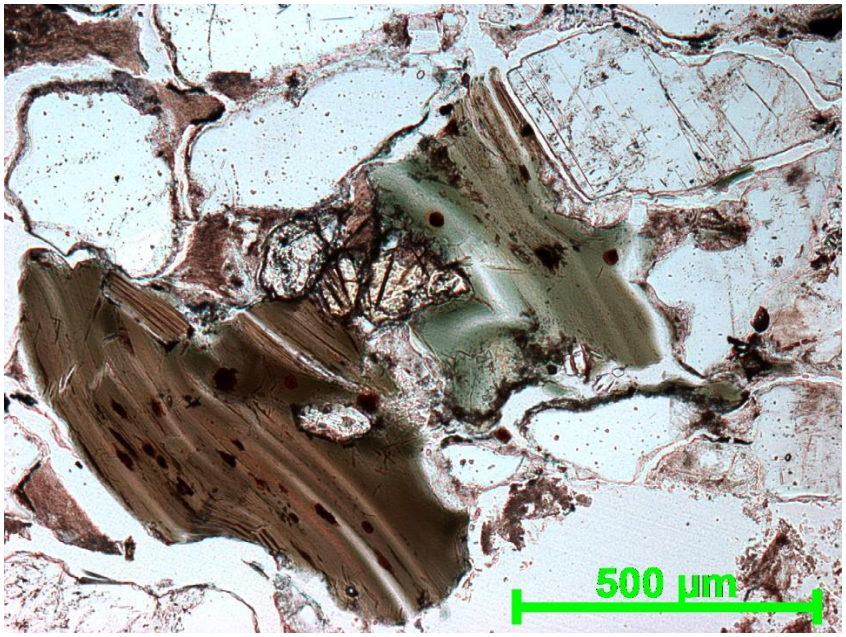

Fig. 17: Biotite brown-green pleochroism in plane light signifying higher than normal iron content.

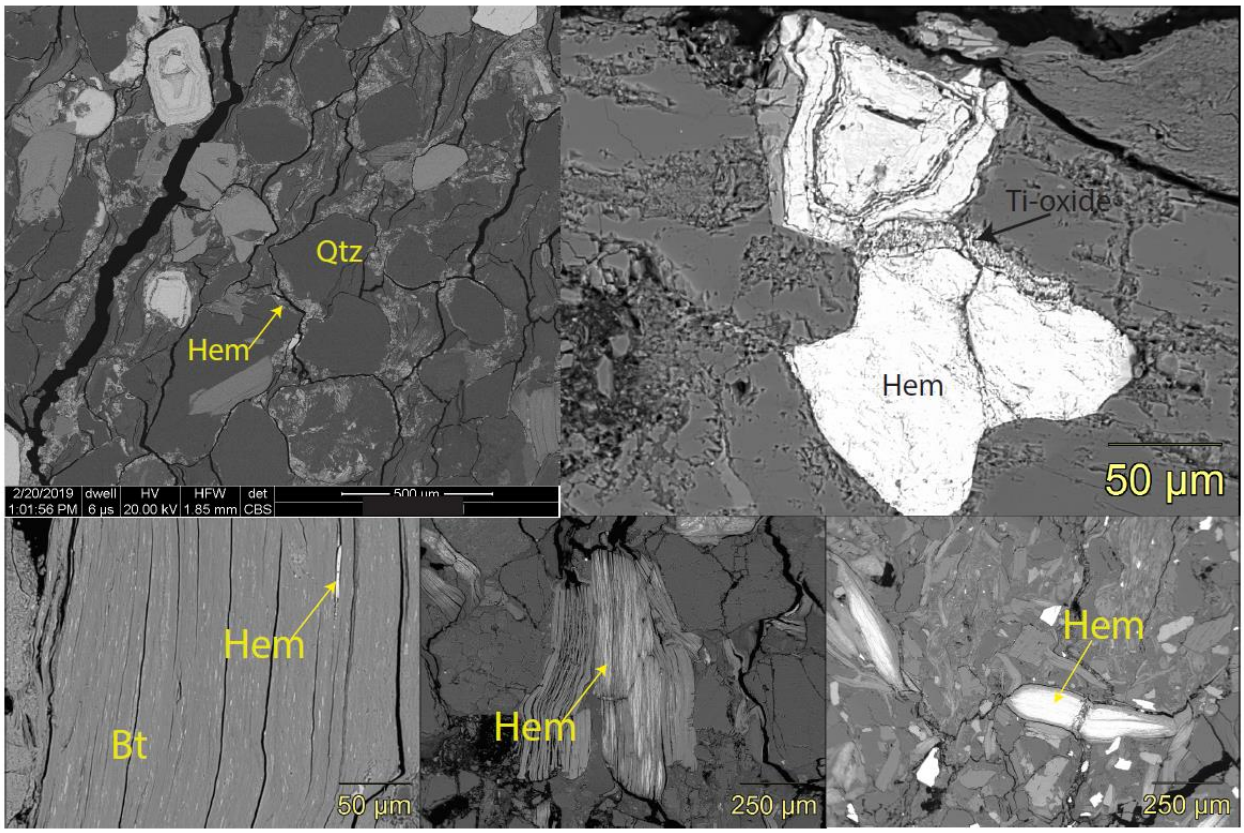

Fig. 18: Varying iron-oxide (hematite) occurrences throughout the Cutler Fm as: coarse grains (top-right), rims (top-left), and biotite replacements/intergrowths (bottom) from minor to almost total replacement.

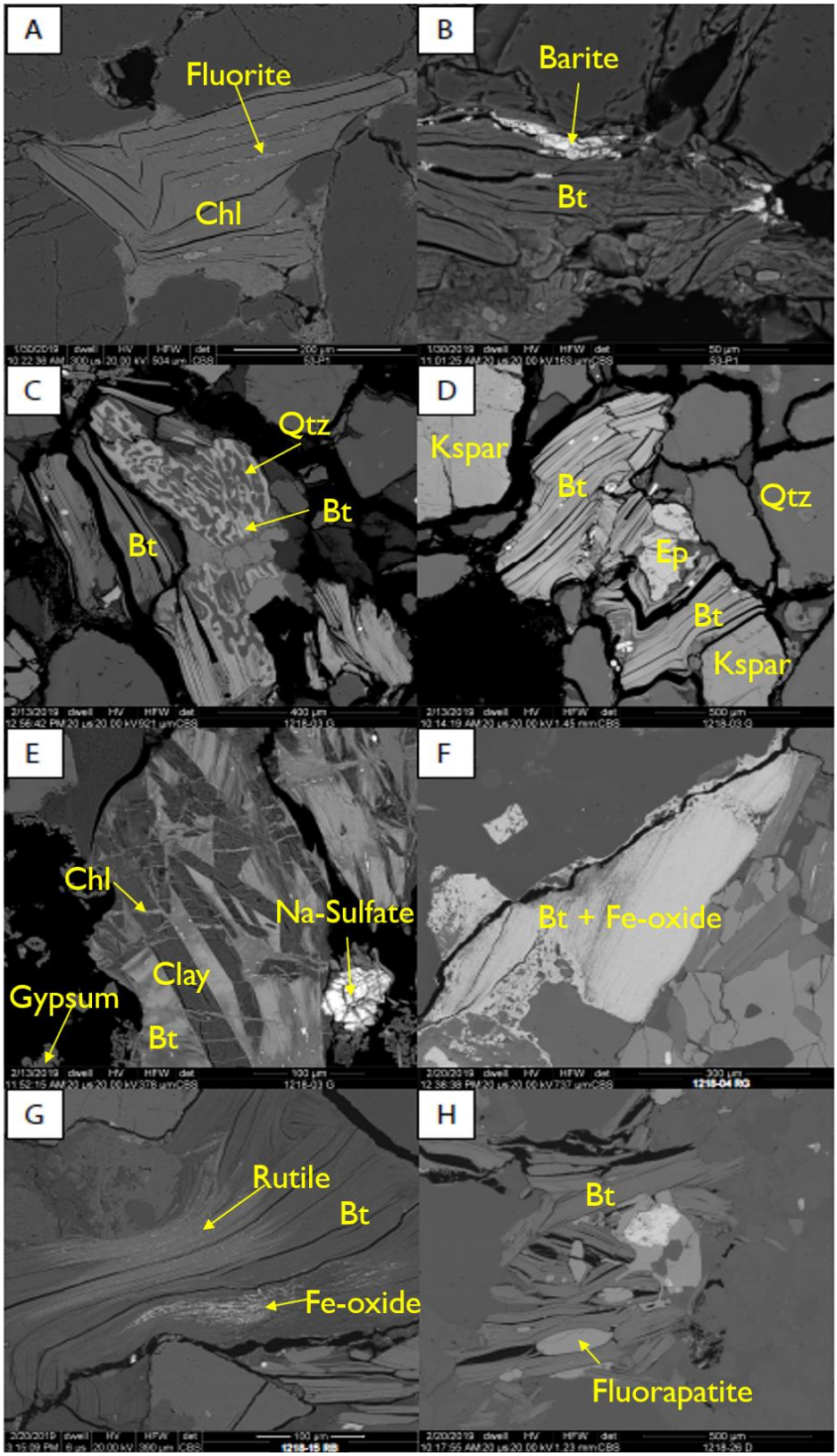
A
Fluorite
Chl
B
Barite
Bt
C
Qtz
Bt
Bt
D
Kspar
Bt
Qtz
Ep
Bt
Kspar
E
Chl
Na-Sulfate
Clay
Gypsum
Bt
F
Bt + Fe-oxide
G
Rutile
Bt
Fe-oxide
H
Bt
Fluorapatite

Fig. 19: SEM of secondary mineral intergrowths in biotite and chloritized biotite. A) Chlorite + Fluorite B) Bt + Barite C) Bt + Qtz D) Bt associations, Bt + Ep +Apatite + Qtz + Kspar E) Bt + Chlorite + Clay F) Bt replaced by Fe-oxide G) Bt +Rutile and Fe-oxide intergrowths H) Bt + Fluorite and Fluorapatite.

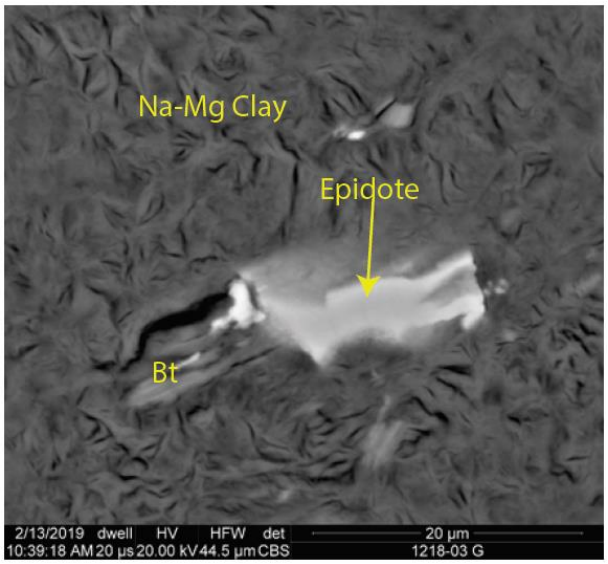

Fig. 20: Authigenic epidote in association with biotite dissemination, surrounded by Na-Mg clay, interpreted as montmorillonite, in green sample 1218-03 G.

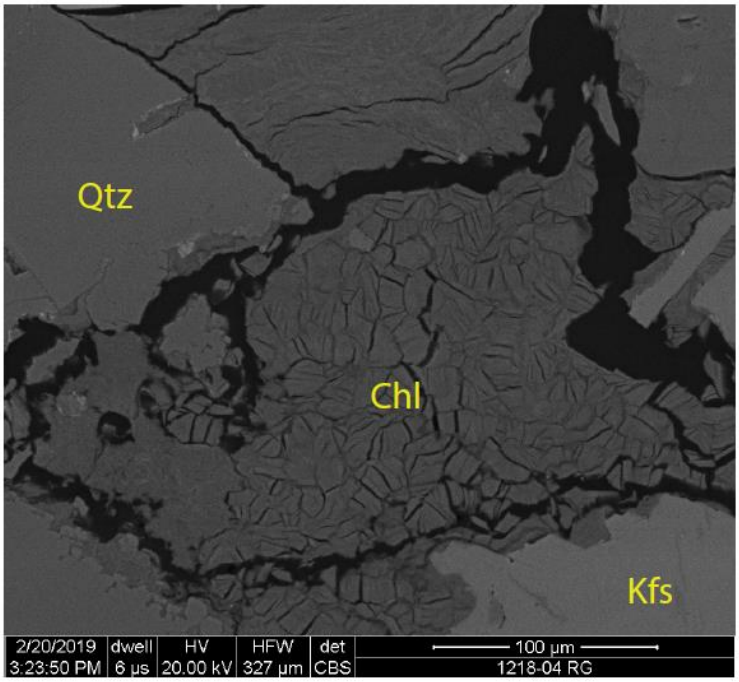

Fig. 21: Chlorite in sample 1218-15 RB as pore-filling.

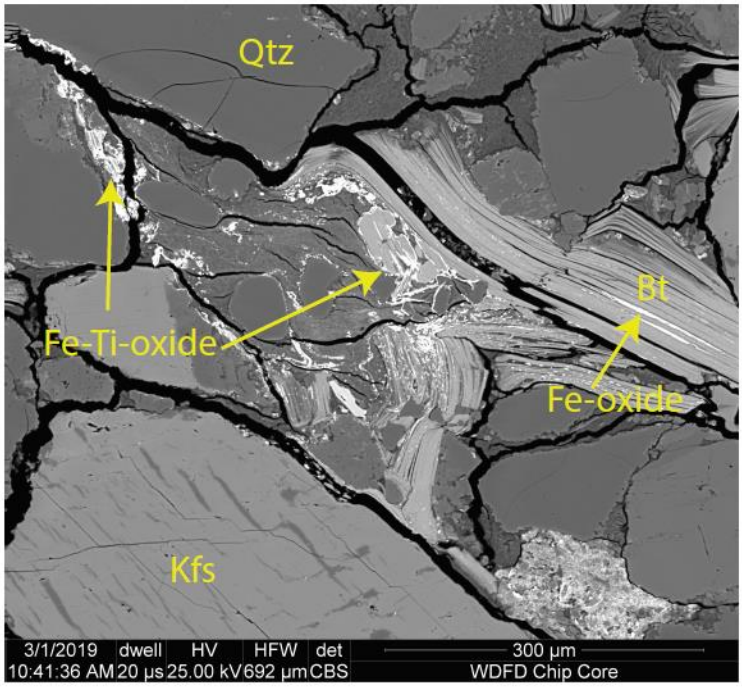

Fig. 22: SEM image of Fe-Ti-oxide rims in the bleached portion of sample 1218-15 RB, supporting hydrothermal fluid alteration.

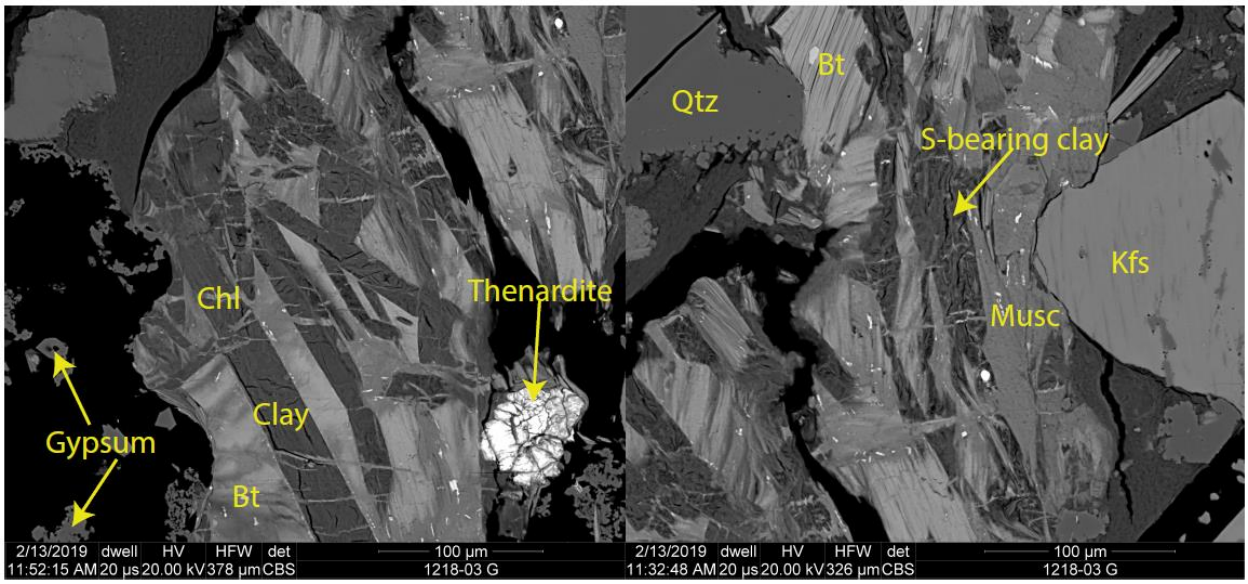

Fig. 23: SEM of gypsum, sulfur-rich clay, and thenardite in sample 1218-03 Green which signifies weathering of the sample.

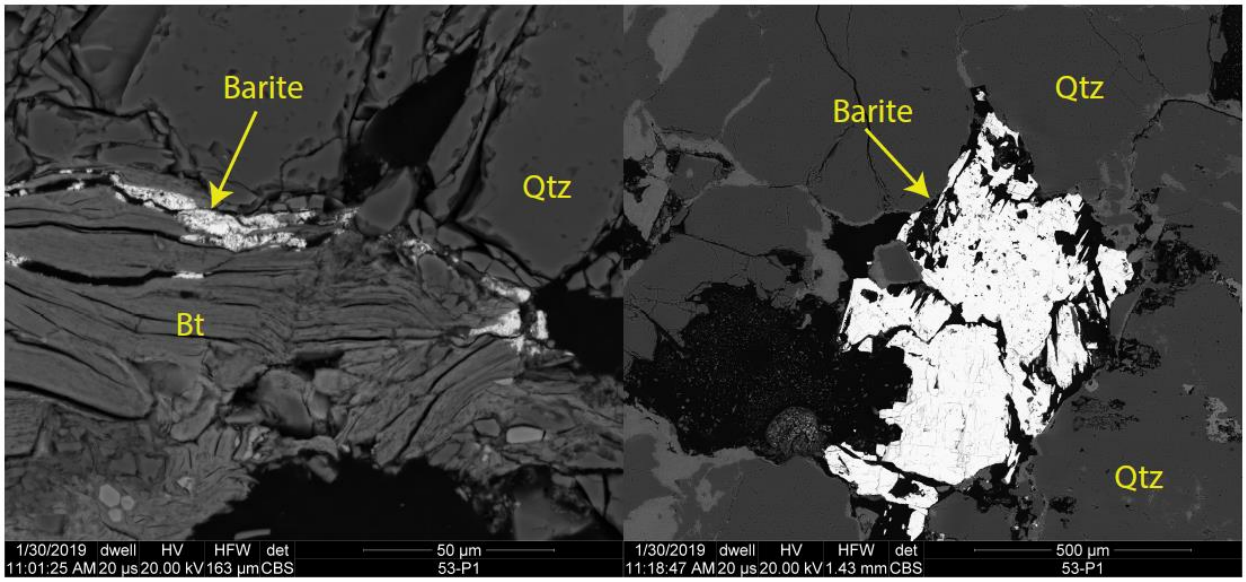

Fig. 24: SEM images of barite intergrowths within biotite as well as large barite grains in sample 53S V-1 Green.

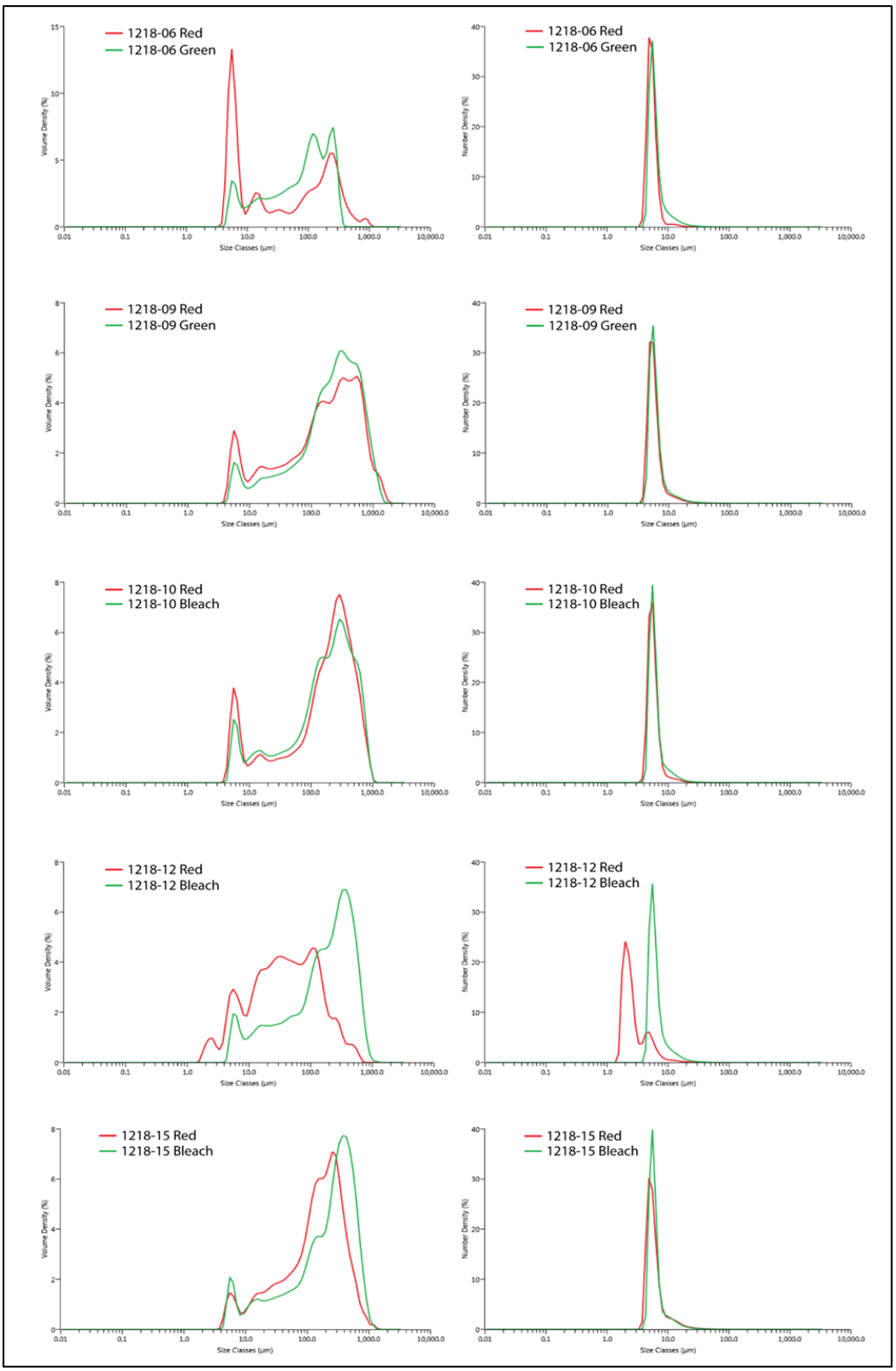
1218-06 Red
1218-06 Green
Volume Density (%)
Number Density (%)
Size Classes (µm)
1218-09 Red
1218-09 Green
1218-10 Red
1218-10 Bleach
1218-12 Red
1218-12 Bleach
1218-15 Red
1218-15 Bleach

Fig. 25: Grain-size graphs of LPSA data comparing RGB differences where the x-axis is grain size (μm) and the y-axis is volume %. Graphs on the left denote volume and graphs on the right are particle size.

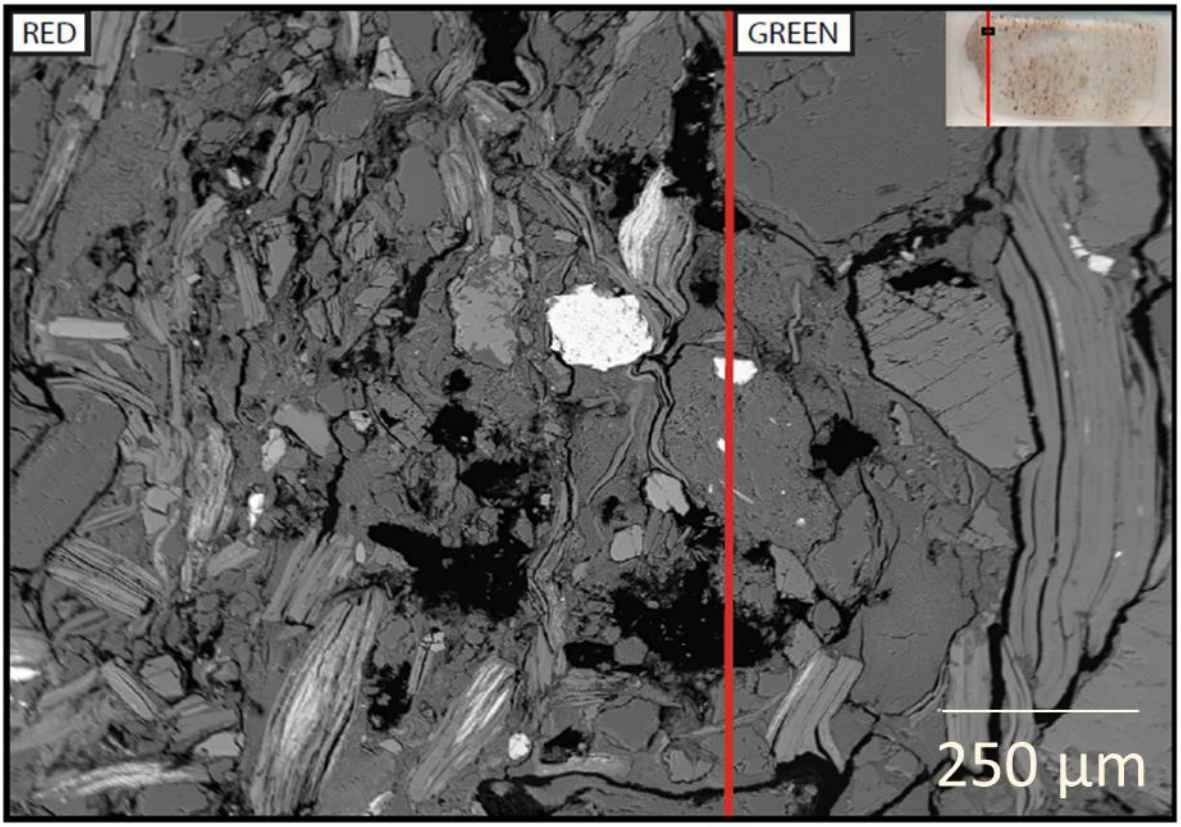

Fig. 26: EDS element map of sample 53 III-14A showing grain-size variations between the red and green rocks across their redox interface.

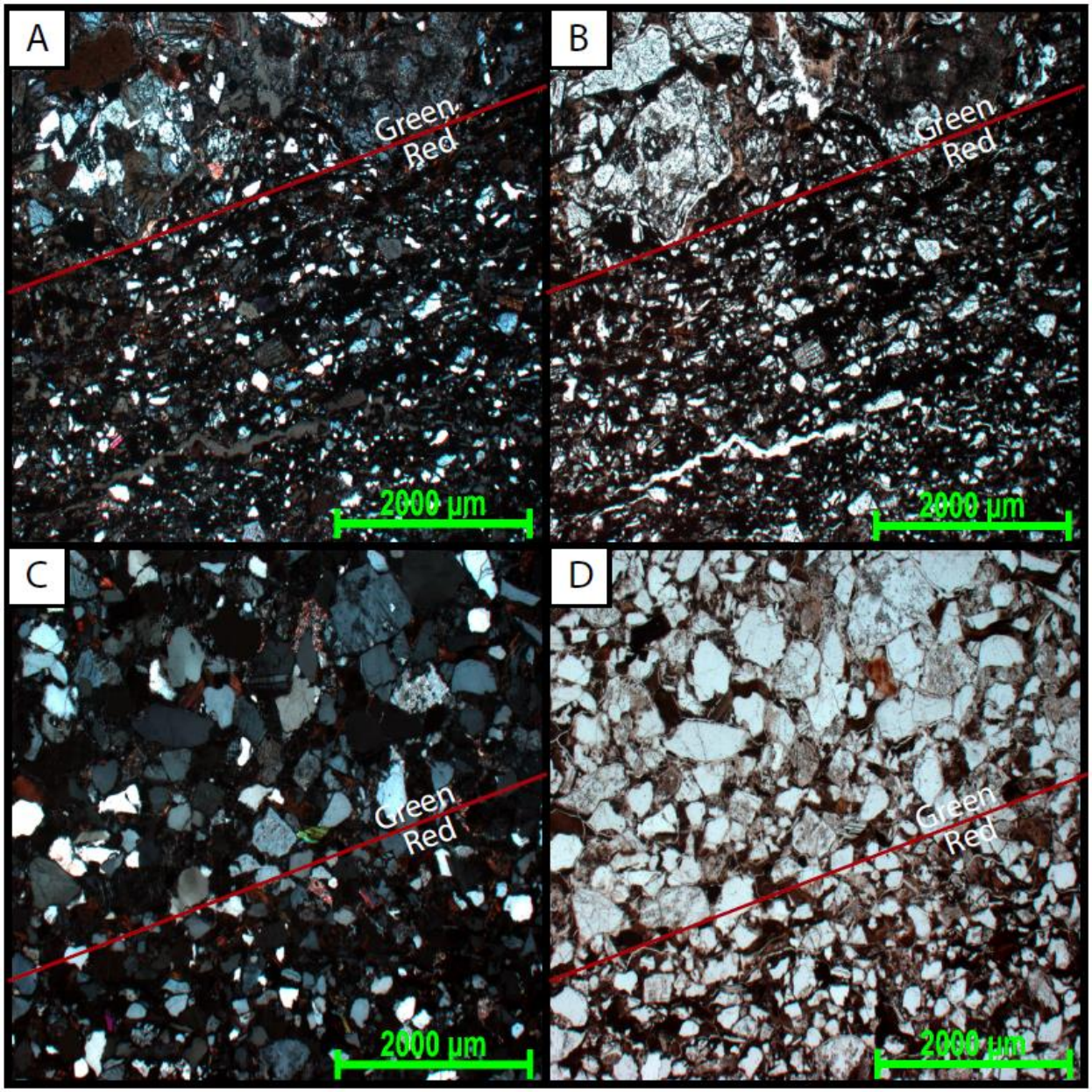

Fig. 27: Optical microscopy illustrating grain-size variation between the red and green rocks.

The red rocks are finer grained than the coarser grained green.

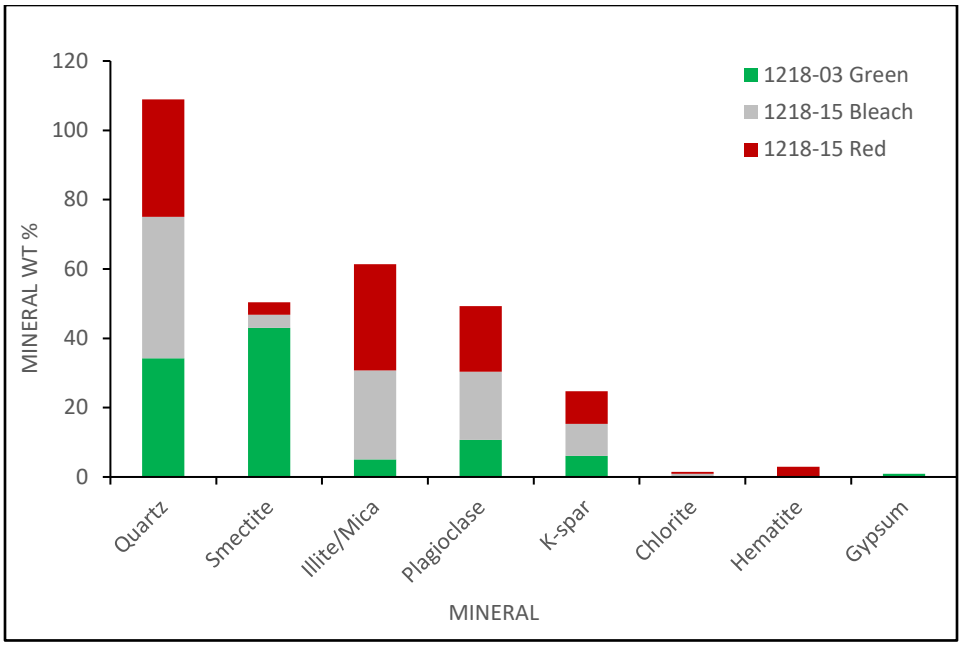

Fig. 28: RGB bulk mineralogy chart of three representative red, green, and bleached samples.

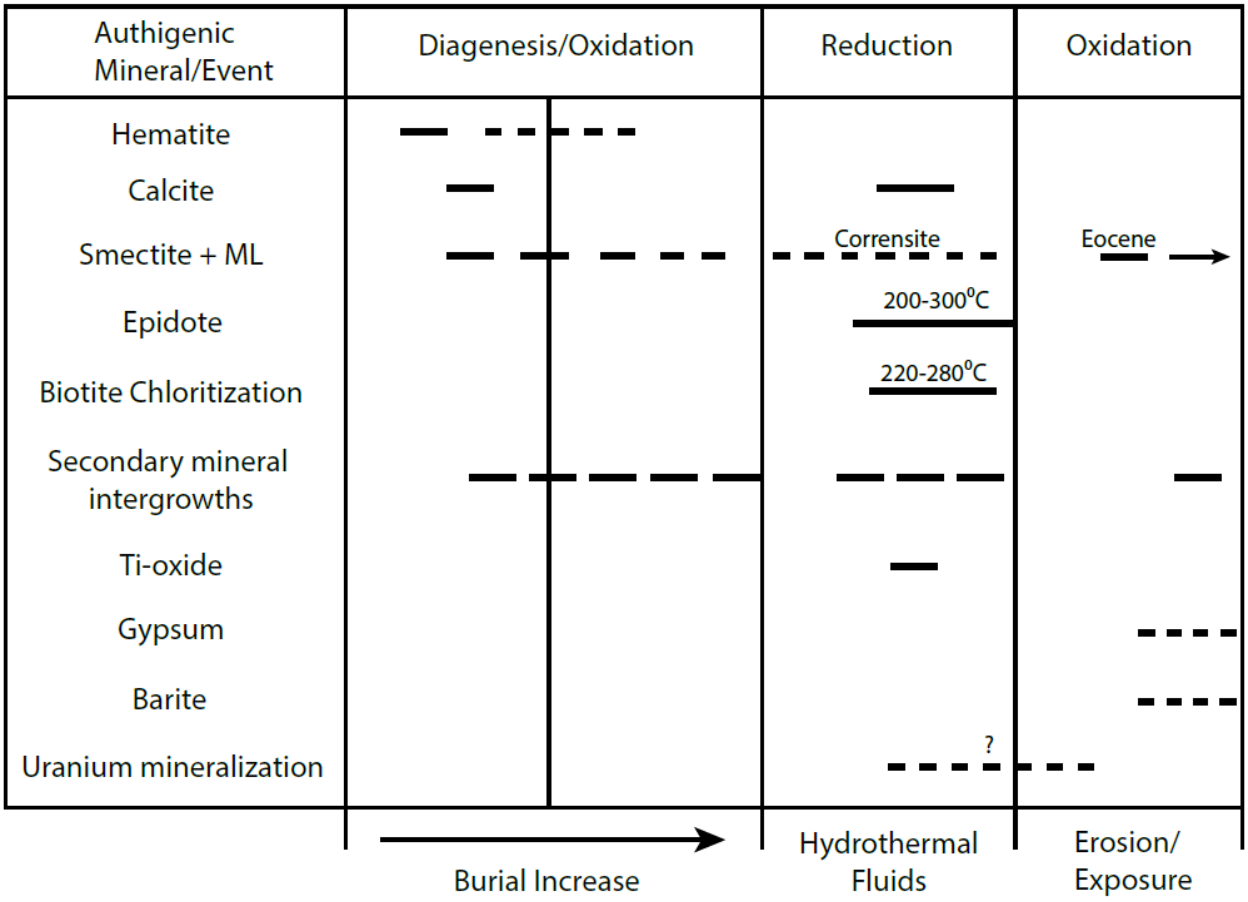

Fig. 29: Paragenetic sequence of events in the Cutler from the time of deposition to recent.

Smectite represents pure smectite + mixed layer illite-smectite and chlorite-smectite.

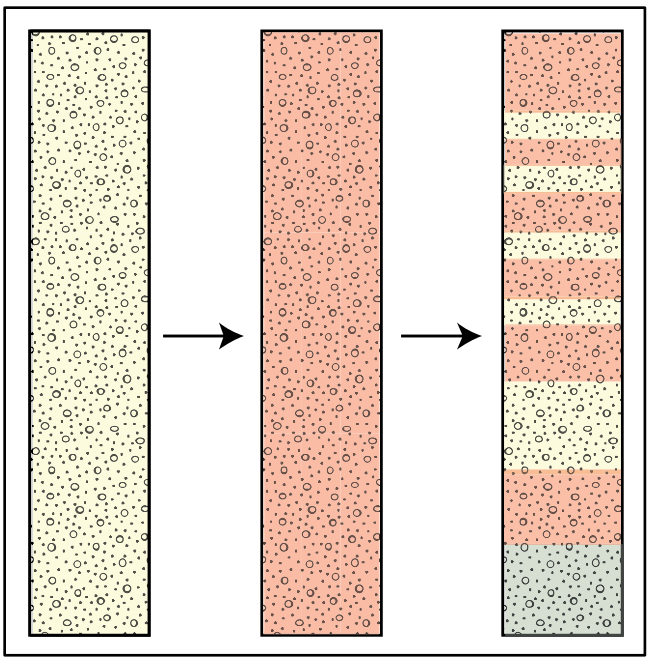

Fig. 30: Generalized schematic of proposed Permian red bed color transformations through geologic time where the formation was (1) deposited without any distinct color, (2) turned red from hematite formation during diagenesis, and then (3) Fe-oxide reduction or stripping from hydrothermal fluid influx. Iron stripping would have occurred via Fe(III) reduction to Fe(II) since Fe(II) is more soluble. The solubilized Fe(II) would then be transported some distance or deposited in the adjacent red layers. Alternatively, syn-depositional weathering to form pigmentary hematite would lead to red-beds during burial, according to the center column; however, evidence also suggests hematite authigenesis during burial diagenesis.

TABLES

Table 1: Munsell color of Cutler Formation rocks.

Sample ID	Sample Color	Munsell Color
53 III-14A:	Red	5R4/2: Grayish Red
	Green	5GY8/1: Light Greenish Gray
53 III-14C:	Red	5R4/2: Grayish Red
	Green	10G8/2: Very Pale Green
53 IV-30:	Green	5GY8/1: Light Greenish Gray
53 IV-230:	Red	5R4/2: Grayish Red
	Green	5YR6/1: Light Brownish Gray
IV-244.5:	Red	10R4/6: Moderate Reddish Brown
53S V-1:	Green	5Y3/2: Olive Gray
63S VI-27:	Green	10GY5/2: Grayish Green
63S VII-1:	Green	5GY5/2: Dusky Yellow Green
63S VII-45:	Red	5R5/4: Moderate Red
	Green	5GY8/1: Light Greenish Gray
63S VIII-47:	Red	5R3/4: Dusky Red
	Green	5GY8/1: Light Greenish Gray
63S IX-6:	Red	10R5/4: Pale Reddish Brown
63S X-19.2:	Red	10R4/6: Moderate Reddish Brown
63S X-75.5:	Red	10R4/6: Moderate Reddish Brown
63 X-106.5:	Red	5R4/2: Grayish Red
63S XI-54.5:	Red	10R5/4: Pale Reddish Brown
63S XII-16.5:	Red	10R4/6: Moderate Reddish Brown
63S XII- 37.5:	Red	5R4/6: Moderate Red
MC-01-1078:	Green	5GY6/1: Greenish Gray
1218-01 Gmt Sediment:	Green	5Y6/1: Light Olive Gray
1218-02 Gmt Outcrop:	Green	5G6/1: Greenish Gray
1218-03 Gmt Outcrop:	Green	5GY8/1: Light Greenish Gray
1218-04 and 1218-06 Gmt:	Red	5RP4/2: Grayish Red Purple
	Green	5GY8/1: Light Greenish Gray

Sample ID	Sample Color	Munsell Color
1218-05 Gmt Outcrop:	Red	5RP2/2: Very Dusky Purple
1218-07 Fluvial Cutout:	Red	10R3/4: Dark Reddish Brown
	Green	5GY8/1: Light Greenish Gray
1218-08 Fluvial Cutout:	Red	10R3/4: Dark Reddish Brown
1218-09 Column:	Red	10R4/2: Grayish Red
	Green	5B9/1: Bluish White
1218-10 Area 1 Outcrop:	Red	5RP4/2: Grayish Red Purple
	Bleach	N8: Very Light Gray
1218-12 Area 1 Outcrop:	Red	10R4/6: Moderate Reddish Brown
	Bleach	5G8/1: Light Greenish Gray
1218-14 Area 1 Outcrop:	Red	5R3/4: Dusky Red
1218-15 Area 1 Outcrop:	Red	5RP4/2: Grayish Red Purple
	Bleach	N8: Very Light Gray
1218-24 Area 2 Outcrop:	Red	10R3/4: Dark Reddish Brown
1218-30 IV 6.3 Casto Draw:	Red	5R4/2 Grayish Red
	Green	10GY7/2: Pale Yellowish Green
1218-31 VI Wright Draw:	Green	10Y5/4: Grayish Olive

Table 2: XRD bulk mineralogy of 10 key minerals and their associated wt.% plus the location of each sample represented as latitude and longitude. Samples are color coded by their k-means cluster group from Fig. 10.

Sample ID	% Calcite	% Chlorite	% Epidote	% Gypsum	% Fe-oxide	% Illite/Mica	% K-spar	% Plagioclase	% Qtz	% Smectite	Latitude	Longitude	K-means Clustering
635 X -19.2 Red	41.50	0.70	0.00	0.00	1.50	6.60	6.30	4.90	38.50	0.00	38.71	-108.95	1
635 X -75.5 Red	25.90	0.40	0.00	0.00	1.20	18.30	7.80	6.00	40.40	0.00	38.70	-108.96	1
635 X-54.5 Red	32.67	6.19	0.00	0.00	3.20	11.39	8.89	5.39	32.27	0.00	38.69	-108.97	1
635 XII-16.5 Red	23.92	2.80	0.00	0.00	2.20	8.01	4.20	8.41	50.45	0.00	38.67	-108.98	1
1218-04 Gr een	22.15	0.10	0.00	0.00	0.10	15.53	16.46	17.08	28.57	0.00	38.77	-109.03	1
53 IV -30 Gravel	0.50	0.00	4.50	0.00	3.40	40.30	0.00	25.10	20.70	5.50	38.71	-108.91	2
63 XII-37.5 Red	9.30	0.90	0.00	0.00	2.00	30.20	6.90	27.10	23.60	0.00	38.67	-108.98	2
1218-30 Gr een	5.88	0.00	0.00	0.00	0.00	16.28	4.10	6.98	16.28	50.48	38.71	-108.90	3
1218-03 Gr een	0.00	0.00	0.00	0.90	0.00	5.10	6.10	10.70	34.20	43.00	38.77	-109.03	3
1218-30 Red	4.40	0.00	0.00	0.00	4.50	27.40	5.10	18.00	20.80	19.80	38.71	-108.90	4
1218-30 Black	2.90	0.00	0.00	0.00	35.16	27.67	4.70	10.09	18.68	0.80	38.71	-108.90	5
1218-28 WMQM	0.00	0.00	0.32	0.00	0.00	5.89	29.79	31.68	32.32	0.00	38.71	-108.90	6
635 VIII-47 Gr een	4.80	0.50	0.00	0.00	7.51	10.81	34.43	14.31	24.42	3.20	38.73	-108.95	6
1218-26D	0.00	4.60	1.30	0.00	1.20	10.20	2.60	49.60	30.50	0.00	38.71	-108.90	7
53 IV -244.5 Red	0.00	0.00	0.00	0.00	1.20	29.07	4.80	9.69	55.24	0.00	38.72	-108.91	8
635 VII-45 Gr een	2.70	0.60	0.00	0.00	4.10	21.22	19.32	13.91	35.34	2.80	38.73	-108.95	8
635 VII-45 Red	6.69	1.40	0.00	0.00	3.80	24.08	18.58	8.39	37.06	0.00	38.73	-108.95	8
635 VIII-47 Red	7.80	0.50	0.00	0.00	7.70	25.60	18.50	9.50	30.40	0.00	38.73	-108.95	8
635 I X-6 Red	4.95	0.91	0.00	0.00	4.14	13.54	16.06	20.10	40.30	0.00	38.71	-108.94	8
63 X -106.5 Red	0.00	0.00	0.00	0.00	3.60	33.97	7.69	14.99	34.27	5.49	38.70	-108.97	8
1218-24 Red	0.00	6.91	2.50	0.00	2.50	36.44	7.61	12.21	31.83	0.00	38.74	-109.02	8
1218-15 Bleach	0.00	0.90	0.00	0.00	0.00	25.60	9.20	19.70	40.80	3.80	38.74	-109.01	8
1218-15 Red	0.00	0.60	0.00	0.00	2.90	30.70	9.40	18.90	33.90	3.60	38.74	-109.01	8
1218-12 Bleach	0.00	0.31	0.00	0.00	0.00	34.20	12.02	16.37	37.10	0.00	38.74	-109.01	8
1218-10 Bleach	2.80	0.00	0.00	0.00	0.30	23.90	11.00	17.60	36.20	8.20	38.74	-109.01	8
1218-10 Red	1.10	2.40	0.00	0.00	5.10	22.40	8.90	14.70	36.40	9.00	38.74	-109.01	8
1218-09 Gr een	2.40	0.00	0.00	0.00	2.60	28.57	12.79	14.89	33.37	5.39	38.78	-109.04	8
1218-09 Red	3.20	0.00	0.00	0.00	3.90	26.80	11.10	13.90	37.20	3.90	38.78	-109.04	8
1218-08 Red	0.00	0.10	0.00	0.00	3.99	41.28	7.78	10.47	35.79	0.60	38.78	-109.04	8
1218-07 Bleach	0.00	7.30	0.00	1.50	0.00	27.80	2.70	12.20	48.50	0.00	38.78	-109.04	8
1218-04 Red	0.00	0.00	0.00	0.00	7.49	34.73	7.83	7.04	42.91	0.00	38.77	-109.03	8
1218-01 Gr een	0.00	3.30	0.00	0.00	0.90	34.50	5.00	18.10	38.20	0.00	38.78	-109.03	8
53 III-14A Gr een	0.00	0.00	0.00	0.00	1.80	50.05	10.79	14.69	20.98	1.70	38.71	-108.89	9
53 III-14A Red	0.00	0.00	0.00	0.00	3.09	65.17	6.89	11.68	12.28	0.90	38.71	-108.89	9
53 III-14C Gr een	0.00	0.00	0.00	0.00	1.80	46.95	10.41	17.92	21.92	1.00	38.71	-108.89	9
53 III-14C Red	0.00	0.00	0.00	0.00	3.60	48.55	14.29	12.29	21.28	0.00	38.71	-108.89	9
53 IV -230 Cutler ...	0.00	1.40	0.00	0.00	2.10	48.40	11.60	16.80	19.70	0.00	38.72	-108.91	9
53 IV -230 Cutler ...	0.00	3.80	0.00	0.00	1.90	39.46	17.48	14.19	23.18	0.00	38.72	-108.91	9
1218-12 Red	0.00	1.20	0.00	0.00	5.11	49.35	6.71	7.81	29.83	0.00	38.74	-109.01	9
1218-07 Red	0.00	8.80	0.00	2.40	3.00	40.30	8.10	7.50	29.90	0.00	38.78	-109.04	9
535 V -1_53-Pl ...	0.00	32.18	0.00	0.00	0.20	1.43	0.00	16.90	42.16	7.13	38.71	-108.90	10
635 VI-27 Gr een	0.00	54.38	1.56	0.00	0.31	9.06	5.00	4.90	24.79	0.00	38.73	-108.92	10
635 VI-167.8	0.00	44.54	0.00	0.00	3.06	8.62	14.96	10.26	18.56	0.00	38.73	-108.93	10
1218-31 Gr een	0.11	28.14	7.57	0.00	0.11	2.15	11.86	21.58	28.47	0.00	38.73	-108.93	10
635 VII-1 Gr een	2.90	22.12	0.00	0.00	4.40	8.61	19.42	10.81	31.73	0.00	38.74	-108.95	10

Table 3: Summary of clay fraction mineral occurrence and semiquantitative abundance where X indicates relative clay mineral abundance.

Sample ID	Corrensite	Smectite	Chlorite	Illite-Smectite	Illite	Chlorite-smectite
MC-01-1078	XXX					
1218-26D			XX		XX	X
53 III-14A Green		XX				
53 III-14A Red			XX	XX	X	
53 III-14C Green	XX			XX	X	
53 III-14C Red			X	XX		
53 IV-30 Gravel Green		XXX				
1218-30 Green		X		XX	XX	
1218-30 Red		XXX	X			
53 IV-230 Cutler Green			XX	XX	XX	
53 IV-230 Cutler Red		XX	X	XXX	XX	
53 IV-244.5 Red	XX		X		XX	
53S V-1_53-P1 Green		X			XX	XX
63S VI-27 Green			XX		X	
63S VII-1 Green		XX	XX		XX	
63S VII-45 Green		XXX	X		XX	
63S VII-45 Red		XXX	XX		XX	
63S VIII-47 Red		XXX	XX		XX	
63S IX-6 Red		XX	XX		XX	
63S X-19.2 Red		XX	X		XX	
63S X-75.5 Red		X	X		XX	
63 X-106.5 Red		XXX	XX		XX	
63S XII-16.5 Red	X		X	X	X	
63 XII-37.5 Red	X			XX		
1218-15 Bleach		XXX			XX	
1218-15 Red	XX	XXX			XX	
1218-12 Bleach		XXX	X		XX	
1218-12 Red		X	X		XX	
1218-10 Bleach	X	XXX			XX	
1218-10 Red	X	XX				
1218-09 Green		XXX			X	
1218-09 Red		XX			X	
1218-08 Red		XXX	X		XX	
1218-07 Bleach		XXX	X		X	
1218-07 Red		XXX	X		XX	
1218-04 Green		XXX			XX	
1218-04 Red		XXX				
1218-03 Green		XXX				
1218-01 Green		XXX	XX			

Table 4: LPSA grain-size data.

	Volume		Number	
Sample ID	Mode (µm)	Dx (90)	Mode (µm)	Dx (90)
1218-06 Green	122	253	5.48	8.94
1218-06 Red	5.53	304	5.12	6.62
1218-09 Green	304	695	5.42	8.46
1218-09 Red	540	676	5.18	7.59
1218-10 Bleach	299	561	5.5	8.53
1218-10 Red	285	523	5.28	7.19
1218-12 Bleach	353	516	5.49	9.49
1218-12 Red	112	176	2.04	5.34
1218-15 Bleach	397	595	5.5	8.77
1218-15 Red	265	423	5.09	9.02

Table 5: Whole-rock geochemistry of three representative RGB samples with a focus on Fe(II) as FeO, Fe(III) as Fe_2O_3, and uranium.

SAMPLE	1218-15	1218-15	1218-03
Group	RED	BLCH	GREEN
FeO	1.03	0.65	0.97
Fe_2O_3	5.46	2.54	2.01
Fe2+/3+	29.5%	36.3%	51.8%
U	2.26	1.82	14.35

APPENDIX

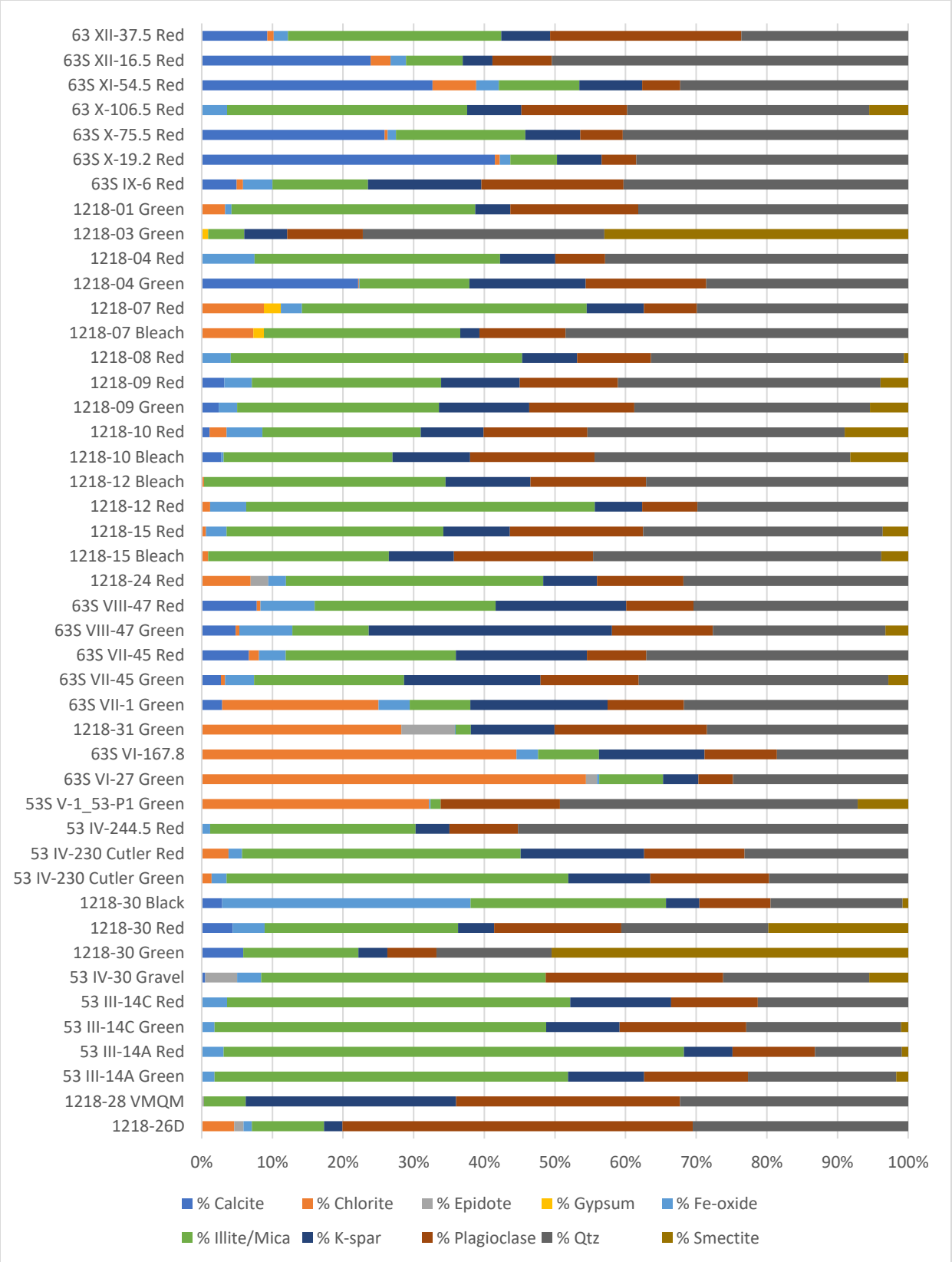

Fig. A1: XRD bulk mineralogy of 10 key minerals in 45 Cutler Formation samples.

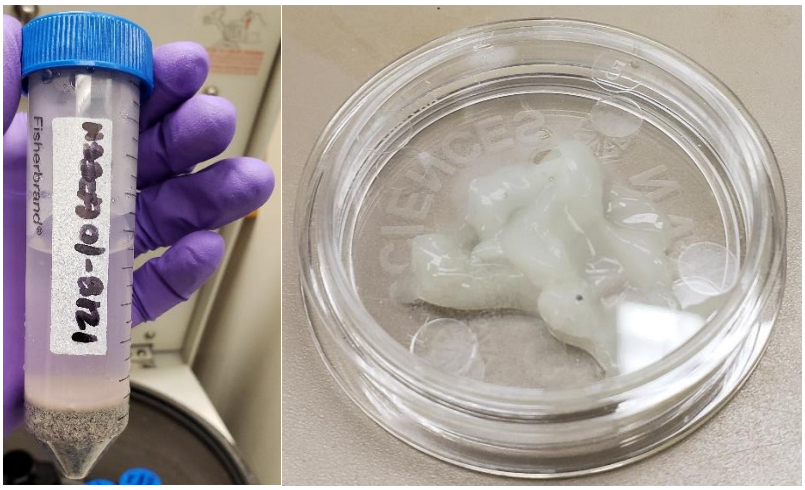

Fig. A2: Swelling clay “goo” from CBD treatment when preparing samples for LPSA. Goo is identified as smectite in Fig. A3 and was fixed by cooling the samples in an ice bath overnight. Eliminating the goo was important to prevent loss of clay from the sample.

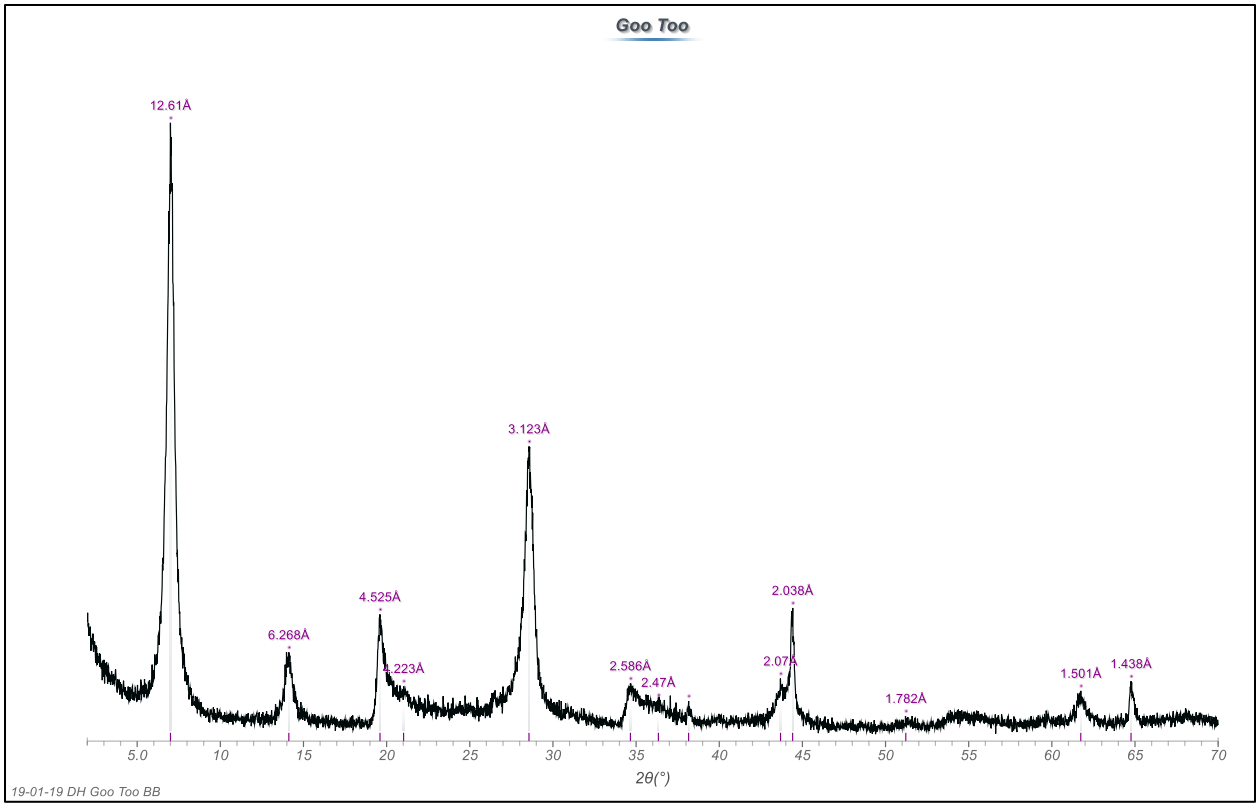

Fig. A3: Swelling clay XRD spectra of "goo" from CBD treatment, suggesting a dioctahedral smectite.

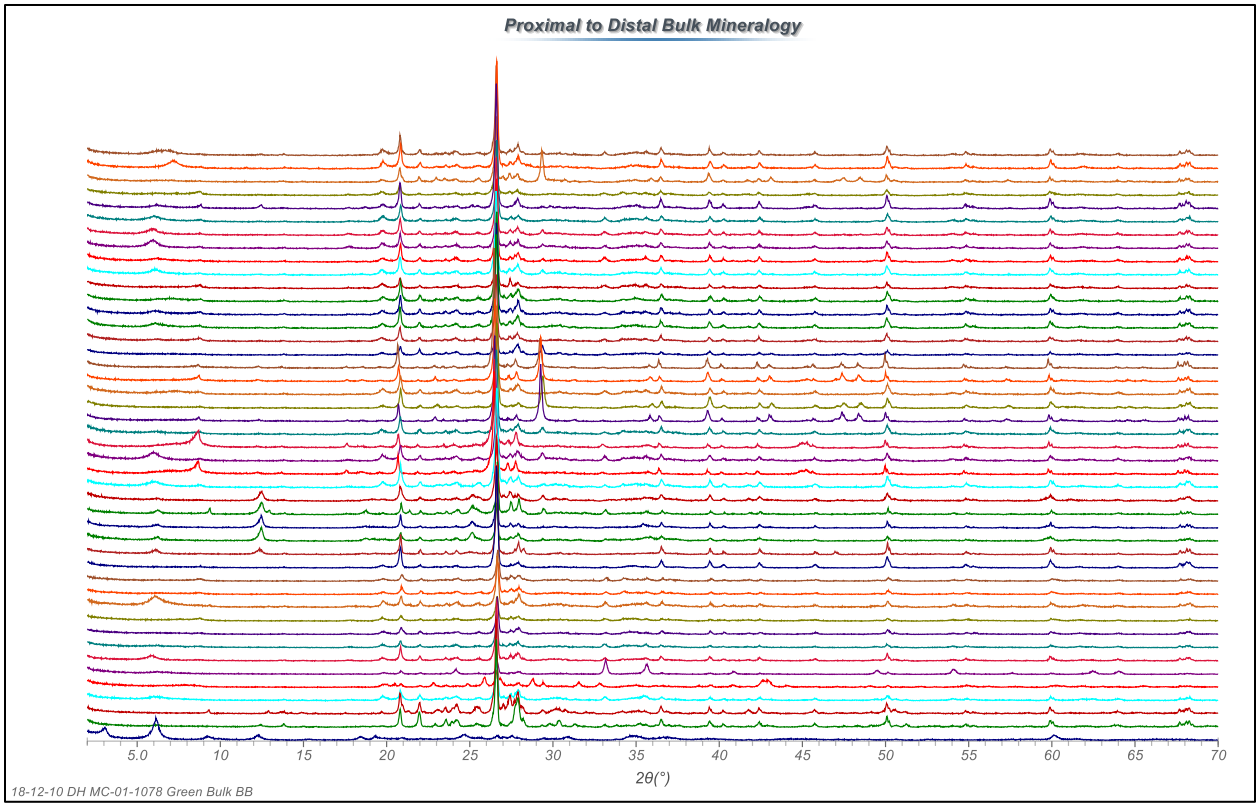

Fig. A4: XRD bulk mineralogy of all 45 Cutler samples interpreted from this study. The samples trend from proximal to distal with the proximal most samples on the bottom. Note not all phases are visible because the spectra are zoomed out in order to incorporate all the samples.

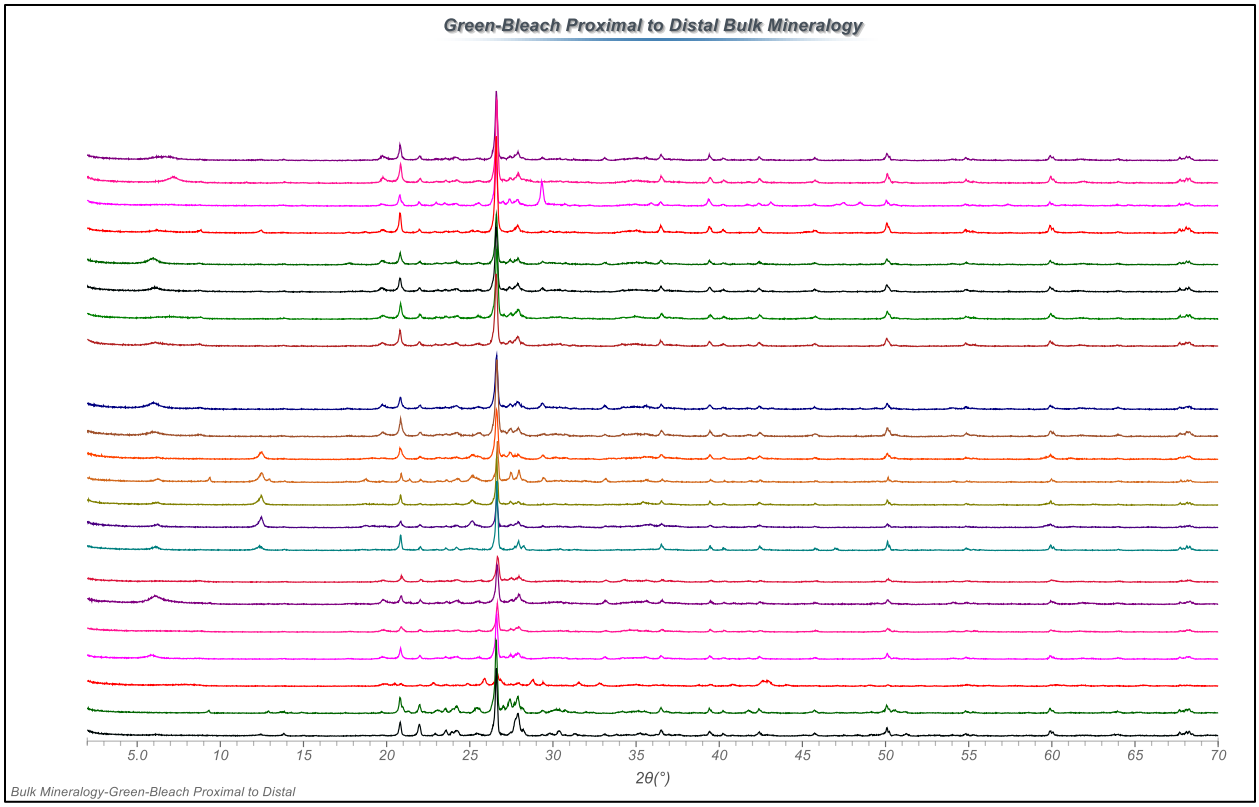

Fig. A5: Overlay of XRD bulk mineralogy of the green-bleached samples, in order from proximal to distal. The proximal most sample is on the bottom. Note not all phases are visible because the spectra are zoomed out in order to incorporate all the samples.

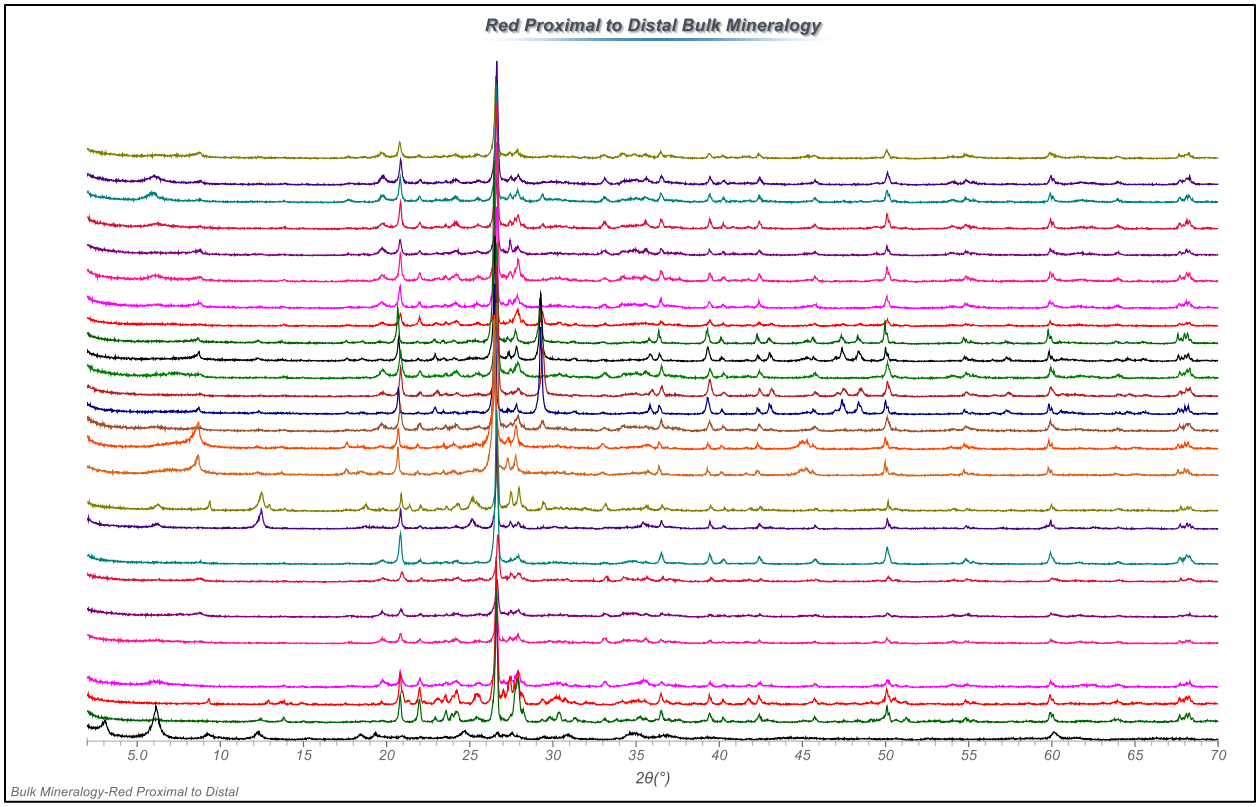

Fig. A6: XRD bulk mineralogy of the red samples trending from proximal to distal with the proximal most sample on the bottom. Note not all phases are visible because the spectra are zoomed out in order to incorporate all the samples.

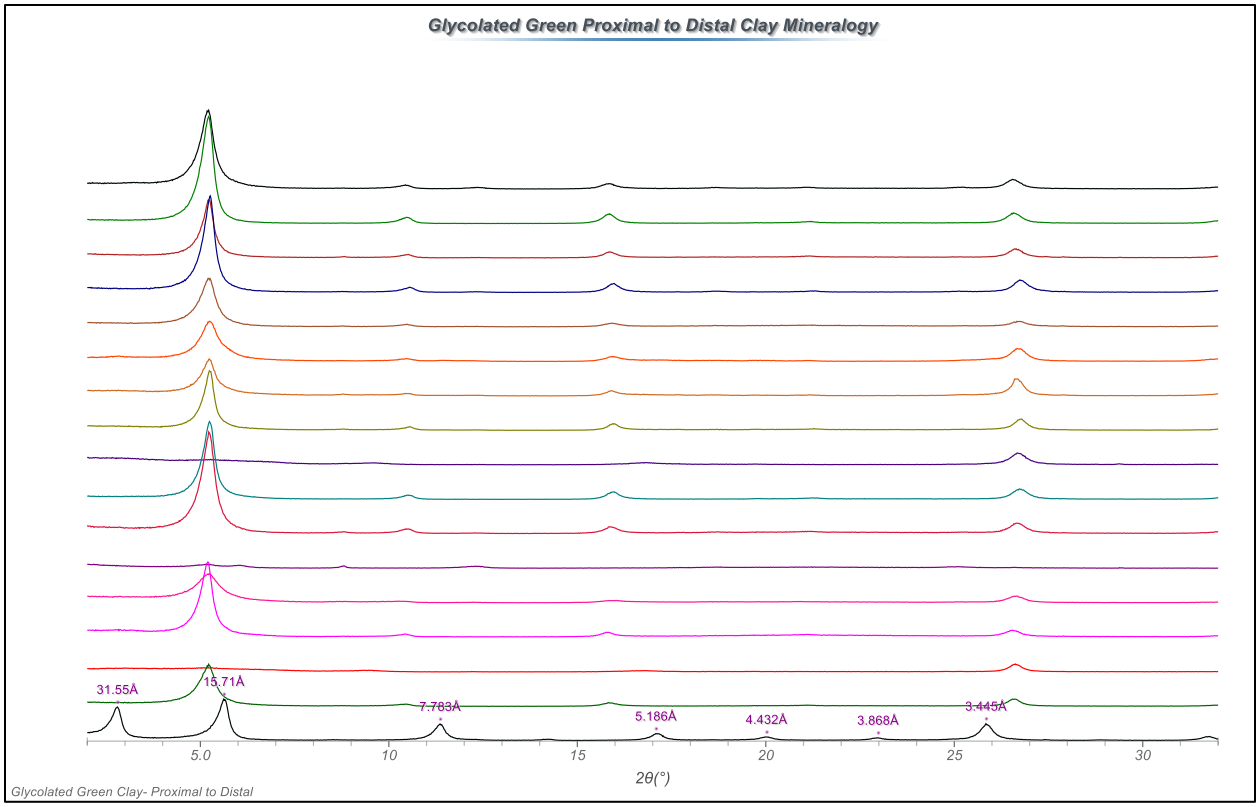

Fig. A7: XRD clay mineralogy of the glycolated green-bleached samples, trending from proximal to distal with the proximal most sample on the bottom. Note not all phases are visible because the spectra are zoomed out in order to incorporate all the samples.

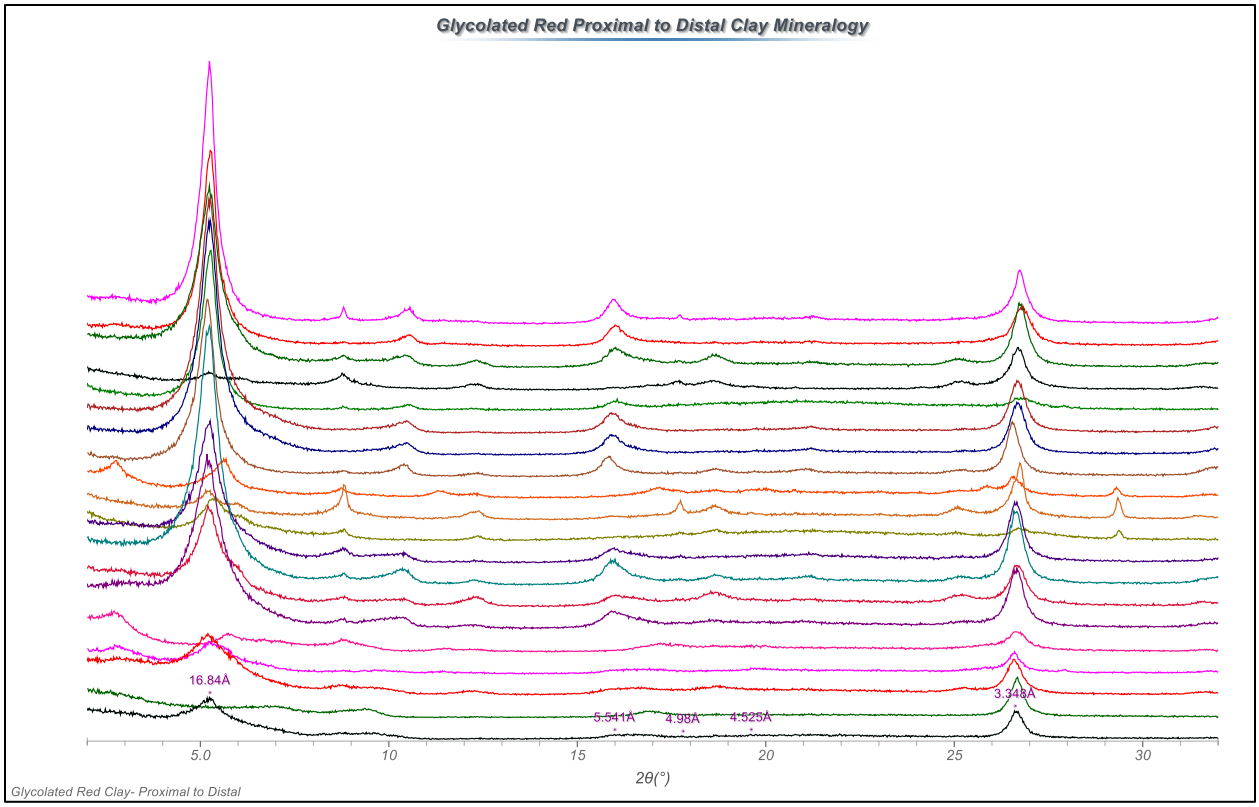

Fig. A8: Glycolated XRD clay mineralogy of all the red Cutler Fm samples trending from proximal to distal with the proximal most sample on the bottom. Note not all phases are visible because the spectra are zoomed out in order to incorporate all the samples.

Table A1: Cutler Formation clay mineral XRD analysis of 39 samples.

53 III-14A Red						53 III-14A Green					
Smectite	D-spacing	(001)	(002)	(003)	(004)	Smectite	D-spacing	(001)	(002)	(003)	(004)
	AD						AD	14.8-12.8	6.19	5.04	3.1
	EG						EG	16.9	8.45	5.6	4.2
	HT550						HT550	9.85	4.88	3.25	
Chlorite	D-spacing	(001)	(002)	(003)	(004)	Chlorite	D-spacing	(001)	(002)	(003)	(004)
	AD	14.2	7.17	4.74	3.52		AD				
	EG		7.12	4.76			EG				
	HT550	14.1					HT550				
Illite-Smectite IS55R0	D-spacing	(001)	(002)	(003)	(004)	Illite-Smectite	D-spacing	(001)	(002)	(003)	(004)
	AD	11.9	5.02	3.35	3.2		AD				
	EG	16.8	9.2	5.37	3.35		EG				
	HT550	10.1	4.97	3.31			HT550				
Illite	D-spacing	(001)	(002)	(003)	(004)	Illite	D-spacing	(001)	(002)	(003)	(004)
	AD	10.2	5.02	3.35			AD				
	EG	10.2	5.14	3.35			EG				
	HT550	10.1	4.97	3.31			HT550				
53 III-14C Red						53 III-14C Green					
Corrensite	D-spacing	(001)	(002)	(003)	(004)	Corrensite	D-spacing	(001)	(002)	(003)	(004)
	AD						AD	28	14.2		7.2
	EG						EG	32.1			7.24
	HT550						HT550	10.1	4.98	3.31	
Chlorite	D-spacing	(001)	(002)	(003)	(004)	Chlorite	D-spacing	(001)	(002)	(003)	(004)
	AD	14.3	7.18	4.73	3.54		AD				
	EG		7.16	4.74			EG				
	HT550	10.1	4.97	3.31			HT550				
Illite-Smectite (IS70R1)	D-spacing	(001)	(002)	(003)	(004)	Illite-Smectite (IS70R1)	D-spacing	(001)	(002/003)	(003/004)	(004)
	AD	10.9	5.04	3.25			AD	12	5.05	3.53	3.2
		(001)	(001/002)	(002/003)	(005)			(001)	(001/002)	(002/003)	(003/004)
	EG	13.1	9.44	5.24	3.34		EG	17	9.34	5.26	4.43
		(001)	(002)	(003)	(004)			(001)	(002)	(003)	(004)
	HT550	10.1	4.97	4.49	3.31		HT550	10.1	4.98	3.31	
Illite	D-spacing	(001)	(002)	(003)	(004)	Illite	D-spacing	(001)	(002)	(003)	(004)
	AD						AD	10.1	5.05	3.38	
	EG						EG	10.23	5.03	3.35	
	HT550						HT550	10.1	4.98	3.31	
1218-30 IV Red						1218-30 IV Green					
Smectite + trace chlorite	D-spacing	(001)	(002)	(003)	(004)	Smectite	D-spacing	(001)	(002)	(003)	(004)
	AD	15.3	7.24	5.02	3.76		AD	14.15	7.22		3.54
	EG	17	8.42	5.58	4.18		EG	16.67			
	HT550	10	4.91	3.25			HT550	9.97	4.95	3.31	
Chlorite	D-spacing	(001)	(002)	(003)	(004)	Chlorite	D-spacing	(001)	(002)	(003)	(004)
	AD	7.24	4.8	3.57			AD				
	EG		4.76				EG				
	HT550	13.9					HT550				
Illite-Smectite	D-spacing	(001)	(002)	(003)	(004)	Illite-Smectite (IS60R1)	D-spacing	(001)	002)/(003	(003/004)	(004/005)
	AD						AD	25.27	12.09	7.22	
								(001)	001)/(002	002)/(003	(005)
	EG						EG	28.44	13.55	9.22	5.28
								(001)	(002)	(003)	(004)
	HT550						HT550	9.97	4.95	3.31	
Illite	D-spacing	(001)	(002)	(003)	(004)	Illite	D-spacing	(001)	(002)	(003)	(004)
	AD						AD	10	5.01	3.32	
	EG						EG	10.08	5.01	3.34	
	HT550						HT550	9.97	4.95	3.31	
Calcite	D-spacing	(001)	(002)	(003)	(004)	Calcite	D-spacing	(001)	(002)	(003)	(004)
	AD						AD	3.04			
	EG						EG	3.04			
	HT550						HT550	3.03			

53 IV-230 Red						53 IV-230 Green					
Smectite	D-spacing	(001)	(002)	(003)	(004)	Smectite	D-spacing	(001)	(002)	(003)	(004)
	AD	12	6.18		3.24		AD				
	EG	16.97					EG				
	HT550						HT550				
Chlorite	D-spacing	(001)	(002)	(003)	(004)	Chlorite	D-spacing	(001)	(002)	(003)	(004)
	AD	14	7.19	4.78	3.55		AD	14.3	7.15	4.79	3.53
	EG	13.98	7.21	4.74	3.53		EG		7.23		3.34
	HT550	13.9					HT550			4.89	3.27
Illite-Smectite (IS55R1)	D-spacing	(001)	(002)	(003/004)	(005/006)	Illite-Smectite (IS10R0)	D-spacing	(001)	(002)	(003)	(004)
	AD						AD	12.4	6.2		3.1
	EG	28.79	14.95	9.21	5.45		EG	16.9	8.61	5.58	
	HT550	10	5.01	3.29			HT550	9.97	4.89	3.27	
Illite	D-spacing	(001)	(002)	(003)	(004)	Illite	D-spacing	(001)	(002)	(003)	(004)
	AD		5.01	3.34			AD	10.2	5.02	3.34	
	EG	10.15	5.1	3.35			EG	10.2	5.58	4.89	
	HT550	10	5.01	3.29			HT550	9.97	4.89	3.27	
IV-244.5 Red						53S V-1 Green					
Corrensite	D-spacing	(001)	(002)	(003)	(004)	Corrensite	D-spacing	(001)	(002)	(003)	(004)
	AD	29.2	13.6	8.99	7.12		AD				
	EG	32.24	15.51	9.97	7.71		EG				
	HT550	13.2					HT550				
Smectite	D-spacing	(001)	(002)	(003)	(004)	Smectite	D-spacing	(001)	(002)	(003)	(004)
	AD						AD	14.3	7.13	4.74	3.57
	EG						EG	17.2			
	HT550						HT550	12.6			
Chlorite	D-spacing	(001)	(002)	(003)	(004)	Chlorite	D-spacing	(001)	(002)	(003)	(004)
	AD	13.6	7.12	4.76	3.56		AD				
	EG	13.9	7.22	4.66	3.44		EG				
	HT550	13.9					HT550				
Chlorite-Smectite	D-spacing	(001)	(002)	(003)	(004)	Chlorite-Smectite (CS90R0)	D-spacing	(001)	(002)	(003)	(004/005)
	AD						AD	14.3	7.13	4.74	3.57
	EG						EG	14.6	7.19	4.72	3.54
	HT550						HT550	12.6		4.55	
Illite	D-spacing	(001)	(002)	(003)	(004)	Illite	D-spacing	(001)	(002)	(003)	(004)
	AD	10.1	5.32	3.32			AD	10.1	5	3.35	
	EG	10.1	5.17	3.35			EG	10	5	3.35	
	HT550	10.1	5	3.34			HT550	10.1	5	3.35	
63S VI-27 Green						63S VII-1 Green					
Smectite	D-spacing	(001)	(002)	(003)	(004)	Smectite	D-spacing	(001)	(002)	(003)	(004)
	AD						AD	12.5			
	EG						EG	17.1			
	HT550						HT550	10	5.02	3.35	
Chlorite	D-spacing	(001)	(002)	(003)	(004)	Chlorite	D-spacing	(001)	(002)	(003)	(004)
	AD	14.2	7.1	4.72	3.54		AD	14.2	7.1	4.71	3.54
	EG	14.3	7.1	4.72	3.53		EG	14.4	7.11	4.73	3.54
	HT550	14	7.02		3.47		HT550	13.8	6.92		3.44
Illite	D-spacing	(001)	(002)	(003)	(004)	Illite	D-spacing	(001)	(002)	(003)	(004)
	AD	10.1	5.02	3.35			AD	10	5	3.35	
	EG	10.1	5.02	3.35			EG	10	5	3.34	
	HT550	10.1	5	3.35			HT550	10	5.02	3.35	

63S VII-45 Red					
Smectite	D-spacing	(001)	(002)	(003)	(004)
	AD	12.5	6.14		3.1
	EG	16.9	8.53	5.58	4.18
	HT550	10	4.96	3.28	
Chlorite	D-spacing	(001)	(002)	(003)	(004)
	AD	14.1	7.16	4.75	3.56
	EG		7.23	4.76	3.53
	HT550	14		4.49	
Illite	D-spacing	(001)	(002)	(003)	(004)
	AD	10.1	5.01	3.34	
	EG	10	5.01	3.35	
	HT550	10	4.96	3.28	

63S VII-45 Green					
Smectite	D-spacing	(001)	(002)	(003)	(004)
	AD	12.8	6.17	3.75	3.75
	EG	16.9	8.45	5.59	4.21
	HT550	10	4.86	3.33	
Chlorite	D-spacing	(001)	(002)	(003)	(004)
	AD	14.8	7.17	4.77	3.54
	EG		7.2	4.74	3.52
	HT550	13.7			
Illite	D-spacing	(001)	(002)	(003)	(004)
	AD	10	5	3.34	
	EG	10	5.59	3.34	
	HT550	10	4.86	3.33	

63S VIII-47 Red					
Smectite	D-spacing	(001)	(002)	(003)	(004)
	AD	12.4	6.14	4.17	3.11
	EG	16.8	8.5	5.54	4.2
	HT550	10	4.97	3.3	
Chlorite	D-spacing	(001)	(002)	(003)	(004)
	AD	14.4	7.19		3.55
	EG		7.21		3.55
	HT550	13.8			3.3
Illite	D-spacing	(001)	(002)	(003)	(004)
	AD	10.1	5	3.34	
	EG	10.1	5	3.35	
	HT550	10	4.97	3.3	

53 IV-30 Gravel					
Smectite	D-spacing	(001)	(002)	(003)	(004)
	AD	12.5	6.18		3.09
	EG	17	8.47	5.62	4.21
	HT550	9.86	4.9	3.25	
Chlorite	D-spacing	(001)	(002)	(003)	(004)
	AD				
	EG				
	HT550				
Illite	D-spacing	(001)	(002)	(003)	(004)
	AD				
	EG				
	HT550				

63S IX-6 Red					
Smectite	D-spacing	(001)	(002)	(003)	(004)
	AD	12.7	7.19	4.77	3.57
	EG	17	8.49	5.53	4.27
	HT550	9.95	4.99	3.34	
Chlorite	D-spacing	(001)	(002)	(003)	(004)
	AD	14.4	7.19	4.77	3.57
	EG	14.57	7.17	4.78	3.53
	HT550	13.7		4.91	
Illite	D-spacing	(001)	(002)	(003)	(004)
	AD	10.1	5.02	3.35	
	EG	10	5.03	3.34	
	HT550	9.95	4.99	3.34	

63S X-19.2 "Unweathered" Red					
Smectite	D-spacing	(001)	(002)	(003)	(004)
	AD	12.5	6.2	4.26	3.11
	EG	16.5	8.25	5.5	4.15
	HT550	10	4.98	3.34	
Chlorite	D-spacing	(001)	(002)	(003)	(004)
	AD	14.1	7.17	4.74	3.56
	EG	14.7	7.17	4.75	3.55
	HT550	13.9		4.48	3.34
Illite	D-spacing	(001)	(002)	(003)	(004)
	AD	10.1	5.01	3.34	
	EG	10.1	5	3.34	
	HT550	10	4.98	3.34	

63S X-75.5 Red					
Smectite	D-spacing	(001)	(002)	(003)	(004)
	AD	12.5	4.27	3.04	
	EG	17.1	8.44	5.58	
	HT550	10	4.99	3.33	
Chlorite	D-spacing	(001)	(002)	(003)	(004)
	AD	14.1	7.14	4.75	3.56
	EG	14.8	7.15	4.75	3.55
	HT550	13.9			3.47
Illite	D-spacing	(001)	(002)	(003)	(004)
	AD	10.1	5	3.33	
	EG	10	5.01	3.33	
	HT550	10	4.99	3.33	

63S X-106.5 Red					
Smectite	D-spacing	(001)	(002)	(003)	(004)
	AD	12.4	6.16		3.11
	EG	17	8.52	5.57	
	HT550	9.99	4.93	3.28	
Chlorite	D-spacing	(001)	(002)	(003)	(004)
	AD	14	7.12	4.78	3.55
	EG		7.19	4.75	3.54
	HT550	13.6		4.93	3.28
Illite	D-spacing	(001)	(002)	(003)	(004)
	AD	10.1	5.03	3.33	
	EG	10	5.57	3.34	
	HT550	9.99	4.93	3.28	

63S XII-16.5 Red					
Corrensite	D-spacing	(001)	(002)	(003)	(004)
	AD	27.6	13.6	9.01	7.2
	EG	32.2	15.8	7.8	5.16
	HT550	12.1	8.07	4.28	3.05
Chlorite	D-spacing	(001)	(002)	(003)	(004)
	AD		7.2	4.77	3.57
	EG		7.21	4.75	3.54
	HT550	14.1	8.07	4.76	3.54
Illite-Smectite	D-spacing	(001)	(002)	(003)	(004)
	AD	11.7	5.35		2.96
	EG	15.8	7.8	5.16	3.86
	HT550	10.2	5.01	3.36	
Illite	D-spacing	(001)	(002)	(003)	(004)
	AD	10.2	5.04	3.36	
	EG	10.1	5.03	3.35	
	HT550	10.2	5.01	3.36	

63S XII-37.5 Red					
Corrensite	D-spacing	(001)	(002)	(003)	(004)
	AD	28	13.5	9.03	7.18
		(001)	(002)	(004)	
	EG	32.3	16.9	7.74	
		(001)	(002/003)	(004)	
	HT550	12	4.52	3.28	
Illite-Smectite (IS60R1)	D-spacing	(001)	(002)	(003)	(004)
	AD	12.3		4.52	3.53
	EG	16.9	9.18	5.36	3.35
	HT550	10	4.97	3.28	

1218-15 Red					
Corrensite	D-spacing	(001)	(002)	(003)	(004)
	AD	29.5	15.1		7.24
	EG	32.1	16.9	10	8.37
	HT550	9.97	4.8	3.2	
Smectite	D-spacing	(001)	(002)	(003)	(004)
	AD	15.1	7.24	5	3.77
	EG	16.9	8.37	5.55	4.18
	HT550	9.97	4.8	3.2	
Illite	D-spacing	(001)	(002)	(003)	(004)
	AD	10	5	3.33	
	EG	10	5	3.33	
	HT550	9.97	4.99	3.33	

1218-15 Bleach					
Corrensite	D-spacing	(001)	(002)	(003)	(004)
	AD				
	EG				
	HT550				
Smectite	D-spacing	(001)	(002)	(003)	(004)
	AD	15.1	7.17	4.77	3.74
	EG	16.8	8.39	5.55	4.17
	HT550	9.99	4.84	3.21	
Illite	D-spacing	(001)	(002)	(003)	(004)
	AD	10.1	5.01	3.35	
	EG	10	5.55	3.33	
	HT550	9.99	5.01	3.33	

1218-12 Red					
Smectite	D-spacing	(001)	(002)	(003)	(004)
	AD	12.4		4.27	3.11
	EG	16.9		5.55	4.27
	HT550	10.1	5.01	4.27	3.34
Chlorite	D-spacing	(001)	(002)	(003)	(004)
	AD	14.2	7.15	4.75	3.55
	EG	14.7	7.21	4.77	3.54
	HT550	13.8			
Illite	D-spacing	(001)	(002)	(003)	(004)
	AD	10.2	5	3.34	
	EG	10.1	5.02	3.34	
	HT550	10.1	5.01	3.34	

1218-12 Bleach					
Smectite	D-spacing	(001)	(002)	(003)	(004)
	AD	12.5	6.18		3.1
	EG	16.9	8.45	5.57	4.19
	HT550	9.73	4.84	3.22	
Chlorite	D-spacing	(001)	(002)	(003)	(004)
	AD		7.15	4.74	3.54
	EG		7.14	4.75	3.52
	HT550	9.73	4.84	3.22	
Illite	D-spacing	(001)	(002)	(003)	(004)
	AD	10.1	5.04	3.35	
	EG	10.1	5.04	3.34	
	HT550	9.73	4.84	3.31	

1218-10 Red					
Corrensite	D-spacing	(001)	(002)	(003)	(004)
	AD	30.4	15.1	10.1	7.2
	EG	32.7	16.8		8.37
	HT550	11.8	4.84	3.2	
Smectite	D-spacing	(001)	(002)	(003)	(004)
	AD	15.1	7.2	5.02	3.75
	EG	16.8	8.37	5.53	
	HT550	9.69	4.84	3.2	
Illite	D-spacing	(001)	(002)	(003)	(004)
	AD				
	EG				
	HT550				

1218-10 Bleach					
Corrensite	D-spacing	(001)	(002)	(003)	(004)
	AD	28.3		8.92	7.15
	EG	31.1	16.8		7.75
	HT550	9.78	4.85	3.23	
Smectite	D-spacing	(001)	(002)	(003)	(004)
	AD	12.5	6.19		3.1
	EG	16.8	8.45	5.56	4.19
	HT550	9.78	4.85	3.23	
Illite	D-spacing	(001)	(002)	(003)	(004)
	AD	10.2	5.01	3.33	
	EG	10.1	5.15	3.34	
	HT550	9.78	4.85	3.23	

1218-09 Red					
Smectite	D-spacing	(001)	(002)	(003)	(004)
	AD	13.1	6.28	4.7	
	EG	16.7	8.41	5.52	
	HT550	9.99	4.86	3.21	
Illite	D-spacing	(001)	(002)	(003)	(004)
	AD	10.1		3.35	
	EG	10.1		3.33	
	HT550	9.99		3.35	

1218-09 Green					
Smectite	D-spacing	(001)	(002)	(003)	(004)
	AD	12.5	6.19		3.09
	EG	16.9	8.44	5.56	
	HT550	9.82	4.87	3.23	
Illite	D-spacing	(001)	(002)	(003)	(004)
	AD	10.1		3.35	
	EG	10.1		3.34	
	HT550	9.82		3.35	

1218-08 Red					
Smectite	D-spacing	(001)	(002)	(003)	(004)
	AD	12.5	6.21		3.1
	EG	17	8.5	5.59	4.22
	HT550	9.88	4.87	3.25	
Chlorite	D-spacing	(001)	(002)	(003)	(004)
	AD		7.2	4.73	3.55
	EG		7.17	4.75	3.52
	HT550	14.1		4.87	3.25
Illite	D-spacing	(001)	(002)	(003)	(004)
	AD	10	5.01	3.33	
	EG	10.1	5	3.36	
	HT550	9.88	4.87	3.25	

1218-07 Red					
Smectite	D-spacing	(001)	(002)	(003)	(004)
	AD	15.1	7.16	5	
	EG	16.9	8.48	5.53	4.19
	HT550	9.97	4.92	3.26	
Chlorite	D-spacing	(001)	(002)	(003)	(004)
	AD		7.16	4.76	3.55
	EG		7.18	4.77	3.54
	HT550	14.1		4.92	
Illite	D-spacing	(001)	(002)	(003)	(004)
	AD	10.1	5	3.33	
	EG	10	5	3.33	
	HT550	9.97	4.92	3.33	

1218-07 Bleach					
Smectite	D-spacing	(001)	(002)	(003)	(004)
	AD	15.1		5.01	3.75
	EG	16.8	8.38	5.54	4.17
	HT550	9.98	4.7	3.18	
Chlorite	D-spacing	(001)	(002)	(003)	(004)
	AD		7.16	4.76	3.54
	EG		7.18	4.76	3.54
	HT550	13		4.7	
Illite	D-spacing	(001)	(002)	(003)	(004)
	AD	10.1	5.01	3.35	
	EG	10.1		3.33	
	HT550	9.98		3.31	

1218-04 Red					
Smectite	D-spacing	(001)	(002)	(003)	(004)
	AD	12.5	6.18	4.75	3.09
	EG	16.8	8.45	5.57	4.19
	HT550	9.82	4.84	3.21	
Illite	D-spacing	(001)	(002)	(003)	(004)
	AD				
	EG				
	HT550				

1218-04 Green					
Smectite	D-spacing	(001)	(002)	(003)	(004)
	AD	12.5	6.2		3.1
	EG	16.9	8.41	5.59	4.19
	HT550	10	4.81	3.19	
Illite	D-spacing	(001)	(002)	(003)	(004)
	AD	10.1	5.02	3.35	
	EG	10	5.01	3.34	
	HT550	10	5	3.33	

1218-03 Green					
Smectite	D-spacing	(001)	(002)	(003)	(004)
	AD	15.2		5.03	3.76
	EG	16.9	8.45	5.58	4.19
	HT550	9.71	4.7	3.18	
Chlorite	D-spacing	(001)	(002)	(003)	(004)
	AD				
	EG				
	HT550				

1218-01 Green					
Smectite	D-spacing	(001)	(002)	(003)	(004)
	AD	12.5	6.23		3.09
	EG	16.9	8.47	5.59	4.21
	HT550	9.87	4.87	3.25	
Chlorite	D-spacing	(001)	(002)	(003)	(004)
	AD		7.12	4.75	3.54
	EG		7.18	4.75	3.54
	HT550	14.1			